THERMAL TRANSPORT PROPERTIES OF MANGANESE FLUORIDE

THERMAL TRANSPORT PROPERTIES
OF
MANGANESE FLUORIDE

By

DAVID JOHN SANDERS, B.Sc.

A Thesis

Submitted to the Faculty of Graduate Studies

in Partial Fulfilment of the Requirements

for the Degree

Doctor of Philosophy

McMaster University

November 1975

DOCTOR OF PHILOSOPHY (1975) McMASTER UNIVERSITY
(Physics) Hamilton, Ontario

TITLE: Thermal Transport Properties of Manganese Fluoride

AUTHOR: David John Sanders, B.Sc. (McMaster University)

SUPERVISOR: Dr. D. Walton

NUMBER OF PAGES: xi, 186

SCOPE AND CONTENTS:

The thermal transport properties of MnF_2 were investigated through thermal conductivity and heat pulse experiments. The roles played by the magnons and by the OH^- impurities in MnF_2 were studied. The absence of magnon conductivity was explained in terms of the magnon-phonon equilibrium time. Theoretical expressions were quantitatively fitted to the experimental results and a tunneling model was proposed for the OH^- impurity states.

ABSTRACT

The thermal transport properties of the antiferromagnet manganese fluoride were investigated using thermal conductivity and heat pulse measurements. With heat flow along the [001] crystallographic direction, the thermal conductivity was measured at temperatures from 0.3 to 4.2 K in magnetic fields ranging from 0 to 60 kOe. Heat pulse signals were measured for pulse propagation along the [001] and [110] directions for an ambient sample temperature of 2.0 K, and pulse temperatures between 2.5 and 6.0 K.

With a magnetic field applied along the [001] direction the thermal conductivity showed no change that could be attributed to heat transport by the antiferromagnetic magnons. This result was in disagreement with calculations of the boundary limited magnon conductivity. It was demonstrated that the absence of magnon heat conduction could be due to the long magnon-phonon relaxation time of MnF_2. This general explanation could also be applied to other magnetic materials.

The results for the thermal conductivity as a function of temperature showed a dip at 1.0 K which indicated a resonant interaction of the phonons with an impurity. The impurity has previously been shown to be OH^-. The attenuation of the heat pulses indicated that only the E_g phonon mode was resonantly scattered. These results were shown to be consistent with the previously unexplained low temperature decrease in the C_{44}

elastic constant of MnF_2. This was accounted for by the reduction in the velocity of the E_g phonons caused by their resonant interaction with the OH^- impurities.

Theoretical expressions were fitted to the experimental results. It was found to be important to include phonon focusing effects in these expressions. The thermal conductivity, heat pulse, and elastic constant results were all accounted for by a single set of adjustable parameters. From the fits, the level splitting of the OH^- impurity states was found to be 2.8 cm^{-1}, the OH^- impurity concentration was estimated to be 8×10^{16} cm^{-3}, and the elastic dipole moment of the OH^- molecule was calculated to be 3.4×10^{-24} cm^3.

When a magnetic field was applied at an angle of 25° to the [001] axis, the conductivity increased below 1.2 K, and decreased for higher temperatures. This was shown to be due to an increase in the resonant frequency of the impurity.

A tunneling model was proposed for the OH^- impurity states in MnF_2. The low lying states of the model system were shown to form a tunnel split doublet. The symmetries of the states were such that only E_g phonons would cause transitions between them. In an off-axis magnetic field, the tunnel splitting was shown to increase due to the static strain caused by the magnetoelastic interaction. Thus, it was demonstrated that a tunneling model was consistent with the experimental results.

ACKNOWLEDGEMENTS

I wish to express my sincere appreciation to my supervisor, Dr. D. Walton, for his guidance, interest, and considerable patience during the course of this work.

I also wish to thank my colleague and friend, Dr. John C. Gustafson, who built the heat pulse apparatus, and whose assistance in this work was invaluable.

I am very grateful to my fellow graduate students in the solid state division, whose help and friendship have made my years in graduate school enjoyable as well as educational.

I wish to thank Drs. K. Maxwell, H. E. Jackson and D. Henry for their help in the laboratory, and Dr. D. A. Goodings for several useful discussions.

Dr. R. L. Melcher is gratefully acknowledged for providing the elastic constant data for MnF_2.

Thanks are also due to Mrs. H. Kennelly for her skillful typing of this thesis.

This research was supported by grants from the National Research Council of Canada. Personal financial support from N.R.C. and McMaster University is also gratefully acknowledged.

Finally, my deepest thanks are given to my parents for their support and encouragement through the years. I dedicate this thesis to them.

TABLE OF CONTENTS

LIST OF FIGURES

LIST OF TABLES

CHAPTER I

INTRODUCTION

The information derived from the thermal transport properties of a solid can be divided into two broad categories. Since a heat current is carried by the propagating elementary excitations of the solid, thermal transport measurements can provide information about these excitations and the interactions among them. Secondly, once the excitations are known, these measurements can be used to study the properties of impurities in the solid through their interaction with the thermal carriers.

In a magnetically ordered crystal there may exist propagating excitations of the spin system known as magnons. These can carry heat through the crystal in the same manner as the more familiar lattice excitations, or phonons. In 1955, Sato[1] pointed out that, at liquid helium temperatures, the magnon system can have a specific heat equal to, or greater than, that of the phonons. Since the velocities of the two excitations are comparable, this means an appreciable fraction of the total thermal conductivity of the crystal can be due to the magnons.

Since then, there has been considerable interest in finding experimental evidence for magnon heat transport.

These experiments have been confined to dielectric magnetic materials because the thermal conductivity of a metal is dominated by the conduction electrons. Magnon conductivity can be recognized by a departure of the thermal conductivity from the T^3 behaviour expected for phonons. Another useful technique is the measurement of any change in the conductivity that occurs when an external magnetic field is applied to the sample. In a ferromagnetic or ferrimagnetic material, the energies of the magnons are raised by the applied field, which decreases their thermal populations, thus lowering the magnon contribution to the total conductivity. In an antiferromagnet, the energy of one magnon branch is lowered, causing a net increase in the magnon contribution.

The first, and still the best documented case of heat conduction by magnons was found in 1962 for the ferrimagnet yttrium iron garnet (YIG)[2-4]. The thermal conductivity of YIG exhibited the expected dependences on temperature and on magnetic field. By measuring the conductivity in fields large enough to completely remove the magnon contribution, it was estimated[5] that about two thirds of the zero field conductivity was due to the magnons. The experimental results for YIG have also been quantitatively explained in terms of theoretical expressions for the magnon and phonon components[6,7].

Experimental evidence for magnon conductivity has also been reported for the ferromagnets EuS[8], and $CuCl_2(CH_3NH_3Cl)$[9]; the ferrimagnet Li ferrite[5]; and the

antiferromagnets $CoCl_2 \cdot 6H_2O$[10], $Co[(NH_2)_2CS]_4 \cdot Cl_2$[11], and $GdVO_4$[12]. However, compared to YIG, the evidence for these materials is much more tenuous. In some cases (EuS, and $CuCl_2(CH_3NH_3Cl)$) it is based only on the temperature dependence of the conductivity, and in other cases ($CoCl_2 \cdot 6H_2O$, Li ferrite, and $GdVO_4$) only on the magnetic field dependence. It has been pointed out[5,13] that care must be taken in interpreting the magnetic field results. Even if there is no magnon contribution, the thermal conductivity can change with magnetic field if the phonon conductivity is field dependent. This is the case if the contribution of phonons with particular energies is suppressed by a resonant interaction with magnetic impurities, or with the magnons themselves. A magnetic field will alter the resonant energy, thus changing the phonon conductivity. Finally, for most of the above systems, there has been no attempt to quantitatively explain the results in terms of theoretical predictions.

A partial list of the many magnetic materials which have been investigated without finding evidence for magnon conductivity includes the ferromagnets $GdCl_3$[5,13], and $CuK_2Cl_4 \cdot 2H_2O$[14]; the ferrimagnets $MnFe_2O_4$, $Co(Zn)Fe_2O_4$, and $Mn(Zn)Fe_2O_4$[15]; and the antiferromagnets $CuCl_2 \cdot 2H_2O$[10], $MnCl_2 \cdot 4H_2O$[13,6], and $FeCl_2$[17]. There are conflicting experimental results for the antiferromagnet $RbMnF_3$. Gustafson[18] found no evidence for magnon heat conduction, but recent results by Hartmann[19] showed a low temperature

enhancement of the conductivity that was attributed to the magnons.

To summarize, while the theoretical prediction of heat transport by magnons has long been established, experimental confirmation of this prediction has been very elusive.

In this regard, MnF_2 provides an attractive material for investigation. Since it is a nearly ideal two sublattice system, MnF_2 is probably the most extensively studied antiferromagnetic material. Most of its magnetic properties, and in particular its magnon dispersion curves[20,21], have been measured. This allows the magnon conductivity of MnF_2 to be calculated with a minimum of approximations. Therefore, the regions of temperature, and of magnetic field which should be experimentally investigated can be determined beforehand. The thermal conductivity of MnF_2 has been measured previously by several workers[18,19,22], but not in magnetic fields large enough to significantly affect the magnon conductivity.

In addition, MnF_2 is an interesting material for study because it is found that its phonon conductivity is governed by a strong resonant interaction with an impurity. In this regard, thermal transport in MnF_2 was also investigated using heat pulse experiments. These are complimentary to thermal conductivity measurements in the sense that they provide time resolution, which allows the contribution of each phonon mode to be studied individually.

The impurity has been noticed in previous experiments[18,19,23,24] and has been shown[24] to be OH^- which occurs even in nominally pure MnF_2. As a result of the experiments reported in this thesis, it was found that the properties of this impurity are strikingly similar to those of molecular impurities such as OH^- in alkali halide host crystals. These form an important class of impurity modes known as tunneling states. They occur when a molecule substitutes in a crystal lattice in such a way that it has several equivalent orientations in its lattice site and can quantum mechanically tunnel between them.

Tunneling modes in solids were first predicted in 1930 by Pauling[25]. Since then, there has been a great deal of investigation of tunneling states, principally in alkali halide hosts, using a variety of experimental techniques. As well as thermal conductivity, these include specific heat, infrared absorption, ultrasonic velocity and dielectric constant measurements. It is beyond the scope of this introduction to list the wealth of theoretical and experimental information available for tunneling systems. For an overview of the subject, the reader is referred to the review article by Narayanamurti and Pohl[26].

Thus, the purpose of the experiments reported in this thesis is twofold. Thermal transport in MnF_2 has been investigated using thermal conductivity and heat pulse experiments

with a view to determining the roles played both by the magnons and by the impurity states of the OH^- molecule.

The thesis is organized in the following manner. The theoretical concepts which will be needed to explain the results are developed in Chapter II. Chapter III contains a brief description of the experimental apparatus and techniques. In Chapter IV the experimental results are presented along with brief qualitative discussions of their significance. In Chapter V and related appendices, theoretical expressions are quantitatively fitted to the results, and models are proposed to explain the behaviour of the magnon system, and of the OH^- impurity system. Chapter VI concludes the thesis with a brief summary of the significant results and recommendations for further study.

CHAPTER II

THEORY

A. Thermal Conductivity

As pointed out in the introduction, the principal elementary excitations in an insulating antiferromagnetic solid are phonons and magnons. Since these have very similar thermal properties, a general theory can be developed to describe a heat current carried by either of these excitations. The phonons[27] or magnons[28] can be labelled by the wave vector of the mode $\vec{g}$, and the dispersion branch index ℓ. For acoustic phonons there are three branches corresponding to one longitudinal and two transverse polarizations. For the antiferromagnetic magnons there are two branches, one for each sublattice. The part of the Hamiltonian of the system due to either of these excitations has the form[27,28]

$$H = \sum_{\vec{g},\ell} (c^{\dagger}(\vec{g},\ell)c(\vec{g},\ell) + \frac{1}{2})\hbar\omega(\vec{g},\ell) \qquad (2.1)$$

where $c^{\dagger}$ and c are excitation creation and annihilation operators respectively. The operator $n(\vec{g},\ell) = c^{\dagger}(\vec{g},\ell)c(\vec{g},\ell)$ gives the number of quanta of energy $\hbar\omega(\vec{g},\ell)$ in a state $|\vec{g},\ell\rangle$.

It is useful to form localized wavepackets from these modes with wave vectors near $\vec{g}$ [29]. The velocity of a wavepacket is given by the group velocity,

$$\vec{v}_G(\vec{g},\ell) = \vec{\nabla}_g \omega(\vec{g},\ell) \tag{2.2}$$

where $\vec{\nabla}_g$ is the gradient operator in reciprocal space. Then the system can be considered to be a gas of particles, each carrying energy $\hbar\omega(\vec{g},\ell)$ at a velocity $\vec{v}_G(\vec{g},\ell)$. Both phonons and magnons are bosons, so if the system is in thermal equilibrium at a temperature T, the expectation value of the number operator is given by the Bose-Einstein distribution[27,28],

$$N(\vec{g},\ell) = \frac{1}{e^{\hbar\omega(\vec{g},\ell)/k_B T} - 1} . \tag{2.3}$$

If a temperature gradient $\vec{\nabla}T$ is applied to the system, the excitation population will be a function of position, and will be a non-equilibrium distribution $N'(\vec{g},\ell;\vec{r})$. The heat flux at $\vec{r}$ will be given by

$$\vec{Q} = \sum_{\vec{g},\ell} \hbar\omega(\vec{g},\ell) N'(\vec{g},\ell;\vec{r}) \vec{v}_G(\vec{g},\ell) . \tag{2.4}$$

In an equilibrium situation, the modes are distributed symmetrically in reciprocal space, so $N(\vec{g},\ell) = N(-\vec{g},\ell)$, and $\vec{Q} = 0$. Therefore, (2.4) can be written as

$$\vec{Q} = \sum_{\vec{g},\ell} \hbar\omega(\vec{g},\ell) \delta N(\vec{g},\ell) \vec{v}_G(\vec{g},\ell) \tag{2.5}$$

where $\delta N(\vec{g},\ell) = N'(\vec{g},\ell) - N(\vec{g},\ell)$ is the departure of the population from its equilibrium value.

The excitation population at a given point will tend to change due to scattering from other excitations, impurities,

and the boundaries of the sample, and due to the drift motion of the wavepackets in the temperature gradient. The classical Boltzmann equation[29,30] states that if the system is in a steady state, the sum of the rates of change of the population due to each of these mechanisms is zero. Therefore,

$$\left.\frac{\partial N'(\vec{q},\ell)}{\partial t}\right|_{\text{scattering}} - \vec{v}_G(\vec{q},\ell)\cdot\vec{\nabla}T\,\frac{\partial N'(\vec{q},\ell)}{\partial T} = 0 \quad . \qquad (2.6)$$

For those scattering mechanisms which tend to restore the non-equilibrium distribution to equilibrium, the first term in (2.6) can be expressed as[29,30]

$$\left.\frac{\partial N'(\vec{q},\ell)}{\partial t}\right|_{\text{scattering}} = \sum_n \frac{N(\vec{q},\ell)-N'(\vec{q},\ell)}{\tau_n} \quad , \qquad (2.7)$$

using the relaxation time approximation which assumes that $N'(\vec{q},\ell)$ decays exponentially to $N(\vec{q},\ell)$. The sum is over the different scattering processes and τ_n is the relaxation time for each. Normal processes (phonon-phonon, or magnon-magnon scattering in which the wave vector is conserved) do not return the system to equilibrium, and by themselves cannot contribute to the thermal resistivity. However, they do tend to replenish the populations of modes which have been depleted by other scattering mechanisms, and in a general treatment[31] should be included. However, at the low temperatures that this work is concerned with, the scattering due to these processes is negligible[29,30].

Substituting (2.7) into (2.6), and assuming that the departure from equilibrium is small so that

$$\frac{\partial N'(\vec{g},\ell)}{\partial T} \simeq \frac{\partial N(\vec{g},\ell)}{\partial T}$$

then,

$$\delta N(\vec{g},\ell) = - \frac{\partial N(\vec{g},\ell)}{\partial T} \tau_T(\vec{g},\ell) \vec{v}_G(\vec{g},\ell) \cdot \vec{\nabla} T \qquad (2.8)$$

where τ_T is the total relaxation time, given by

$$\tau_T^{-1}(\vec{g},\ell) = \sum_n \tau_n^{-1}(\vec{g},\ell) \ . \qquad (2.9)$$

Substituting (2.8) into (2.5), the heat flux becomes

$$\vec{Q} = -\sum_{\vec{g},\ell} \hbar\omega(\vec{g},\ell) \frac{\partial N(\vec{g},\ell)}{\partial T} \vec{v}_G(\vec{g},\ell) \tau_T(\vec{g},\ell) \times \vec{v}_G(\vec{g},\ell) \cdot \vec{\nabla} T \ . \qquad (2.10)$$

In general, the thermal conductivity coefficient K is a tensor which relates the heat flux to the temperature gradient by[29,30]

$$Q_\alpha = - \sum_\beta K_{\alpha\beta} \nabla T_\beta \ .$$

Therefore, from (2.10),

$$K_{\alpha\beta} = \sum_{\vec{g},\ell} \hbar\omega(\vec{g},\ell) \frac{\partial N(\vec{g},\ell)}{\partial T} \tau_T(\vec{g},\ell) \times (v_G(\vec{g},\ell))_\alpha (v_G(\vec{g},\ell))_\beta \ . \qquad (2.11)$$

The number of independent components of the conductivity tensor can be deduced by symmetry considerations. If the temperature

gradient is applied along a symmetry direction, then the heat flux must also be along this direction. For example, for a tetragonal crystal such as MnF_2, applying this condition to the [100], [010] and [001] directions proves that the off-diagonal components must be zero. Applying it to the [110] direction shows that $K_{xx} = K_{yy}$. Therefore, for a tetragonal crystal there are only two independent components, K_{xx} and K_{zz}. From (2.11), each of these is given by

$$K = \sum_{\vec{g},\ell} C(\vec{g},\ell) v_G^2(\vec{g},\ell) \tau_T(\vec{g},\ell) \cos^2\theta_G(\vec{g},\ell) \qquad (2.12)$$

where $C(\vec{g},\ell) = \hbar\omega(\vec{g},\ell)\partial N(\vec{g},\ell)/\partial T$ is the specific heat of the mode $(\vec{g},\ell)$, and $\theta_G(\vec{g},\ell)$ is the angle between $\vec{v}_G(\vec{g},\ell)$ and the heat flow direction. Changing the sum over the discrete set of states $\vec{g}$ to an integral in the usual fashion[27] this can be expressed as

$$K = \frac{1}{(2\pi)^3} \sum_{\ell} \int C(g,\ell) v_G^2(\vec{g},\ell) \tau_T(\vec{g},\ell) \cos^2\theta_G(\vec{g},\ell) d^3g \qquad (2.13)$$

where the integral extends over the first Brillouin zone, so that all possible wave vectors are included.

To calculate the conductivity using (2.13), it is necessary to know the dispersion relations for the excitations in order to calculate $C(\vec{g},\ell)$ and $\vec{v}_G(\vec{g},\ell)$, and the scattering processes in order to calculate $\tau_T(\vec{g},\ell)$. At low temperatures an important mechanism is scattering from the boundaries of the sample. If this is the only scattering process, the conductivity

is said to be boundary limited, and depends on the dimensions of the sample. McCurdy et al.[32] have developed expressions for the conductivity in the boundary limit for several geometries. For a cylindrical sample of diameter D, with heat flow along the cylinder axis, it was found that

$$K_b = \frac{4}{3\pi} D \frac{1}{(2\pi)^3} \sum_{\ell} \int C(\vec{g},\ell) v_G(\vec{g},\ell) \frac{\cos^2\theta_G(\vec{g},\ell)}{\sin\theta_G(\vec{g},\ell)} d^3g, \quad (2.14)$$

apart from a length correction term which can be neglected if the sample is long compared to its diameter. Therefore, by comparison with (2.13), the relaxation time for boundary scattering is

$$\tau_b(\vec{g},\ell) = \frac{4}{3\pi} \frac{1}{v_G(\vec{g},\ell)} \frac{D}{\sin\theta_G(\vec{g},\ell)} . \quad (2.15)$$

In the following sections, these general results will be used to calculate the thermal conductivity due to phonons and magnons.

B. Phonon Conductivity

The motions of a crystal lattice can be resolved into the normal modes of the system. These may be quantized into excitations called phonons. The Hamiltonian for the crystal lattice can be expressed as[27]

$$H = \frac{1}{2} m \sum_{\ell j} \left(\frac{\partial u_{\ell j}}{\partial t}\right)^2 + \frac{1}{2} \sum_{\ell j, \ell' j'} A_{\ell j \ell' j'} u_{\ell j} u_{\ell' j'} + H_a \quad (2.16)$$

where the first term is the kinetic energy, and $u_{\ell j}$ is the j'th component of the displacement of the ℓ'th atom from its equilibrium position. The second term is the harmonic part of the potential energy, where

$$A_{\ell j \ell' j'} = \left. \frac{\partial^2 V}{\partial u_{\ell j} \partial u_{\ell' j'}} \right|_o$$

and V is the potential energy of the whole crystal expressed in terms of the displacements of each atom. H_a is the anharmonic part of the potential which contains higher order derivatives of V. By Fourier transforming the momentum and position operators, the Hamiltonian can be written in the form[27]

$$H = \sum_{ki} (a^{\dagger}_{ki} a_{ki} + \tfrac{1}{2}) \hbar\omega_{ki} + H' \qquad (2.17)$$

where $a^{\dagger}_{ki} a_{ki}$ is the number operator for phonons of wave vector $\vec{k}$ and polarization i, with energy $\hbar\omega_{ki}$, and H' contains terms of higher order in the phonon operators.

Since the Hamiltonian can be written in the form of equation (2.1), then from (2.13), the thermal conductivity due to the phonons is

$$K = \frac{1}{(2\pi)^3} \sum_i \int C(\vec{k},i) v_G^2(\vec{k},i) \tau_T(\vec{k},i) \cos^2\theta_G(\vec{k},i) d^3k. \qquad (2.18)$$

At low temperatures, only the acoustic modes will be populated, so i runs over the three acoustic polarizations. Including the specific heat $C(\vec{k},i) = \hbar\omega(\vec{k},i) \partial N(\vec{k},i)/\partial T$ explicitly, the conductivity can be expressed as

$$K = \frac{k_B}{(2\pi)^3} \sum_i \int \left(\frac{\hbar\omega}{k_B T}\right)^2 \frac{e^{\hbar\omega/k_B T}}{\left(e^{\hbar\omega/k_B T}-1\right)^2} v_G^2(\vec{k},i) \times \tau_T(\vec{k},i)\cos^2\theta_G(\vec{k},i)\,d^3k \quad . \tag{2.19}$$

The integration over the first Brillouin zone can be split into integrals over the magnitude and over the direction of $\vec{k}$; i.e. $d^3k = k^2 d\Omega dk$, where Ω is a solid angle in reciprocal space. At low temperatures, the thermally excited phonons will occur at small values of k, where the dispersion curves are linear. Therefore,

$$\omega(\vec{k},i) = v(\Omega,i)k \tag{2.20}$$

where $v(\Omega,i)$ is the phase velocity of the phonon, which in the linear region is just the velocity of sound. The phase velocity depends only on direction but not on the magnitude of $\vec{k}$. Therefore, from (2.2) it can be shown that the group velocity also depends only on direction. Using (2.20), and letting $x = \hbar\omega/k_B T$, (2.19) can be expressed as

$$K = \frac{1}{(2\pi)^3} \frac{k_B^4 T^3}{\hbar^3} \sum_i \int \frac{v_G^2(\Omega,i)}{v^3(\Omega,i)} \cos^2\theta_G(\Omega,i) \times \int_0^{x_{max}} \frac{x^4 e^x}{(e^x-1)^2} \tau_T(x,\Omega,i)\,dx\,d\Omega \tag{2.21}$$

where $x_{max} = \hbar\omega_{max}/k_B T = \Theta_D/T$, and Θ_D is the Debye temperature of the solid. For MnF_2, $\Theta_D = 255$ K[33,34]. The function $x^4e^x/(e^x-1)^2$ has a broad peak with a maximum value at $x \approx 3.8$. Therefore, the most important phonons for heat conduction are

those with frequencies $\hbar\omega \approx 3.8\ k_B T$. Since this function becomes small for x larger than 3.8, then for low temperature $T << \Theta_D$, the upper limit of the x integration can be extended to infinity.

Equation (2.21) can be used to calculate the conductivity only if the phonon frequency depends linearly on wave vector. In cases where a large amount of dispersion is introduced, for example, by a strong resonant interaction of the phonons with an impurity mode, the more general expression (2.19) should be used. This will be discussed in more detail later in this section.

To use expression (2.21), one must be able to calculate the phonon phase and group velocities for any direction in the crystal. At low temperatures, the phonon wavelength is long compared to the lattice spacing, so the crystal acts like a continuum. For example, assuming a typical phonon velocity of 3×10^5 cm/sec, then at 1 K the wavelength of the dominant phonon is $\lambda_{dom} = 2\pi\hbar v/3.8\ k_B T \approx 400$ Å. Therefore, the velocities can be calculated from elastic continuum theory, which requires only a knowledge of the elastic constants of the solid. As shown in Appendix A, for a phonon wave vector with direction cosines ℓ_1, ℓ_2, and ℓ_3 along the Cartesian crystal axes, the three possible phase velocities v are given by the roots of the secular equation[35],

$$|\Gamma_{jk} - \delta_{jk}\rho v^2| = 0 \qquad (2.22)$$

where ρ is the density, and

$$\Gamma_{jk} = \sum_{i\ell} \ell_i \ell_\ell C_{ijk\ell}$$

and $C_{ijk\ell}$ is an elastic constant. The components of the corresponding group velocity are then[36]

$$v_{Gi} = \frac{1}{\rho v} \sum_{jk\ell} C_{ijk\ell} \ell_\ell e_j \sigma_k \qquad (2.23)$$

where $\hat{e}$ is the unit polarization vector of the phonon.

To make further progress in calculating the conductivity, the form of the relaxation time τ_T must be investigated. From (2.9), the total relaxation rate is given by the sum of the relaxation rates for the possible phonon scattering processes,

$$\tau_T^{-1}(\vec{k},i) = \sum_n \tau_n^{-1}(\vec{k},i). \qquad (2.24)$$

This assumes independent scattering probabilities for each process. This appears to be a valid assumption[29-31], although special attention should be paid to the phonon normal processes[31].

As pointed out previously, at low temperatures an important scattering mechanism is scattering from the boundaries of the sample. At sufficiently low temperatures all other scattering processes will become insignificant compared to the boundary scattering. From (2.15), the relaxation rate for boundary scattering for a cylindrical sample of diameter D is

$$\tau_b^{-1}(\Omega,i) = \frac{3\pi}{4} v_G(\Omega,i) \frac{\sin\theta_G(\Omega,i)}{D}. \qquad (2.25)$$

If this is the only significant scattering mechanism, then substituting (2.25) in (2.21), and performing the x integration, the boundary limited conductivity becomes

$$K_b = \frac{2}{45} \frac{k_B^4 T^3}{\hbar^3} D \sum_i \int \frac{v_G(\Omega,i)}{v^3(\Omega,i)} \frac{\cos^2\theta_G(\Omega,i)}{\sin\theta_G(\Omega,i)} d\Omega \qquad (2.26)$$

where

$$\int_0^\infty \frac{x^4 e^x}{(e^x-1)^2} dx = \frac{4\pi^4}{15} .$$

Thus, the boundary limited conductivity has a characteristic T^3 temperature dependence.

Often, to simplify the angular integration in (2.26), the isotropic approximation is made. The most important phonons in the angular integral are those along the heat flow direction, for which $\theta_G = 0$. The isotropic approximation consists of neglecting the angular dependence of the phonon velocities, and using only those velocities $\vec{v}_i$ along the heat flow direction. In an experiment, this is usually a symmetry direction, and it can be shown from (2.2) that along any symmetry axis $\vec{v}_G = \vec{v}$. Therefore, (2.26) becomes

$$K_b^c = \frac{2\pi^2}{45} \frac{k_B^4 T^3}{\hbar^3} D \sum_i \frac{1}{v_i^2} \qquad (2.27)$$

which is the usual Casimir[37] expression for the boundary limited conductivity. It has been pointed out by McCurdy et al.[32] that in many cases this is not a good approximation, and that the full expression (2.26) should be used.

Another important scattering process is scattering from point defects. These may be substitutional or interstitial impurity atoms, or vacancies in the lattice. Point defect

scattering can also be caused by the presence of more than one isotope in the crystal, although this will not be the case for MnF_2 which is isotopically pure. The point defect scattering rate is well described by a Rayleigh law[29,30,38],

$$\tau_p^{-1} = Bk^4 = B\omega^4/v^4 \qquad (2.28)$$

where B is a parameter which describes the strength of the scattering. Because of the ω^4 dependence, point defect scattering becomes important at higher temperatures. Its effect on the thermal conductivity is to gradually reduce the conductivity from its T^3 boundary limited value as the temperature increases.

At still higher temperatures, phonon-phonon scattering becomes important. In equation (2.17) the anharmonic part of the Hamiltonion, H' causes interactions between the phonons. The simplest anharmonic term is of the form $a^{\dagger}_{k_3} a_{k_2} a_{k_1}$ which indicates that two phonons $\vec{k}_1$ and $\vec{k}_2$ collide to form a third $\vec{k}_3$. All such three phonon processes conserve energy, but need not conserve momentum. Since all possible phonon wave vectors are contained in the first Brillouin zone, if $\vec{k}_3$ lies outside the zone, it can be brought back within it by the addition of a reciprocal lattice vector $\vec{G}$. This is known as an Umklapp process,

$$\vec{k}_1 + \vec{k}_2 = \vec{k}_3 + \vec{G} \qquad (2.29)$$

in which phonon momentum is not conserved. Therefore, this is a resistive scattering mechanism. If $\vec{k}_3$ does not lie outside

the first Brillouin zone, it is known as a Normal, or non-resistive process.

The scattering rates for these processes are[29-31]

$$\tau_u^{-1} = C_u \omega^2 T^3 e^{-\Theta_D/aT}$$

and

$$\tau_N^{-1} = C_N \omega^2 T^3 \qquad (2.30)$$

where C_u and C_N are parameters which give the strength of the scattering, and a has a value of order unity. At high temperatures, Umklapp scattering dominates all others. This leads to a conductivity which decreases with increasing temperature. Between the Umklapp and boundary scattering regimes, the conductivity reaches a peak. The height of this peak is dependent on the amount of point defect and normal process scattering. The temperatures of interest in this work are well below the conductivity peak for MnF_2, so phonon-phonon scattering will not be considered further.

In some cases[39,40] impurities with internal energy levels may produce strong phonon scattering at discrete resonant frequencies. Resonant scattering will cause a "dip" in the thermal conductivity approximately at a temperature T given by 3.8 $k_B T = \hbar\omega_o$, where ω_o is the resonant frequency of the impurity. At this temperature, the most important phonons for heat conduction will be strongly scattered since their frequency equals the resonant frequency.

Resonant scattering also leads to dispersion. Coupled phonon-impurity modes are created in the region of the spectrum where the phonon frequency is close to the resonant frequency. This leads to a gap in the phonon dispersion curve, which shifts the phonon frequency for each wave vector, and alters the dispersion relations. These effects have recently been demonstrated experimentally for the system KCl:CN[41].

The dispersion and scattering are not independent. In principle, they can be related respectively to the real and imaginary parts of a complex index of refraction for the phonon, which are connected by Kramers-Kronig relations. A general theory for the dispersion and scattering due to resonant interactions with impurities has been developed by Walton[42,43]. It is found that the fractional phonon frequency shift can be expressed as

$$\frac{\Delta\omega}{\omega} = \frac{A\rho_i}{\omega'^2-\omega_o^2}\tanh\frac{\hbar\omega_o}{2k_BT} \qquad (2.31)$$

where $\Delta\omega = \omega'-\omega$, ω' and ω being the perturbed and unperturbed frequencies for a given wave vector. A is a parameter which gives the strength of the scattering, and ρ_i is the number of resonant scatterers per unit volume. The parameter A can be expressed as[42,43]

$$A = \frac{W^2\omega_o}{\hbar\rho v^2} \qquad (2.32)$$

where ρ is the crystal density, and W is a coupling constant which gives the shift of the impurity energy levels for a unit

applied strain. The tanh function in (2.31) occurs because at high temperatures, $k_B T >> \hbar\omega_o$, the impurity ground and excited states will be equally populated, so phonon energy gain and energy loss processes will cancel[41].

The relaxation rate due to the resonant scattering is given by[42,43]

$$\tau_R^{-1} = \frac{2A^2 \rho_i v^2}{\pi v'^4 v_G'} \frac{\omega'^4}{(\omega'^2 - \omega_o^2)^2} \tanh \frac{\hbar\omega_o}{2k_B T} \qquad (2.33)$$

where $v' = \omega'/k$ is the perturbed phase velocity, $\vec{v}_G' = \vec{\nabla}_k \omega'$ is the perturbed group velocity, and ω' can be calculated from (2.31). In general, the dispersion introduced by the resonant interaction should be included in calculating the conductivity[42,43]. Since the phonon frequency no longer depends linearly on wave vector, the new phonon frequencies and velocities should be calculated from (2.31) and used in expression (2.19) for the conductivity.

To extract information about the phonon scattering from thermal conductivity measurements, the conductivity is calculated numerically in terms of parameters for each scattering process. These are then adjusted to give agreement with the measured temperature dependence of the conductivity.

C. Tunneling States

Tunneling states[26] form an important class of impurity modes which can resonantly scatter phonons. They are formed when a molecule substitutes for an ion in a crystal lattice in

such a way that it has several equilibrium orientations in its lattice site and can perform a tunneling motion between them.

Devonshire[44] calculated how the rotational states of a linear molecule were modified when placed in a crystal field. The energy levels of a free rotor are

$$\varepsilon_J = BJ(J+1) \tag{2.34}$$

where J is the rotational angular momentum quantum number, and B is the rotational constant; $B = \hbar^2/2I$, where I is the moment of inertia of the molecule. Devonshire postulated a Hamiltonian[44]

$$H_{Dev} = B(J^2/\hbar^2 + V(\Omega)) \tag{2.35}$$

where $V(\Omega)$ is a function with potential wells in N_w directions (where N_w depends on the symmetry of the lattice), and potential barriers between them.

By solving the Schrodinger equation associated with (2.35), the energy levels were calculated as a function of the barrier height, for the case of octahedral crystal fields[44,45]. It was found that as the barrier height increased from zero, some of the 2J+1 rotational degeneracy was removed, and the resulting states could be described as hindered rotors. As the barriers became higher, the energy levels clustered into groups, with small splittings between the members of each group.

The nature of these states can be seen by considering a tunneling model[46-48]. In the limit of infinite potential barriers, the molecule will be locked into one of the N_w potential

wells. In the well, the molecule can undergo an angular oscillatory motion called libration. The energy levels of a librator are just harmonic oscillator levels,

$$\varepsilon_n = (n+1)\hbar(K/I)^{1/2} \tag{2.36}$$

where K is a force constant. Each librator level is $N_w(n+1)$-fold degenerate, since a two-dimensional harmonic oscillator is (n+1)-fold degenerate, and there are N_w equivalent wells. If the barrier is large but finite, the possibility exists of tunneling between the wells. This removes some of the degeneracy, and each librator level splits into several tunneling levels, separated by small tunnel splittings. It can be shown[47] that these are equivalent to the levels found in the large barrier limit of the hindered rotor model.

The origin of the tunnel splitting can be illustrated by considering the ground state of a simple two well system, as shown in Fig. 2.1. There are two equivalent wells V_A and V_B. If the wells did not overlap, the ground state librator wavefunctions would be $|a\rangle$ and $|b\rangle$, localized in wells A and B respectively. The energy level ε_o would be twofold degenerate, where

$$\varepsilon_o = \langle a|H_A|a\rangle = \langle a|T+V_A|a\rangle$$

or (2.37)

$$\varepsilon_o = \langle b|H_B|b\rangle = \langle b|T+V_B|b\rangle \ .$$

If the barrier is finite, the Hamiltonian of the system is described by

FIG. 2.1 A model double well potential for tunneling states. The labels are defined in the text.

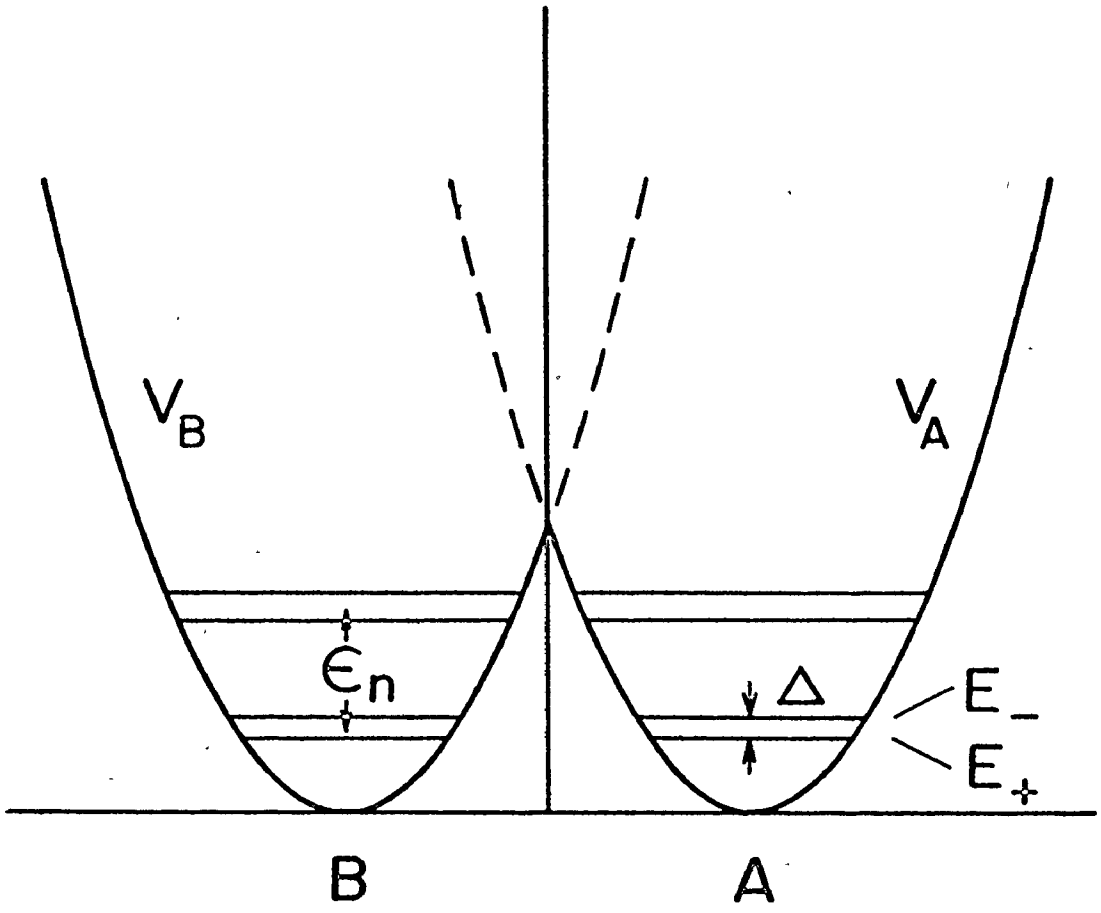
V_B
V_A
ϵ_n
Δ
E_-
E_+
B
A

$$H = \begin{cases} T + V_A & \text{in region A} \\ T + V_B & \text{in region B .} \end{cases} \tag{2.38}$$

The localized states are no longer the correct eigenstates, since the overlap integral,

$$\eta = \langle a|H|b\rangle = \langle b|H|a\rangle \tag{2.39}$$

is not zero. The problem is to find linear combinations of $|a\rangle$ and $|b\rangle$ which diagonalize the Hamiltonian. The obvious choice is the symmetric and antisymmetric combinations,

$$\text{and} \qquad \begin{aligned} |\psi_+\rangle &= (|a\rangle+|b\rangle)/[2(1+S)]^{1/2} \\ |\psi_-\rangle &= (|a\rangle-|b\rangle)/[2(1-S)]^{1/2} \end{aligned} \tag{2.40}$$

where S in the normalization factor is the wavefunction overlap,

$$S = \langle a|b\rangle. \tag{2.41}$$

It is easy to show that $\langle\psi_+|H|\psi_-\rangle = \langle\psi_-|H|\psi_+\rangle = 0$, and that the new energy levels are

$$\text{and} \qquad \begin{aligned} E_+ &= \langle\psi_+|H|\psi_+\rangle = (E_o+\eta)/(1+S) \\ E_- &= \langle\psi_-|H|\psi_-\rangle = (E_o-\eta)/(1-S) \end{aligned} \tag{2.42}$$

where

$$E_o = \langle a|H|a\rangle = \langle b|H|b\rangle. \tag{2.43}$$

Therefore, the degeneracy is removed.

This approach is valid if the localized states provide an adequate basis for the exact wavefunctions. This requires

that the overlap $S << 1$, so S can be neglected in (2.42). Moreover, from the definitions (2.39) and (2.43), it can be shown[46] that

$$E_o = \varepsilon_o + \langle a|V_B - V_A|a\rangle_B$$

and

$$\eta = \varepsilon_o S + \langle a|V_B - V_A|b\rangle_B$$

where the integration is carried out only over the B region of space. Since $|a\rangle$ is small in this region, the second term in E_o can be neglected. Because S is small, the first term in η can be ignored, and since $V_B < V_A$ in region B, the second term is negative. Therefore, $\eta < 0$, so the symmetric state has the lower energy. Equations (2.42) can therefore be expressed as

$$\text{and} \qquad \begin{aligned} E_+ &\simeq \varepsilon_o - \Delta/2 \\ E_- &\simeq \varepsilon_o + \Delta/2 \end{aligned} \qquad (2.44)$$

where $\Delta = -2\eta$ is the tunnel splitting, as shown in Fig. 2.1.

This approach was originally applied by Gomez et al.[46] to the case of a single ion impurity which has off-centre equilibrium positions in its lattice site, such as the KCl:Li system. In this situation, the localized states are translational harmonic oscillators. However, the general formalism applies equally well to the case of angular harmonic oscillators (librators)[47,48].

The potential of the impurity is implicitly a function of the coordinates of its neighbouring ions in the lattice. This can be expanded in a Taylor's series about their equilibrium

positions,

$$V(x_{ij}) = V(x^{o}_{ij}) + \sum_{ij} u_{ij} \frac{\partial V}{\partial x_{ij}} + \ldots \qquad (2.45)$$

where x_{ij} is the j'th coordinate of the i'th neighbour, and u_{ij} is its displacement from equilibrium. The first term is the impurity potential due to the static host lattice. This is the potential that appears in the impurity Hamiltonian (2.38). Since the u_{ij}'s can be expressed in terms of phonon operators, the second term leads to interactions between the impurity modes and the lattice vibrations. Thus, phonons which cause transitions between the tunneling levels can be resonantly scattered.

D. Heat Pulses

In a heat pulse experiment[49], a pulse of thermal phonons is generated at one end of the sample under study, and detected at the other. Usually the pulse is created by applying a voltage pulse to a thin film metal heater evaporated onto one polished face of the crystal, in order to achieve good thermal contact. The detector consists of a thin film bolometer evaporated onto the opposite face. To achieve maximum temperature sensitivity, the bolometer is usually a superconductor kept close to its transition temperature.

The experiments are performed at low temperatures, where the intrinsic phonon mean free path is long compared to the length of the sample (i.e. the boundary scattering regime in

thermal conductivity). Then, in a pure crystal, phonons will travel between the generator and detector without being scattered, which is known as ballistic propagation. Therefore, the pulses due to different polarizations will arrive separately at the detector at times $t_o = L/v_G(\Omega,i)$, where L is the path length, and v_G is the group velocity for polarization i, along the direction Ω, which is determined by the sample geometry. Thus, thermal transport by phonons of each mode (Ω,i) can be studied in a heat pulse experiment. This is in contrast to a thermal conductivity experiment, which, as shown in section B, measures only an average over all modes.

If there are impurities in the crystal which scatter the ballistic phonons, then each heat pulse will be attenuated by a factor $\exp[-t_o/\tau(\Omega,i)]$, where τ is an average relaxation time for the mode (Ω,i). Thus, heat pulse experiments can be used to study the modal dependence of the scattering. In order to calculate this attenuation, it is first necessary to have a model for the ballistic pulse heights.

Unlike an ultrasonics experiment, the phonons generated in a heat pulse experiment do not form a coherent plane wave, but rather are incoherent thermal phonons which travel out in all directions in the sample. Those phonons which have group velocities along the heater-detector direction will be detected by the bolometer. Because of elastic anisotropy, the group

velocity of a phonon will in general differ in magnitude and direction from its phase velocity. This has two important consequences.

Usually, the sample is arranged so that the heater-detector direction is along a symmetry axis of the crystal. Along such a direction, the group and phase velocities are equal, so there will be, in general, three heat pulses corresponding to the three polarizations with velocities given by (2.22). There may also be extra heat pulses, due to the fact that phonons with phase velocities in other directions may have their group velocities along the heater-detector direction. These extra heat pulses have been noted in several experiments[49,50]. Secondly, it can happen for some modes that a large number of the phonons emitted by the heater, with phase velocities spread over a wide angular range, all have their group velocities along the heater-detector direction. Thus, thermal energy is "focused" into this direction, which produces an enhancement of the heat pulse associated with this mode. These phonon focusing effects have been calculated and measured in some materials by Taylor et al.[51].

The other factor which affects the ballistic pulse heights is the number of phonons of each polarization produced in the sample by the heater. A general theory for heat transport across an interface between two media has been developed by Little[52]. Consider two solids with a plane boundary between them. For simplicity, both media are assumed to be isotropic,

and at first only a single polarization is considered. The number of phonons per unit time incident on a unit area of the boundary with frequencies between ω and $\omega+d\omega$, and angles of incidence between θ_1 and $\theta_1 + d\theta_1$ in medium 1 is

$$\frac{1}{2} v_1 N_1(\omega)\cos\theta_1 \sin\theta_1 d\theta_1 d\omega \tag{2.46}$$

where $N_1(\omega)$ is the number of phonons in medium 1 with frequency ω, and v_1 is their velocity.

Some of these will be reflected, and some will be refracted into the second medium at an angle between θ_2 and $\theta_2 + d\theta_2$. These angles are related by an acoustic Snell's law,

$$\frac{\sin\theta_1}{\sin\theta_2} = \frac{v_1}{v_2} \, . \tag{2.47}$$

A similar expression to (2.46) is obtained for the number of phonons in medium 2 travelling towards the interface between θ_2 and $\theta_2 + d\theta_2$. Therefore, the net heat flux across the boundary is

$$\begin{aligned} Q_{12} = &\frac{1}{2} \iint \hbar\omega N_1(\omega) v_1 \alpha_1(\theta_1) \cos\theta_1 \sin\theta_1 d\theta_1 d\omega \\ &- \frac{1}{2} \iint \hbar\omega N_2(\omega) v_2 \alpha_2(\theta_2) \cos\theta_2 \sin\theta_2 d\theta_2 d\omega \end{aligned} \tag{2.48}$$

where $\alpha_1(\theta_1)$ is the transmission coefficient of the interface for phonons incident at θ_1 in medium 1. By the principles of detailed balance, $\alpha_1(\theta_1) = \alpha_2(\theta_2)$.

The frequency distribution is given by[52]

$$N(\omega) = \frac{1}{2\pi^2}\frac{1}{v^3}\frac{\omega^2}{e^{\hbar\omega/k_BT}-1} . \tag{2.49}$$

Substituting (2.49) into (2.48), the heat flux becomes

$$Q_{12} = \frac{\hbar}{4\pi^2}\left(\frac{\Gamma_1}{v_1^2}\int \frac{\omega^3}{e^{\hbar\omega/k_BT_1}-1}\,d\omega - \frac{\Gamma_2}{v_2^2}\int \frac{\omega^3}{e^{\hbar\omega/k_BT_2}-1}\,d\omega\right) \tag{2.50}$$

where

$$\Gamma = \int_0^{\pi/2} \alpha(\theta)\sin\theta\cos\theta\,d\theta \tag{2.51}$$

is the total transmission coefficient for each medium. Making the substitution $x = \hbar\omega/k_BT$, and performing the x integrations, (2.50) becomes

$$Q_{12} = \frac{\pi^2}{60}\frac{k_B^4}{\hbar^3}\left(\frac{\Gamma_1}{v_1^2}T_1^4 - \frac{\Gamma_2}{v_2^2}T_2^4\right) , \tag{2.52}$$

since

$$\int_0^\infty \frac{x^3}{e^x-1}\,dx = \frac{\pi^4}{15}$$

where at low temperatures, the upper limit of the x integration can be extended to infinity.

Using (2.47) it is easy to show from (2.51) that

$$\Gamma_2 = \frac{v_2^2}{v_1^2}\int_0^{\pi/2} \alpha_1(\theta_1)\sin\theta_1\cos\theta_1\,d\theta_1 = \frac{v_2^2}{v_1^2}\Gamma_1 . \tag{2.53}$$

Therefore, (2.52) becomes

$$Q_{12} = \frac{\pi^2}{60} \frac{k_B^4}{\hbar^3} \frac{\Gamma_1}{v_1^2} (T_1^4 - T_2^4). \qquad (2.54)$$

This expression has the form of a black-body radiation model for phonons. Generalizing to the case of three polarizations, the heat flux from the heater into the sample can be expressed as

$$Q_{hs} = \frac{\pi^2}{60} \frac{k_B^4}{\hbar^3} \left(\frac{\Gamma_{hL}}{v_{hL}^2} + 2\frac{\Gamma_{hT}}{v_{hT}^2}\right) (T_h^4 - T_s^4) \qquad (2.55)$$

where L and T refer to longitudinal and transverse polarizations, and h and s refer to the heater and the sample.

Several attempts have been made to calculate and measure the transmission coefficients[52-54]. In the perfect-coupling model[54], the transmission coefficients are assumed to have their maximum value of $\frac{1}{2}$. It has been pointed out[55] that the thermal relaxation time of the heater to the sample must be very short. Otherwise, the application of typical pulse powers of several watts to the thin film heater would burn it out. With the perfect-coupling assumption, (2.55) becomes

$$\begin{aligned} Q_{hs} &= \frac{\pi^2}{120} \frac{k_B^4}{\hbar^3} \left(\frac{1}{v_{hL}^2} + \frac{2}{v_{hT}^2}\right) (T_h^4 - T_s^4) \\ &= \sigma (T_h^4 - T_s^4) \end{aligned} \qquad (2.56)$$

where σ has the form of a Stefan-Boltzmann constant for phonon radiation.

The height of a heat pulse is proportional to the heat flux falling on the detector. For ballistic propagation, this is

proportional to the heat flux across the heater-sample boundary. Since virtually all the heat goes into the sample, this is just the power delivered to the heater, P_h divided by its area, A_h. Therefore, the height of any ballistic heat pulse is

$$I_B \propto P_h/A_h \ . \tag{2.57}$$

Moreover, from (2.56) it can be seen how this heat flux is divided among the polarizations. The height of a longitudinal or transverse pulse will be proportional to the inverse square of the velocity of that polarization in the heater,

$$I_{Bi} \propto 1/v_{hi}^2 . \tag{2.58}$$

The perfect-coupling black-body model contains many simplifying assumptions. Nevertheless, in many cases[54,56] it has been found to give good agreement with experimental results.

If there are impurities in the crystal which scatter the phonons, the heat pulses will be attenuated. Since the scattering rates are frequency dependent (for example, point defect or resonant scattering), it is necessary to know the frequency distribution in the heat pulses in order to calculate their attenuation. Returning to equation (2.50), the heat flux for the perfect-coupling model can be expressed as

$$Q_{hs} = \frac{\hbar}{8\pi^2}\left(\frac{1}{v_{hL}^2} + \frac{2}{v_{hT}^2}\right)\int \left(\frac{\omega^3}{e^{\hbar\omega/k_B T_h}-1} - \frac{\omega^3}{e^{\hbar\omega/k_B T_s}-1}\right)d\omega \ . \tag{2.59}$$

Therefore, letting $x = \hbar\omega/k_B T_h$, the height of a ballistic pulse can be written as

$$I_{Bi} \propto \frac{1}{8\pi^2} \frac{k_B^4 T_h^4}{\hbar^3} \frac{1}{v_{hi}^2} \int g(x,T_h,T_s)dx \qquad (2.60)$$

where the heat pulse frequency distribution function is

$$g(x,T_h,T_s) = \frac{x^3}{e^x-1} - \frac{x^3}{e^{(T_h/T_s)x}-1} . \qquad (2.61)$$

Therefore, the frequency distribution is characterized by the sample temperature T_s and the heat pulse temperature T_h, which can be calculated from (2.56), knowing σ and the power density delivered to the heater, $Q_{hs} = P_h/A_h$. For low power densities, $T_h = T_s + \Delta T$, it can be shown[55] from (2.61) that

$$g(x,T_h,T_s) \simeq \frac{\Delta T}{T_s} \frac{x^4 e^x}{(e^x-1)^2} \qquad (2.62)$$

which is the same as the frequency distribution in a thermal conductivity experiment. It has a broad peak at $x \simeq 3.8$. For higher power densities, $T_h >> T_s$, it is found that

$$g(x,T_h,T_s) \simeq \frac{x^3}{e^x-1} \qquad (2.63)$$

which has a broad peak centred at $x \simeq 2.8$. Therefore, the most important phonons for carrying heat are those with frequencies $\hbar\omega = C\, k_B T_h$, where C is a number between 3.8 and 2.8. This is another advantage of a heat pulse experiment over a thermal conductivity experiment. By changing the power delivered to the heater, the frequency distribution of the phonons can be varied independently of the ambient sample temperature.

If a phonon mode is scattered with a total relaxation

time τ_{Ti}, the height of its heat pulse will be reduced to

$$I'_{Bi} \propto \frac{1}{8\pi^2} \frac{k_B^4 T_h^4}{\hbar^3} \frac{1}{v_{hi}^2} \int g(x,T_h,T_s) e^{-t_o/\tau_{Ti}(x)} dx \qquad (2.64)$$

where t_o is the arrival time at the bolometer. Therefore, using (2.60), the heat pulse is attenuated by a factor

$$\frac{I'_{Bi}}{I_{Bi}} = \frac{15}{\pi^4} \frac{T_h^4}{T_h^4 - T_s^4} \int g(x,T_h,T_s) e^{-t_o/\tau_{Ti}(x)} dx \; . \qquad (2.65)$$

The heat which is scattered out of the ballistic heat pulse will arrive diffusively at the detector after the ballistic pulse. The form of this diffusive heat flow has been investigated by Ackerman and Guyer[57]. They found solutions to the modified heat flow equation,

$$\frac{1}{2} \tau \frac{\partial^2 T}{\partial t^2} + \frac{\partial T}{\partial t} = \frac{K}{C} \nabla^2 T \qquad (2.66)$$

where τ is an average phonon relaxation time, K is the thermal conductivity, and C is the specific heat. The first term in (2.66), which is not usually included in the heat flow equation, is necessary to prevent the heat pulse from propagating with infinite velocity[57]. The solution to (2.66) was found using Laplace transform techniques. For a cylindrical sample of length L, with an input temperature pulse of height I_B and duration Δt applied at one end, the temperature signal at the other end was found to be

$$\begin{aligned} I(t) = {} & I_B e^{-t/\tau} \theta(t-t_o) \theta(t_o+\Delta t-t) \\ & + \frac{\Delta t}{\tau} I_B e^{-t/\tau} \left(I_o(z) + \frac{t}{\tau} \frac{I_1(z)}{z} \right) \theta(t-t_o) \end{aligned} \qquad (2.67)$$

where $t_o = L/v$ is the arrival time, $z = (t^2-t_o^2)^{1/2}/\tau$, and I_o and I_1, are hyperbolic Bessel functions.

The first term in (2.67) is just the attenuated ballistic heat pulse I_B'. The second term represents the diffusive signal I_D. For long relaxation times, the second term produces a diffusive tail on the ballistic heat pulse. As τ becomes shorter, the ballistic heat pulse becomes smaller, and I_D becomes a broad diffusive ramp. Attempts have been made to compare this model to experiment[58]. The general shape of the diffusive heat signal agrees qualitatively with (2.67), but quantitative agreement is often lacking.

In the above discussion, the relaxation time was assumed to be dominated by resistive scattering processes. If normal processes are dominant, the heat pulse can propagate as a temperature pulse, or "second sound"[57,59]. This occurs only in extremely pure crystals, so it does not need to be considered in the present experiments.

E. Magnon Conductivity

It is well known that at low temperatures some materials become antiferromagnetically ordered, with the magnetic moments of the ions pointing alternately parallel and antiparallel to a particular direction. The elementary excitations of such a system are quantized spin deviation waves called magnons.

The Hamiltonian for a simple antiferromagnet can be expressed as[28]

$$H = - J \sum_{j,\delta} \vec{S}_j \cdot \vec{S}_{j+\delta} - g\mu_B H_A \left(\sum_j S^a_{jz} - \sum_j S^b_{jz}\right) - g\mu_B H \sum_j S_{jz} \quad (2.68)$$

where $\vec{S}_j$ is the spin on the j'th magnetic ion, g is the g factor, and μ_B is the Bohr magneton. The first term is the Heisenberg exchange Hamiltonian, and J is the exchange constant. If J is negative, it favours antiparallel alignment of the spins. The sum over δ is over the nearest neighbours to each magnetic ion. It has been assumed that the lattice could be divided into two interpenetrating sublattices a and b, for parallel and antiparallel alignment, such that the nearest neighbours to an ion on a lie on b and vice versa. Because of magnetic dipole forces and residual spin-orbit effects, there are anisotropic energy terms which favour alignment of the spins along particular crystallographic directions. These have been approximated by an anisotropy magnetic field H_A which favours the alignment of a spins along the +z direction, and b spins along the -z direction. The application of an external magnetic field $\vec{H}$ along the +z direction lowers the energy of a spins and raises the energy of b spins.

By writing (2.68) in terms of spin deviation operators, transforming to spin wave operators, and diagonalizing the Hamiltonian[28], it can be expressed as

$$\begin{aligned} H = & -Ng\mu_B(H_A+H_E) + \sum_q (\alpha_q^\dagger \alpha_q + \tfrac{1}{2})\hbar\omega_q^+ \\ & + \sum_q (\beta_q^\dagger \beta_q + \tfrac{1}{2})\hbar\omega_q^- + H' \end{aligned} \quad (2.69)$$

where N is the total number of spins, H_E is the effective exchange field, defined by $g\mu_B H_E = 2z|J|S$, where z is the number of nearest neighbours, $\alpha_q^\dagger \alpha_q$ is the number operator for magnons of wave vector $\vec{q}$ and energy $\hbar\omega_q^+$, and $\beta_q^\dagger \beta_q$ for those with energy $\hbar\omega_q^-$, and H' contains terms of higher order in the magnon operators.

The magnon dispersion relations are

$$\hbar\omega^{\pm}(\vec{q}) = g\mu_B[(H_A+H_E)^2 - H_E^2\gamma_q^2]^{1/2} \pm g\mu_B H \qquad (2.70)$$

where

$$\gamma_q = \frac{1}{z}\sum_{\delta} e^{i\vec{q}\cdot\vec{\delta}} \quad .$$

For example, for a bcc lattice with lattice constant a,

$$\gamma_q = \cos(\frac{aq_x}{2})\cos(\frac{aq_y}{2})\cos(\frac{aq_z}{2}) \quad .$$

The two signs in (2.70) indicate that when an external field is applied along the z axis, the dispersion curve breaks into two branches, one being raised and the other lowered by an amount $g\mu_B H$.

The effect of anisotropy can be seen from (2.70). For $q = 0$, $\gamma_q = 1$, and

$$\hbar\omega^{\pm}(o) = g\mu_B(2H_E H_A + H_A^2)^{1/2} \pm g\mu_B H \quad . \qquad (2.71)$$

Therefore, the anisotropy produces a gap in the spectrum. Unlike phonons, the magnon frequency does not become zero at zero wave vector. Also because of the anisotropy, ω_q does not vary linearly with q even for small wave vectors. Usually $H_A \ll H_E$,

so (2.71) defines a critical field

$$H_c = (2H_E H_A)^{1/2} \tag{2.72}$$

in the sense that the application of an external field of magnitude H_c will bring the lower magnon branch down to $\omega_q = 0$ at $q = 0$. For example, for MnF_2 the critical field has been found to be $H_c = 93$ kOe[60]. Therefore, the gap in the magnon spectrum is $\hbar\omega(0)/k_B = g\mu_B H_c/k_B = 12.5$ K. When the critical field is exceeded, the spins abruptly "flop" into the xy plane so as to be perpendicular to the applied field. As shown in Appendix D, this is a lower energy configuration.

It has been shown theoretically[1] that the magnons can contribute to the heat current in a thermal conductivity experiment. Since the spin wave Hamiltonian can be written in the general form of equation (2.1), then using (2.13) the magnon conductivity is

$$K_m = \frac{1}{(2\pi)^3} \sum_j \int C(\vec{q},j) v_G^2(\vec{q},j) \tau_T(\vec{q},j) \cos^2\theta_G(\vec{q},j) d^3q \tag{2.73}$$

where j refers to the two dispersion curve branches. Including the specific heat explicitly, (2.73) becomes

$$K_m = \frac{k_B}{(2\pi)^3} \sum_j \int \left(\frac{\hbar\omega}{k_B T}\right)^2 \frac{e^{\hbar\omega/k_B T}}{(e^{\hbar\omega/k_B T} - 1)^2} v_G^2(\vec{q})\ \tau_T(\vec{q},j) \cos^2\theta_G(\vec{q}) d^3q \tag{2.74}$$

where $\omega(\vec{q},j)$ is given by (2.70), and $\vec{v}_G(\vec{q}) = \vec{\nabla}_q \omega(\vec{q},j)$. Since the magnon frequency does not vary linearily with wave vector, this integral cannot be simplified as it was in the phonon case. The integral extends over the magnetic first Brillouin zone

which is half as large as the phonon zone.

As in the phonon case, at low enough temperatures, the magnon mean free path will be limited only by the boundaries of the sample. Therefore, from (2.14) the boundary limited magnon conductivity for a cylindrical sample of diameter D is

$$K_m^b = \frac{k_B}{6\pi^4} D \sum_j \int \left(\frac{\hbar\omega}{k_B T}\right)^2 \frac{e^{\hbar\omega/k_B T}}{(e^{\hbar\omega/k_B T}-1)^2} |\vec{\nabla}_q \omega(\vec{q})| \frac{\cos^2\theta_G(\vec{q})}{\sin\theta_G(\vec{q})} d^3q \ . \qquad (2.75)$$

At higher temperatures, other magnon scattering processes become possible. Impurity ions with different spins or exchange constants can substitute for magnetic ions in the crystal. It has been shown for ferromagnets[61] that the magnon relaxation rate due to these magnetic defects has a Rayleigh form,

$$\tau_{md}^{-1} = Dq^4 \qquad (2.76)$$

similar to that for point defect scattering of phonons. The magnetic defects can also produce resonance impurity modes in the spin wave spectrum[62] which could act like resonant magnon scatterers[61].

The higher order terms in the Hamiltonian (2.69) will lead to magnon-magnon interactions. As in the phonon case, these can be either Normal or Umklapp processes. It has been shown[61] that the Normal processes by themselves cannot produce thermal resistance to the magnon heat current. Moreover, as in the case of phonons, the magnon Umklapp processes become exponentially unimportant at low temperatures[63]. Although there have been some theoretical predictions[61], the relaxation rates for these

magnon scattering mechanisms have not been tested experimentally.

So far, it has not been mentioned that the magnons and phonons can interact with each other. The interaction is strongest at the point where the magnon and phonon dispersion curves cross, since at this point energy and wave vector can be conserved in a one phonon -one magnon interaction. The cross-over point can be found by equating expressions (2.20) and (2.70). At the point of intersection, a gap is introduced into the dispersion curves, and near this gap the excitations are neither phonons nor magnons, but coupled magnetoelastic modes.

Magnetoelastic interactions occur because the phonon strain field modulates the spacings between magnetic ions. This in turn affects the exchange and magnetic dipole interactions between the ions and the crystal field around each ion[64]. Regardless of its microscopic origin, the magnetoelastic interaction can be described by a semiclassical model. The total energy per unit volume of the crystal can be expressed as the sum of a magnetic energy, an elastic energy, and an interaction term[65],

$$E = E_M(m_{ij}) + E_E(e_{k\ell}) + E_{ME}(m_{ij}, e_{k\ell}) \qquad (2.77)$$

where m_{ij} is the j'th component of the i'th sublattice magnetization, and $e_{k\ell}$ is a strain component. For a uniaxial antiferromagnet with exchange constant λ, anisotropy constant K, and magnetoelastic coupling constant b, this can be expressed as[60]

$$E = -\lambda \vec{m}_1 \cdot \vec{m}_2 - \frac{1}{2}\frac{K}{m_s^2}(m_{1z}^2 + m_{2z}^2) + \frac{1}{2} C_{44}(e_{zx}^2+e_{yz}^2) + \frac{b}{m_s}[(m_{1x}-m_{2x})e_{zx} + (m_{1y}-m_{2y})e_{yz}] \quad (2.78)$$

where $m_s = |\vec{m}_1| = |\vec{m}_2|$ is the sublattice magnetization. Only the strains relative to the coupling have been included in the elastic term, and the magnetoelastic term is correct to first order in the strains.

Equations of motion for the elastic and magnetic variables can be derived from (2.78) and solved to find the dispersion relations for the coupled modes[65]. The size of the gap in the spectrum depends on the magnitude of the coupling constant b. If this is large, then in the region around the gap, the conductivity should be calculated for the coupled magnetoelastic modes, rather than separately for the magnons and phonons[7,17].

The relaxation rate for a magnetoelastic mode is a combination of a magnon-like and a phonon-like rate. If the magnon scattering rate is much larger than that for the phonons, the contribution of the coupled modes to the thermal conductivity can be much less than that which the phonons near the crossover would have contributed in the absence of any magnetoelastic coupling. Therefore, a band of phonons near the crossover is effectively removed from the heat carrier spectrum. In this case, the magnons act in much the same way as a resonant phonon scatterer. This type of behaviour has been found in $GdCl_3$[5,13], $MnCl_2 \cdot 4H_2O$[13,16], and $FeCl_2$[17].

Higher order interactions such as one phonon-two magnon processes are also possible. Theoretical analyses of these interactions have been developed for ferromagnets[66,67], ferrimagnets[68], and antiferromagnets[69]. Unlike the one phonon-one magnon process, these interactions are not limited to a narrow range of frequency and wave vector. Therefore, they are important in establishing thermal equilibrium between the magnon and phonon systems[63]. In Chapter V it will be shown that the question of equilibrium between the two systems may be very important in discussing magnon conductivity.

CHAPTER III

EXPERIMENTAL APPARATUS AND METHODS

A. Thermal Conductivity Apparatus

All the MnF_2 samples used in these experiments were obtained from Optovac Inc., and were of the highest purity available. The thermal conductivity results which will be presented in Chapter IV were obtained using sample TC3. This consisted of a cylinder, 0.856 cm in diameter and 5.0 cm long, with its axis along the [001] crystallographic direction. This orientation was checked by back reflection Laue techniques and found to be correct to within 2°.

The sample was clamped by means of a phosphor bronze spring (AA) to a copper post (BB) connected to the copper bottom of the He^3 pot (CC) of the cryostat. (The letters in parentheses refer to the labels in Figs. 3.1 and 3.2). To achieve good thermal contact, all the clamps were faced with indium and coated with a thin layer of Apiezon J oil. The crystal heater (DD) was similarly clamped to the lower end of the sample. The heater consisted of a winding of constantan wire with a room temperature resistance of 110 Ω.

The thermometer clamps (EE) and (FF) were then attached to the crystal between the heater and post. For thermometers

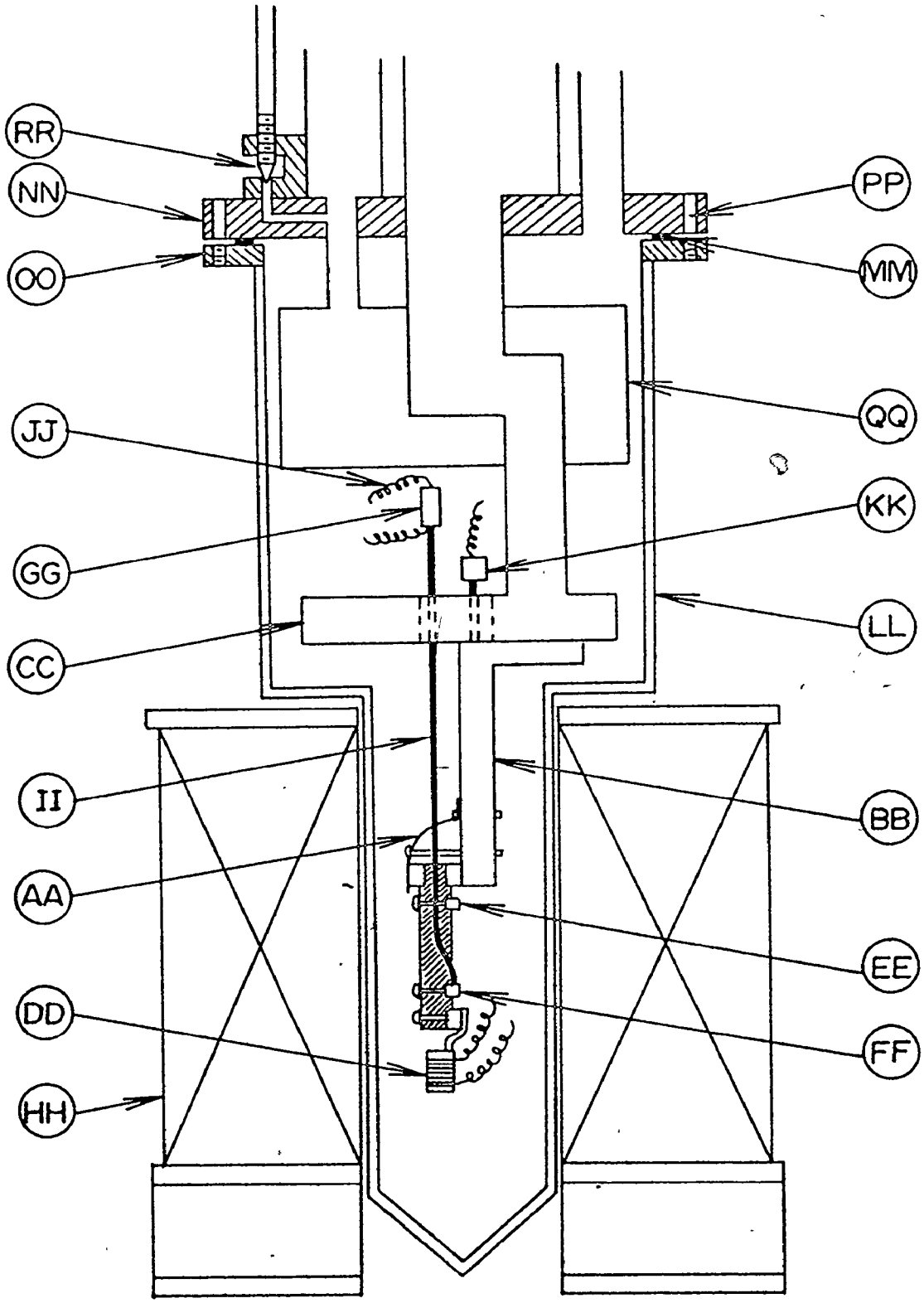
RR
NN
OO
PP
MM
QQ
JJ
KK
GG
LL
CC
II
BB
AA
EE
DD
FF
HH

two Speer 470 Ω carbon resistors (GG) were used. To prevent large magnetoresistance corrections, these were held out of the strong magnetic field of the 60 kOe superconducting magnet (HH) by lengths of 20 gauge copper wire (II) which protruded through the doughnut shaped He^3 pot. The thermometers were connected to the thermometer leads by 5 inch lengths of 40 gauge constantan wire (JJ). Since constantan is a poor thermal conductor at low temperatures, these prevented heat from leaking from the thermometers to the leads, which were thermally anchored to the He^3 pot. The temperature of the upper end of the sample could be adjusted by means of the post heater (KK). This consisted of a 100 Ω wire-wound resistor, soldered to the post.

After the crystal was mounted, the copper can (LL) surrounding the sample space was raised and fastened to the cryostat. The can was sealed by an indium O-ring (MM) laid between the flanges (NN) and (OO), and compressed by the screws (PP). The sample space was evacuated through valve (a) using a portable helium leak detector, which was then used to check the O-ring seal.

The magnet dewar (A) was raised around the cryostat so that the tail of the sample can fitted into the 1½ inch bore of the solenoid. In order to precool the magnet and sample to 77 K, the outer jacket of the dewar (B) was filled with liquid nitrogen. To further cool the sample during the liquid helium transfer, valve (b) was opened to let hydrogen exchange gas into the sample chamber. A pressure of about 0.7 Torr of H_2,

FIG. 3.2 He^3 cryostat and associated pumping systems. The labels are referred to in the text.

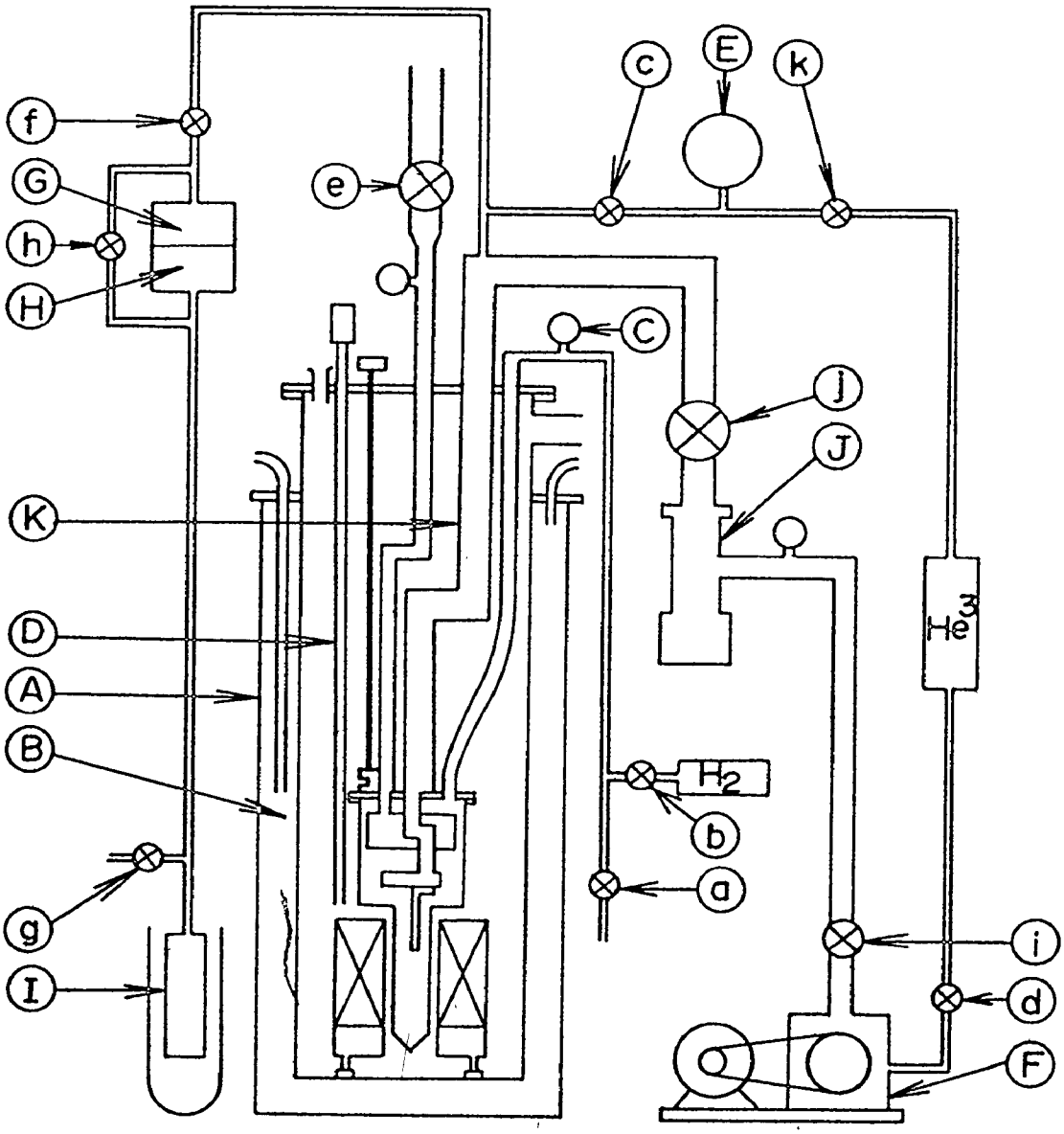
f
G
h
H
e
c
E
k
C
j
J
K
D
A
B
H_2
b
a
He^3
g
I
i
d
F

read on the thermocouple gauge (C), allowed the sample to cool from 77 K to 4.2 K. At this point, the exchange gas solidified on the walls of the sample can, thus returning the sample to thermal isolation.

The liquid level was monitored by means of a continuous liquid level gauge (D). When the liquid level had risen above the sample chamber, the needle valve (RR) was opened, allowing liquid helium to fill the He^4 pot (QQ). He^3 gas was admitted to the He^3 pot (CC) by opening valve (c). The gas was contained in the He^3 reservoir between valves (c) and (d). This had previously been filled with 99.5% pure He^3 gas to a pressure of 800 Torr, read on the pressure gauge (E). When the dewar was filled to capacity (about 7 litres), the needle valve was closed. By slowly opening valve (e), the liquid He^4 vapour pressure was reduced by a large Edwards mechanical pump to the ultimate pressure of 0.2 Torr. At this temperature of about 1.1 K, the He^3 gas condensed and ran into the He^3 pot. The sealed-shaft Welch rotary pump (F) was turned on, and the exhaust valve (d) was opened.

When as much He^3 as possible had condensed, valve (f) was opened to admit He^3 gas to a Datametrics Barocel capacitance manometer. The cell was divided into two chambers (G) and (H) by a flexible diaphragm. The difference in pressure between the two chambers was measured by the difference between the capacitances on either side of the diaphragm[70]. In order to measure

the absolute pressure, (H) was maintained at a very low reference vacuum by means of a charcoal trap (I) which was periodically evacuated through valve (g), and immersed in liquid nitrogen. The manometer was zeroed by closing valve (f) and opening the bypass valve (h) to connect the two chambers. With this arrangement, it was possible to measure pressures very accurately between 10 and 10^{-4} Torr.

To reduce the sample temperature below 1.1 K, valve (c) was closed, and valve (i) opened. Then, by slowly opening the large baffle valve (j), the He^3 vapour pressure was reduced by the forepump (F). This pump could produce a vapour pressure of about 3×10^{-2} Torr which corresponds to a temperature of about 0.4 K. To reach lower temperatures, it was necessary to use the diffusion pump (J).

This cryostat was designed to reach temperatures as low as 0.2 K. An important factor[71] in achieving this was the large 1 7/8 inch diameter He^3 pumping line (K), which allowed the liquid He^3 to be pumped to very low pressures. The ultimate temperature of this system will be discussed in section B of this chapter.

The circuitry used for the thermal conductivity measurements is shown in Fig. 3.3. Current for the upper and lower carbon thermometers, R_o and R_1 respectively, was supplied by the variable voltage V_t. The large 1 MΩ resistor in series with each thermometer ensured that the thermometer current would be independent of changes in the thermometer resistances. V_t

consisted of five standard 1.018 v batteries and five precision resistors. By adding various combinations of these, the thermometer current i_o could be varied in steps from 5.0 to 0.1 μa. As the temperature of the sample was lowered, it was necessary to use progressively smaller currents to avoid self-heating of the thermometers. The currents through the two thermometers were made equal by adjusting R_i. The polarity reversing switch was used to make sure no thermoelectric voltages were present before measurements were taken.

The temperature gradient along the sample was monitored by measuring the difference in the potentials across the two thermometers, $\Delta V = i_o(R_o - R_1)$, with a Hewlett-Packard differential voltmeter. This contained a known voltage supply which was adjusted to match the unknown voltage. Potentials could be measured to an accuracy of ±0.2 μv. The absolute temperature of the sample was monitored by using a second differential voltmeter to measure the potential across the upper thermometer, $V_o = i_o R_o$.

The differential voltmeter supplied an output voltage which was proportional to the difference between the known and measured voltages. This was fed to a controller which supplied current to the post heater R_p whenever V_o tried to rise above the value set on the voltmeter. This raised the temperature of the sample, thus lowering R_o to the preset value. The controller

FIG. 3.3 Schematic diagram of the thermal conductivity measuring circuits. The labels are defined in the text.

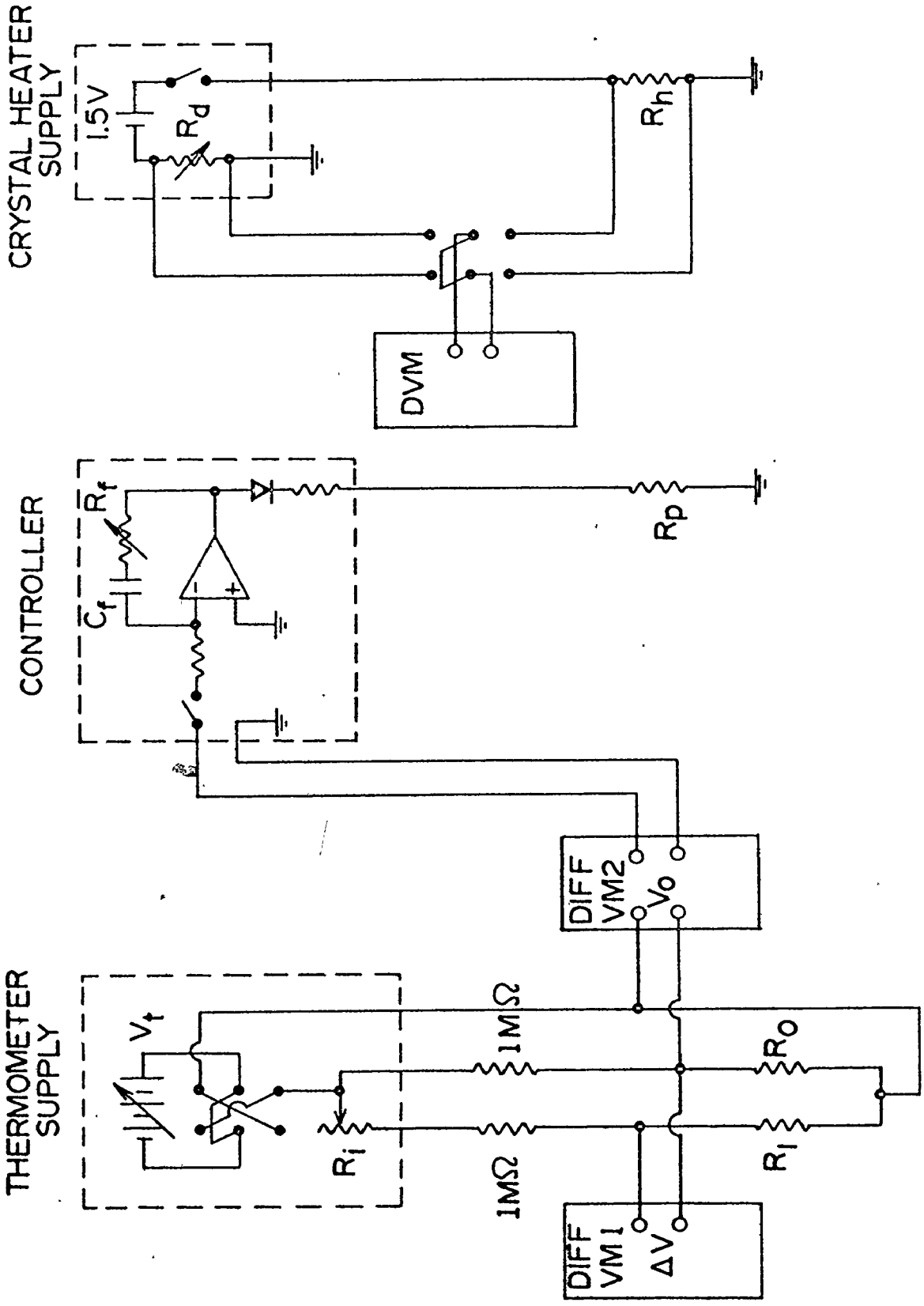
CRYSTAL HEATER SUPPLY
1.5V
R_d
R_h
DVM
CONTROLLER
R_f
C_f
R_p
DIFF VM2
V_o
THERMOMETER SUPPLY
V_t
R_i
1MΩ
R_o
R_1
1MΩ
DIFF VM1
ΔV_o

consisted of an operational amplifier with a feedback loop that provided an output voltage proportional to the input voltage plus the time integral of the input. By varying R_f and selecting different values of C_f, the gain and time constant of the controller could be adjusted to give the fastest possible damping of temperature variations at each temperature.

Current was supplied to the crystal heater R_h by a 1.5 v battery in series with a precision decade resistor R_d. The power delivered to the heater, $P = i_h V_h$ was monitored by using a digital voltmeter to measure the voltages V_h across the heater and $V_d = i_h R_d$ across the decade resistor.

The superconducting solenoid was energized by a 50 amp magnet power supply. Since the magnet showed no hysteresis, the field H could be calculated by measuring the magnet current, and using the known magnet constant, 60/44.1 kOe/amp.

The He^3 cryostat shown in Fig. 3.2 was inconvenient for measurements above 1.1 K. When as much He^3 as possible had been condensed in the He^3 pot, valve (k) was closed. Then, leaving the baffle valve (j) closed, the He^4 pumping rate was reduced by turning back valve (e). The temperature was monitored by noting the He^3 vapour pressure on meter (E). Using this method, measurements could be taken up to about 1.25 K. Above this temperature, there was no liquid He^3 left in the pot, and the He^3 gas did not provide an adequate thermal link between the He^4 pot and the sample.

Rather than installing a mechanical heat switch, a separate He^4 cryostat was used for measurements between 1.1 and 4.2 K. The He^4 cryostat was similar to the He^3 cryostat shown in Figs. 3.1 and 3.2, with the exception, of course, that it contained no He^3 pot or pumping system. The cryostat was used with the same magnet and dewar, and the measuring circuits were identical to those shown in Fig. 3.3. Temperature stability at these higher temperatures was achieved by using a Cartesian manostat in the He^4 pumping line to control the He^4 vapour pressure, and a 1 KΩ post heater. The temperature was measured using a 10^3 to 10^{-2} Torr Barocel manometer to monitor the He^4 vapour pressure. It was found that the two cryostats gave identical results, within the bounds of experimental error, in the overlapping temperature range.

B. Thermal Conductivity Data Analysis

In order to calculate the thermal conductivity from the experimental measurements, it was necessary to calibrate the carbon resistor thermometers. For the He^3 cryostat, the resistance of the upper thermometer R_o was measured as a function of temperature, which was calculated from the He^3 vapour pressure[72]. At the lowest temperatures however, the pressure measured by the manometer, which was at room temperature, was greater than the pressure in the cold He^3 pot because of thermomolecular effects[73,74]. Therefore, the temperature was also monitored

by measuring the susceptibility of cerium magnesium nitrate (CMN), which obeys a Curie law, $\chi = C/T$, down to very low temperatures[75]. A CMN salt pill, and the carbon thermometer were thermally attached to the post of the He^3 cryostat. The susceptibility was measured by a conventional technique[76]. A primary and secondary coil were wound on a form which fitted over the tail of the sample can, thus enclosing the salt pill. The susceptibility was then proportional to the mutual inductance between the coils, which was measured with a Cryotonics electronic bridge.

The results of a typical calibration run are shown in Fig. 3.4. Because of the large 1 7/8 inch diameter tube from the He^3 pot up to room temperature, thermomolecular effects did not become important until below 0.4 K. Even below this temperature, when the vapour pressure was corrected for the thermomolecular effect of a tube of this size, using the data of Freddi and Modena[74], 1/T varied linearly as the susceptibility down to the lowest temperature. Therefore, by using the published thermomolecular corrections, it was possible to use the He^3 vapour pressure as a primary thermometer over the entire range of the cryostat. The lowest temperature reached in these calibration runs was somewhat below 0.25 K.

Speer carbon resistors are very convenient low temperature thermometers[77]. The temperature characteristics of the resistors used in these experiments are shown in Fig. 3.5(a) for

FIG. 3.4 Susceptibility of CMN versus reciprocal temperature calculated from the He^3 vapour pressure. The solid circles have been corrected for thermomolecular effects, while the open circles are uncorrected.

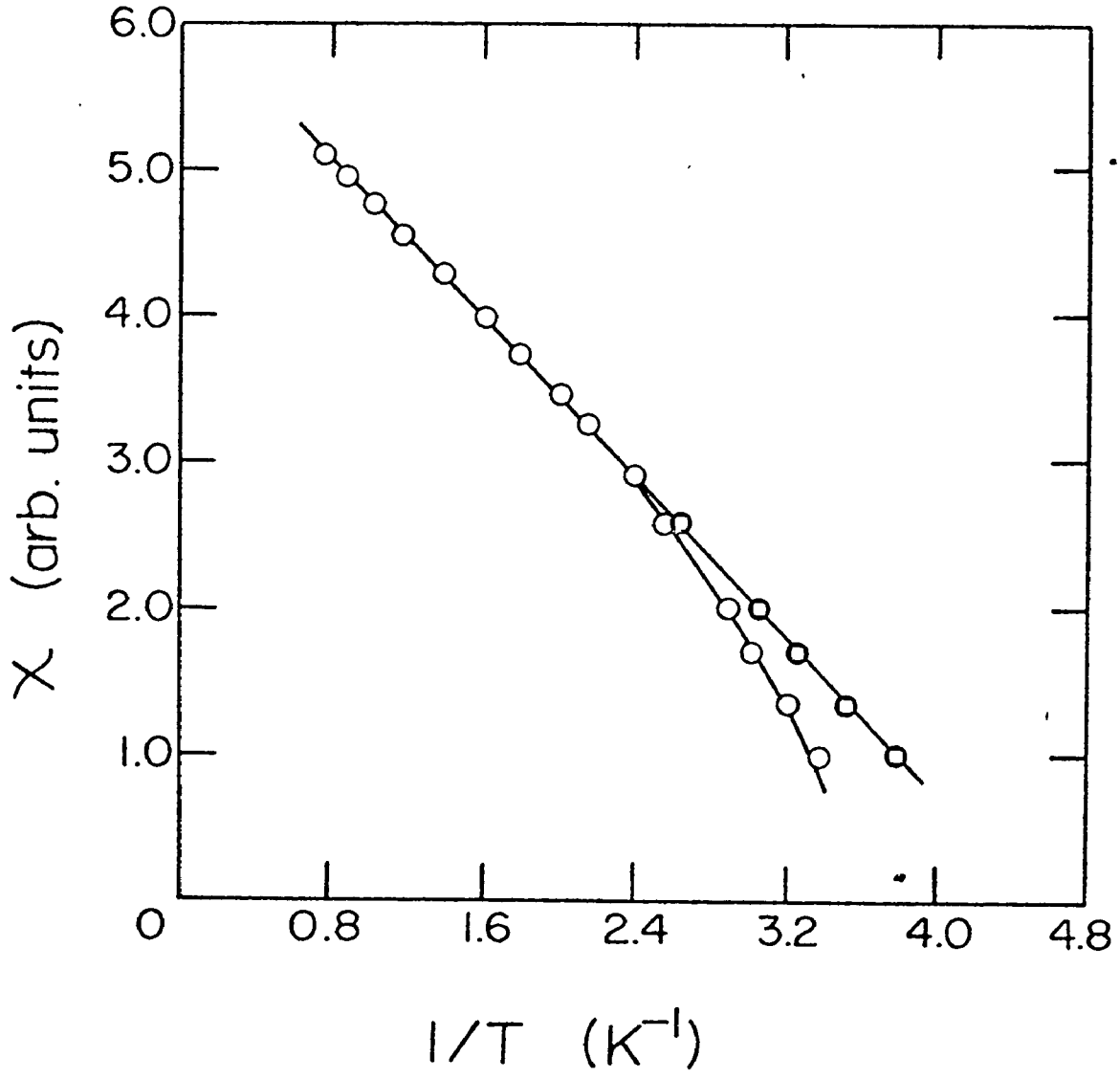
6.0
5.0
4.0
3.0
2.0
1.0
0
χ (arb. units)
0.8
1.6
2.4
3.2
4.0
4.8
1/T (K⁻¹)

the He^3 temperature range. Since R_o varies almost linearly with 1/T, this curve could be fitted by an equation of the form[78],

$$1/T = A + BR + CR^{1/2} \qquad (3.1)$$

with agreement between fitted and measured values of temperature to better than 1%. This is better agreement than that provided by most other interpolation formulae[78]. Moreover, the simple analytical form of (3.1) is very convenient for thermal conductivity calculations.

For the He^4 cryostat, the resistors were calibrated using the He^4 vapour pressure to measure the temperature[79]. The temperature characteristics for this range are shown in Fig. 3.5(b). Again, the curve could be fitted by the form of equation (3.1) with agreement to better than 1%. The same resistors were used in both cryostats. The curves do not match up exactly because of different lead resistances in the two systems. The best fit parameters for equation (3.1) are shown in Table 3.1 for the He^3 and He^4 temperature ranges.

The thermal conductivity was measured by a standard steady-state method. From equation (2.11), if the temperature gradient is uniform, and applied along a symmetry direction of the crystal, the thermal conductivity K is defined by the relation,

$$\frac{P}{A} = -K \frac{\delta T}{\ell} \qquad (3.2)$$

FIG. 3.5 Reciprocal temperature versus carbon thermometer resistance (a) over the He^3 temperature range, and (b) over the He^4 temperature range.

(a)

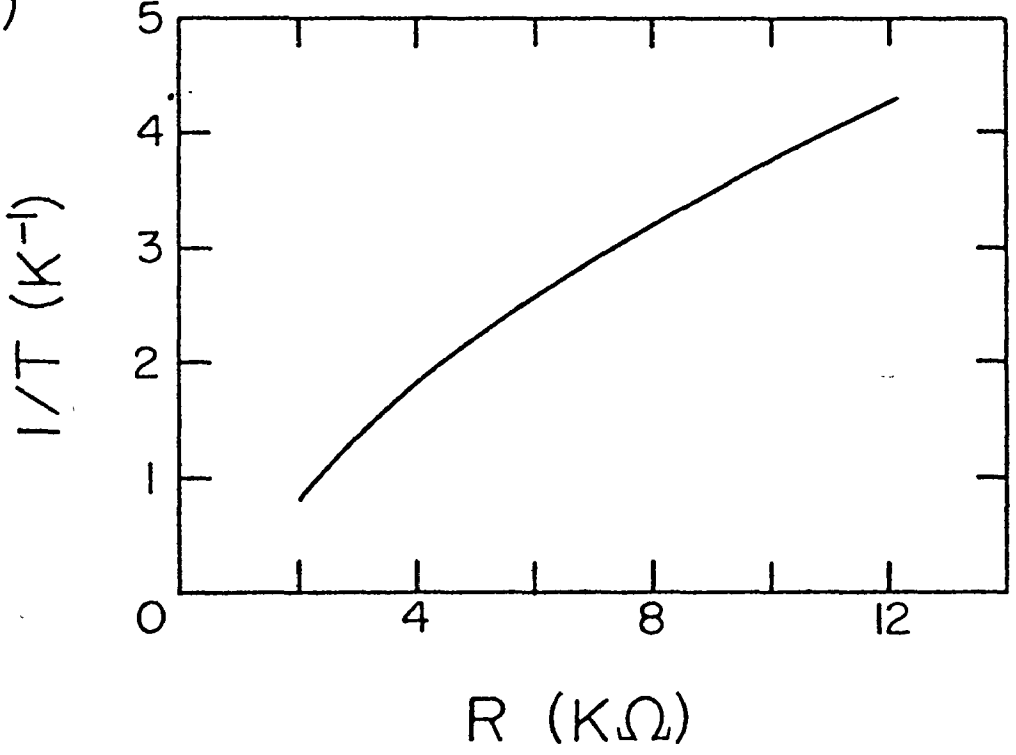

(b)

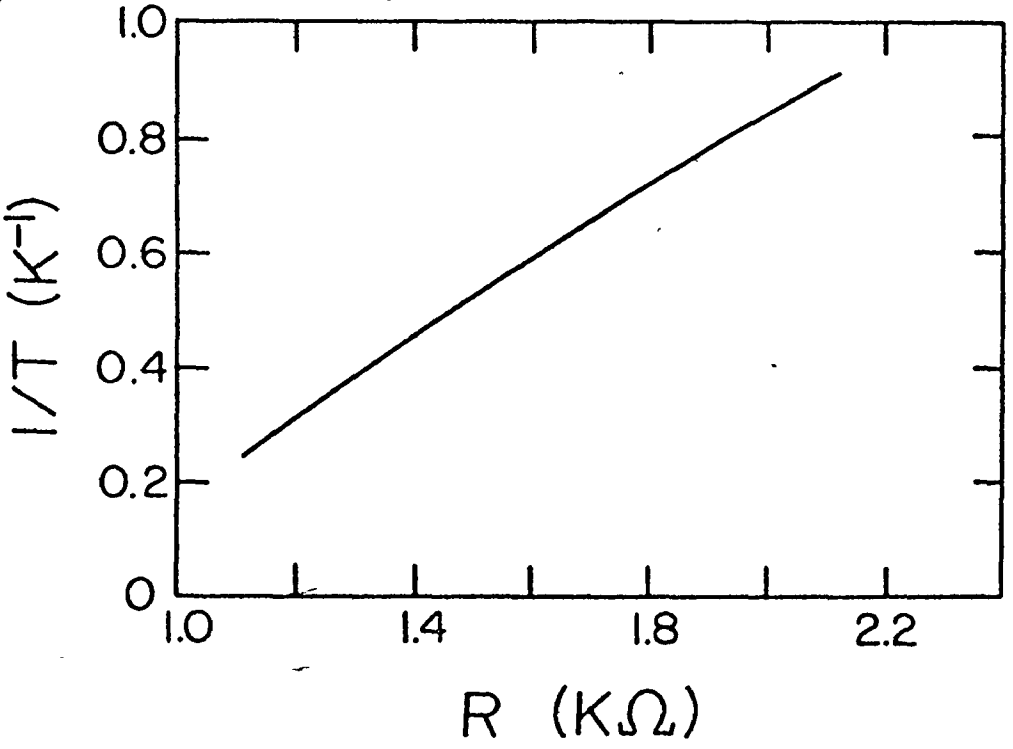

TABLE 3.1 Best fit parameters for the carbon thermometer calibration.

Temperature Range (K)	A (K^{-1})	B (K^{-1} $K\Omega^{-1}$)	C (K^{-1} $K\Omega^{-1/2}$)
0.25 - 1.25	-1.72693	-0.02850	1.82729
1.1 - 4.2	-1.15239	-0.22889	1.08796

where P is the power supplied to one end of the sample of cross-sectional area A, and δT is the temperature difference between two points along the sample, a distance ℓ apart.

The temperature difference δT is related to the difference in the resistances of the two thermometers δR by

$$\delta T = \left.\frac{\partial T}{\partial R}\right|_{T_o} \delta R \qquad (3.3)$$

where T_o is the average temperature of the sample. Since $\delta T << T_o$, then T_o is approximately the controlled temperature of the upper carbon resistor R_o. From equation (3.1),

$$\left.\frac{\partial T}{\partial R}\right|_{T_o} = -T_o^{\,2}\left(B + \frac{C}{2R_o^{\,1/2}}\right). \qquad (3.4)$$

The temperature characteristics of the carbon thermometers change somewhat on cycling between room temperature and liquid helium temperatures. It was found that, to a good approximation, only the parameter A in (3.1) changed with cycling, so the curves in Fig. 3.5 were only translated up or down. This can be neglected because (3.4) can be expressed as

$$\left.\frac{\partial T}{\partial R}\right|_{T_o} = -\,T_o^{\,2}\left.\frac{\partial (1/T)}{\partial R}\right|_{R_o} \qquad (3.5)$$

where T_o can be measured directly by the vapour pressure, and the second factor is just the slope of the curves in Fig. 3.5 which does not change with cycling. Therefore, the thermometers did not have to be calibrated before each run.

Of course, the two carbon resistors would not have exactly the same resistance, even when they were at the same temperature, so δR is actually

$$\delta R = \Delta R_Q - \Delta R_I \tag{3.6}$$

where ΔR_I is the isothermal difference in resistances, ΔR_Q is the difference in the presence of a heat flux Q, and

$$\Delta R = R_o - R_1. \tag{3.7}$$

In practice, it was convenient to choose a well matched pair of resistors so that ΔR_I was small.

Since all the power delivered to the crystal heater must go into the sample,

$$P = i_h V_h \tag{3.8}$$

where i_h is the heater current and V_h is the heater voltage. Combining the above equations, the thermal conductivity can be expressed as

$$K = \frac{\ell}{A} i_h V_h \frac{1}{T_o^2} \left(B + \frac{C}{2R_o^{1/2}}\right)^{-1} \frac{1}{\Delta R_Q - \Delta R_I} . \tag{3.9}$$

The thermal conductivity was measured as a function of temperature by the following procedure. The cross-sectional area A, and the thermometer separation ℓ were noted before the experiment. For the cylindrical sample TC3, A was 0.575 cm^2 and a typical thermometer separation was 3.0 cm. The cryostat was

pumped down to its lowest temperature, then allowed to warm slowly. When each desired temperature was reached, the corresponding resistance $R_o = V_o/i_o$ was noted. The controller was set to keep T_o constant, and the isothermal resistance difference $\Delta R_I = \Delta V_I/i_o$ was measured. Then, enough power was supplied to the crystal heater (typically a few mwatts) to create a $\delta T \approx 1\% \ T_o$, and the pumping speed was adjusted to compensate for the extra heat load. The new resistance difference $\Delta R_Q = \Delta V_Q/i_o$ was noted along with the heater voltage V_h and current $i_h = V_d/R_d$. With these measurements, the conductivity could be calculated from equation (3.9). The accuracy of the absolute value of the conductivity was limited, mainly by the measurement of the thermometer separation, to about ±5%, although relative changes in the conductivity with temperature would have a somewhat higher precision.

When the conductivity was measured as a function of magnetic field, keeping the temperature constant, the important quantity was the fractional change in conductivity,

$$\frac{\Delta K(H)}{K(O)} = \frac{K(H)-K(O)}{K(O)} = \frac{K(H)}{K(O)} - 1. \qquad (3.10)$$

From equation (3.2), the conductivity at a field H is

$$K(H) = - \frac{\ell}{A} \frac{P(H)}{\delta T(H)} \qquad (3.11)$$

where δT will change with field if the conductivity changes, and

P will be altered if the crystal heater resistance changes because of magnetoresistance effects. Therefore, using (3.11) and (3.3),

$$\frac{\Delta K(H)}{K(O)} = \frac{P(H)}{P(O)} \frac{\delta T(O)}{\delta T(H)} - 1 = \frac{P(H)}{P(O)} \frac{\Delta R_Q(O) - \Delta R_I(O)}{\Delta R_Q(H) - \Delta R_I(H)} - 1 \qquad (3.12)$$

where ΔR_I may change with field if the magnetoresistances of the two carbon resistors are not the same.

In practice, the controller was set to maintain a constant temperature T_o, and a reasonable resistance difference $\delta R = \Delta R_Q - \Delta R_I$ was established at zero field. Then, the field was increased, and $\Delta R_Q(H)$, $i_h(H)$, and $V_h(H)$ were measured, usually at 5 kOe intervals up to 60 kOe and back to zero to check for reproducibility. Then, the crystal heat was turned off, and the field was swept up again to measure $\Delta R_I(H)$. With these measurements, $\Delta K(H)/K(O)$ could be calcualted from equation (3.12). Usually, $P(H)$ and $\Delta R_I(H)$ did not change very much with field. Neglecting these changes in (3.12) would have produced an error in $\Delta K(H)/K(O)$ of only about 2%.

If the magnetoresistance of the carbon thermometer is large, then controlling at a constant resistance R_o will not maintain a constant temperature T_o as the field is changed. For the He^3 cryostat, this effect was found to be negligible, since the thermometers were held out of the strong magnetic field. For the He^4 cryostat however, where the thermometers were closer to the field, this was not the case. Therefore, when using this cryostat, a preliminary field sweep was performed to measure

the resistances $R_o(H)$ corresponding to a particular T_o at each field point.

The measurements of $\Delta K(H)/K(O)$ were observed to be reproducible to about ±2%. This is probably due to long term drifts in the measuring currents.

C. Heat Pulse Sample Preparation

The heat pulse samples used in these experiments were supplied by Optovac Inc. All the samples came from a single boule of MnF_2 which was of the same grade as the thermal conductivity sample. The samples were in the form of oriented cubes, 9 mm on a side. The orientations were checked with back reflection Laue photographs, and the cubes were cut with a diamond saw to form samples with various thicknesses along several crystallographic directions. The samples used to obtain the results which will be presented in Chapter IV are listed in Table 3.2.

For each sample, the faces perpendicular to the heat pulse direction were polished parallel and flat to a 1 micron finish. The sample was mounted in a holder and polished manually on 220, 320, 400, and 600 grade emery paper, then on a polishing wheel with 6 micron, and finally 1 micron diamond paste. The sample was then carefully cleaned and mounted in the evaporator for the application of the thin film heater and bolometer to the polished faces .

TABLE 3.2 Heat pulse samples.

Sample	Heat Pulse Direction	Heat Pulse Path Length (mm)	Cross-section Sides	Cross-section Dimensions (mm)
HP2	[001]	2.72	(110) , (1$\bar{1}$0)	9×9
HP3	[110]	3.61	(001) , (1$\bar{1}$0)	9×9
HP5	[110]	1.32	(001) , (1$\bar{1}$0)	9×9

The evaporator used is shown in Fig. 3.6. The apparatus was contained in a cylindrical glass jar (A) sealed by rubber O-rings (B) between the stainless steel top plate (C) and bottom plate (D). (The letters in parentheses refer to the labels in Figs. 3.6 and 3.7). The plates were fitted with vacuum tight feed-throughs to accomodate the evaporation apparatus. The sample was mounted in a sample holder (E) next to a Sloan quartz crystal thickness monitor (F), which measured the thickness of the evaporated film directly in Angstroms. A thin mask could be placed between the sample and the source by means of the rotating mask holder (G), which could accommodate three masks simultaneously. The material to be evaporated was placed in a tungsten boat (H) between two copper electrodes (I). The evaporator could accommodate three sources at the same time.

A typical series of evaporations proceeded as follows. The sample was placed in a 1 cm × 1 cm hole (AA) in a nylon disc (BB) in the sample holder (CC). The sample was supported by three small indium faced copper legs (DD). The mask holder (EE) was rotated so that the contact pad mask was below the sample. The evaporator was sealed and evacuated using a mechanical forepump. Then, the butterfly valve (J) was opened to connect the chamber to the large diffusion pump (K).

When the pressure in the chamber fell below about 2×10^{-6} Torr, as measured by an ionization gauge, a small amount of copper in one of the tungsten boats was heated until it began to evaporate. The shutter (L) was opened, and copper evaporated

FIG. 3.6 Thin film evaporator. The labels are referred to in the text.

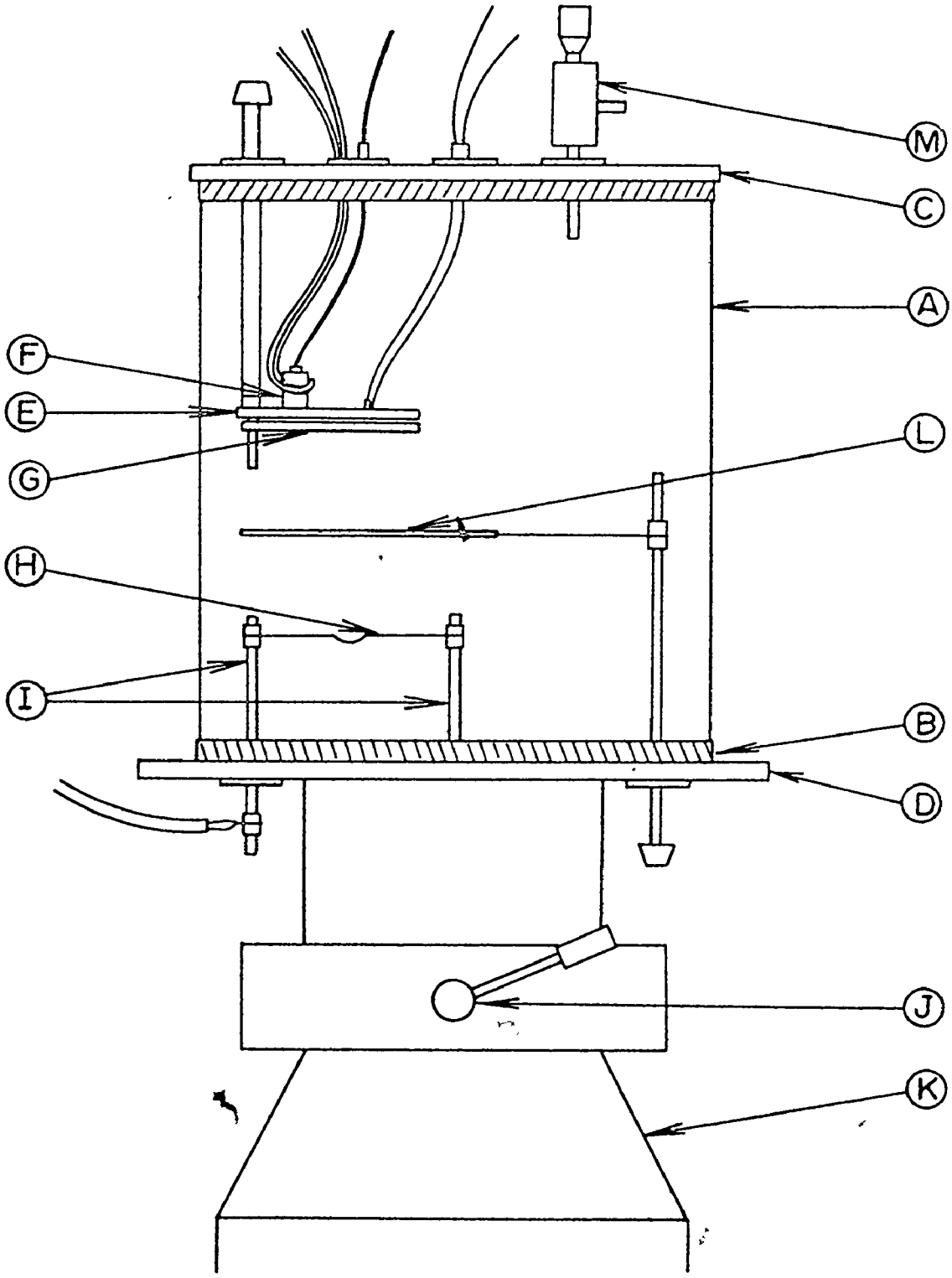
M
C
A
F
E
G
L
H
I
B
D
J
K

onto the sample until the contact pads were about 1200 Å thick, as measured by the thickness monitor (FF). The evaporation was then halted, and the evaporator opened. The contact pads (a) were in the form of 3 mm wide strips along two sides of the sample face, as shown in Fig. 3.7(b).

The sample was removed from the sample holder, rotated by 180°, and replaced, such that each pad made contact with one of the legs (DD) which were connected to electrical leads (GG) leading out of the evaporator. By connecting these to a 0.01 ma constant current source, and measuring the voltage across them with a digital voltmeter, it was possible to monitor the resistance of the heater or bolometer as it was being deposited between the contact pads.

The mask holder was rotated so that the heater mask (HH) was below the sample. After the chamber had again been evacuated, the constantan heater was evaporated onto the sample until it reached a resistance of about 65 Ω. At liquid helium temperatures, this produced a resistance of about 50 Ω which was the correct termination for the pulse generator used to supply voltage pulses to the heater. The heater (b) consisted of a thin strip, 3 mm long by 0.5 mm wide. Typically, it was about 500 Å thick. Without opening the chamber, the mask holder was rotated back to the contact pad mask, and another 1200 Å of copper was deposited to ensure good contact with the heater.

The chamber was then opened, and the sample turned over. Contact pads and the bolometer were evaporated onto the opposite

FIG. 3.7(a) Top view of the sample holder and rotating mask holder. The labels are referred to in the text.

FIG. 3.7(b) Finished heat pulse sample with evaporated thin films.

(a)

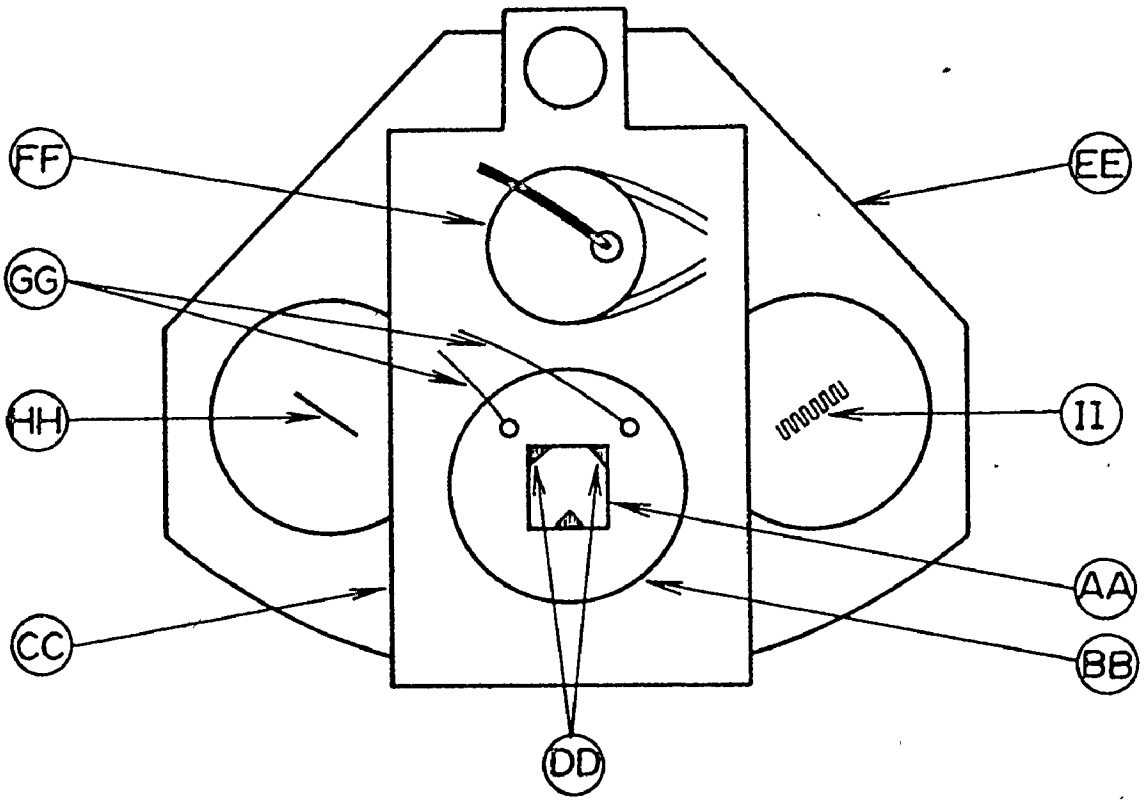

(b)

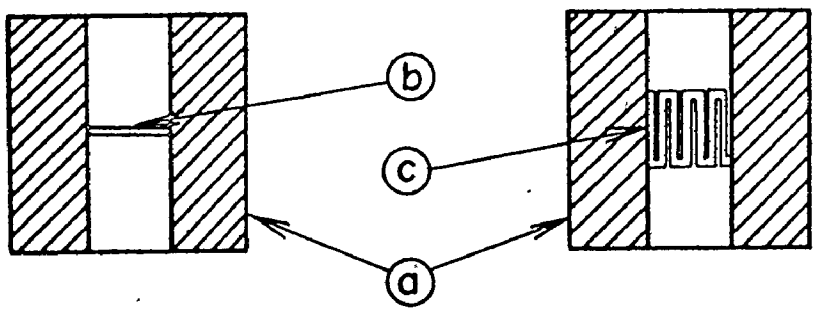

face in much the same fashion. The material used for the superconducting bolometer was granular aluminum, produced by evaporating aluminum in an oxygen atmosphere. Prior to the aluminum evaporation, the precision valve (M) was connected to an oxygen tank and opened until the pressure in the chamber rose to about 3×10^{-4} Torr. Granular aluminum has several advantages as a bolometer material[80,81]. With this oxygen pressure, the superconducting transition temperature was raised to about 2.0 K which was within the range of the heat pulse cryostat. Moreover, its superconducting transition was broadened so that it was possible to maintain the bolometer at its transition temperature with a simple temperature stabilization system.

A room temperature resistance of about 150 Ω was required for the bolometer so that when it was maintained near the lower end of its superconducting transition, it provided the 50 Ω termination required by the bolometer circuit. To produce this high resistance, and still have a fairly thick film, the bolometer length was increased by making it in the form of a convoluted strip. The finished bolometer (c) covered an area 3mm × 3 mm, and was typically about 750 Å thick. The bolometer mask (II) was produced by a photo-etching process. The finished heat pulse sample was removed from the evaporator and kept in a a desicator prior to its use in a heat pulse experiment.

D. Heat Pulse Apparatus and Measurements

The heat pulse sample (A) was clamped by means of a phosphor bronze spring (B) to an indium faced copper block (C).

(The letters in parentheses refer to the labels in Fig. 3.8.) The block was attached to a copper platform (D) which was suspended from the top flange of the sample chamber (E) by thick copper posts (F). Electrical contact was made to the two copper pads on each face of the sample by means of small drops of indium solder (G). Each pair of indium contacts was attached to a piece of printed circuit board (H), which was held against the sample by a coil spring (I) around a nylon bolt (J).

Electrical leads for the heater and bolometer consisted of thin 1/16 inch diameter coaxial cables (K). This method of achieving contact allowed the cables to extend right up to the indium contacts. It is important to keep the unshielded leads as short as possible because stray capacitance and inductance between the leads causes coupling between the heater and the bolometer circuits. When a short voltage pulse is applied to the heater, this direct pickup causes "ringing" in the bolometer circuit. The coupling must be minimized to ensure that this ringing will have died down before the actual heat pulse signal arrives at the bolometer.

The sample temperature was monitored by a germanium resistance thermometer (L) which was soldered to the copper platform. The thermometer had previously been calibrated against the vapour pressure of liquid He^4. The thermometer supply described in section A of this chapter was used to deliver current to the germanium resistor. Its voltage was measured by

FIG. 3.8 Heat pulse sample chamber. The labels are referred to in the text.

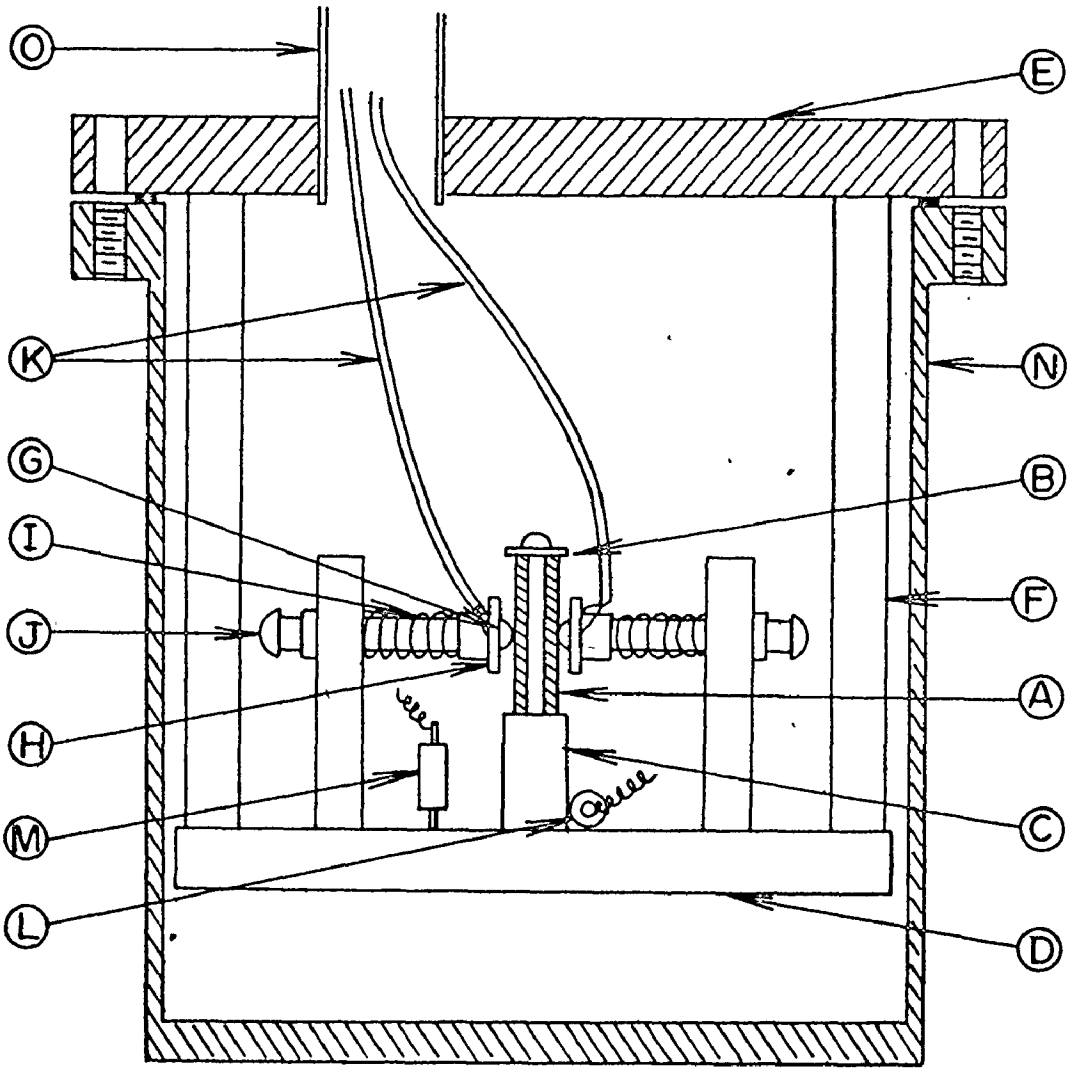
O
E
K
N
G
B
I
F
J
A
H
C
M
L
D

a differential voltmeter which also supplied the input to the temperature controller described in section A. The controller delivered power to a 1 KΩ heater (M) which damped any small variations in the sample temperature.

The sample chamber was enclosed by a brass can (N) which was attached to the top flange and sealed with an indium O-ring. The chamber was evacuated through the pumping line (O) which also carried the electrical leads. The cryostat was inserted into a simple glass dewar system, consisting of an inner helium dewar and an outer nitrogen dewar. After filling the dewar with liquid He^4 and allowing the sample to come to equilibrium at 4.2 K, the temperature was lowered to the superconducting transition of the bolometer by pumping on the liquid helium with a large Edwards mechanical pump. Extra temperature stability was achieved by using a Cartesian manostat in the pumping line to control the He^4 vapour pressure.

It is important to ensure that after the application of each heat pulse, the sample returns to the ambient temperature of the cryostat before the application of the next pulse, or the heater would quickly burn out. To provide extra cooling for the sample, the chamber was filled with about 2.0 Torr of helium exchange gas. Since thermal contact between the heater and the gas is poor compared to that between the heater and the sample, it is still a good approximation to assume that all the heat generated by the heater flows into the sample.

A constant current supply was used to deliver a dc current i_b = 0.3 ma to the bolometer. The voltage developed across the bolometer was measured by the Y axis of an X-Y recorder. The voltage across the germanium thermometer was connected to the X axis. Thus, as the temperature was slowly lowered, the resistance versus temperature characteristic of the bolometer was traced out. A bias temperature T_s was chosen at the lower end of the linear portion of the bolometer superconducting transition. The sample was stabilized at this temperature using the manostat and the temperature controller. A typical bolometer characteristic is shown in Fig. 3.9. The bolometers produced by the process described in section C of this chapter were fairly reproducible. It was always possible to choose a sample temperature T_s of approximately 2.0 K.

When a voltage pulse V_h was applied to the heater, the resulting heat pulse produced a temperature rise δT at the bolometer. This produced an ac signal in the bolometer circuit[49].

$$\delta V_b = i_b \delta R_b = i_b \frac{dR_b}{dT} \delta T \qquad (3.13)$$

which was proportional to the heat pulse signal if dR_b/dT was constant. It can be seen from Fig. 3.9 that the bolometer characteristic was fairly linear over a range for δT of about 0.1 K. It should be noted that this is not the same as the heat pulse temperature T_h, which describes the frequency distribution of the phonons in the heat pulse. Because of geometrical losses,

FIG. 3.9 Superconducting bolometer resistance versus temperature. The bias sample temperature is also shown.

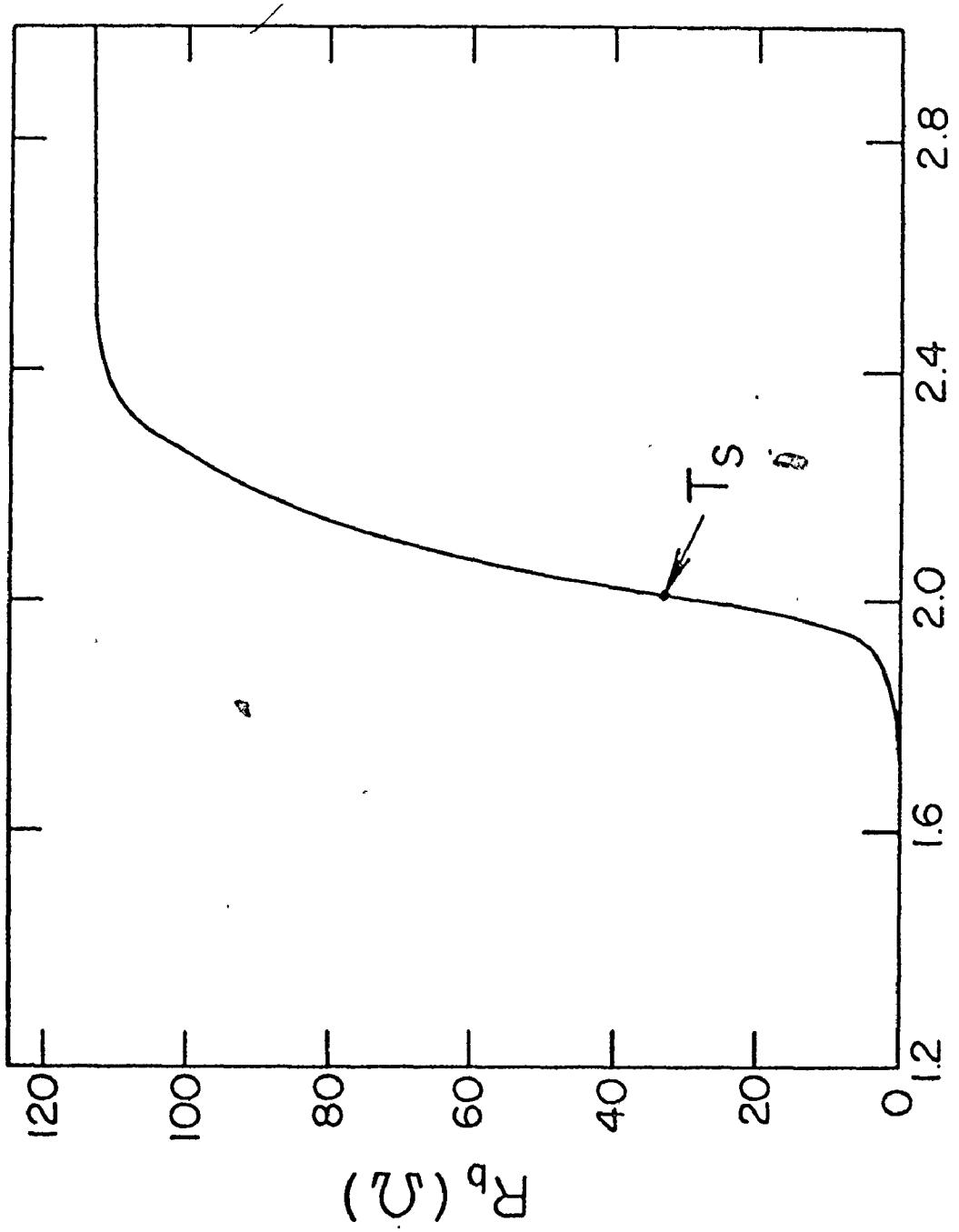
R_b (Ω)
120
100
80
60
40
20
0
1.2
1.6
2.0
2.4
2.8
T (K)
T_s

the actual temperature rise δT at the bolometer is quite small even for fairly high values of T_h [55].

A block diagram of the heat pulse circuits is shown in Fig. 3.10. An isolator was inserted into the bolometer circuit so that the current supply was connected through a large inductance. This prevented the ac signal from flowing back into the supply. The heat pulse signal was extracted through a large capacitance which removed any dc component.

The heat pulse waveform is repeated at the frequency with which pulses are delivered to the heater, typically about 500 cps. Since any noise in the signal varies randomly from cycle to cycle it can be averaged out using a boxcar integrator. This samples the input waveform during each cycle, using a variable width, variable delay gate. The signal passed by the gate is averaged by an integrator with an adjustable time constant. If the gate is narrow compared to the input waveform, the output will be the value of one point on the input signal, averaged over some large number of repetitions. If the gate is then slowly scanned across the input signal, the entire averaged waveform will be reproduced at the output.

The narrowest gate available on the PAR boxcar integrator used in these experiments was 10^{-6} sec, whereas it was necessary to resolve details of the heat pulse signal of the order of 10^{-8} sec. To compensate for this, a narrow gate generator and a pulse stretcher were incorporated into the circuit. The sequence of events was as follows. The pulse generator produced

FIG. 3.10 Block diagram of the heat pulse circuits.

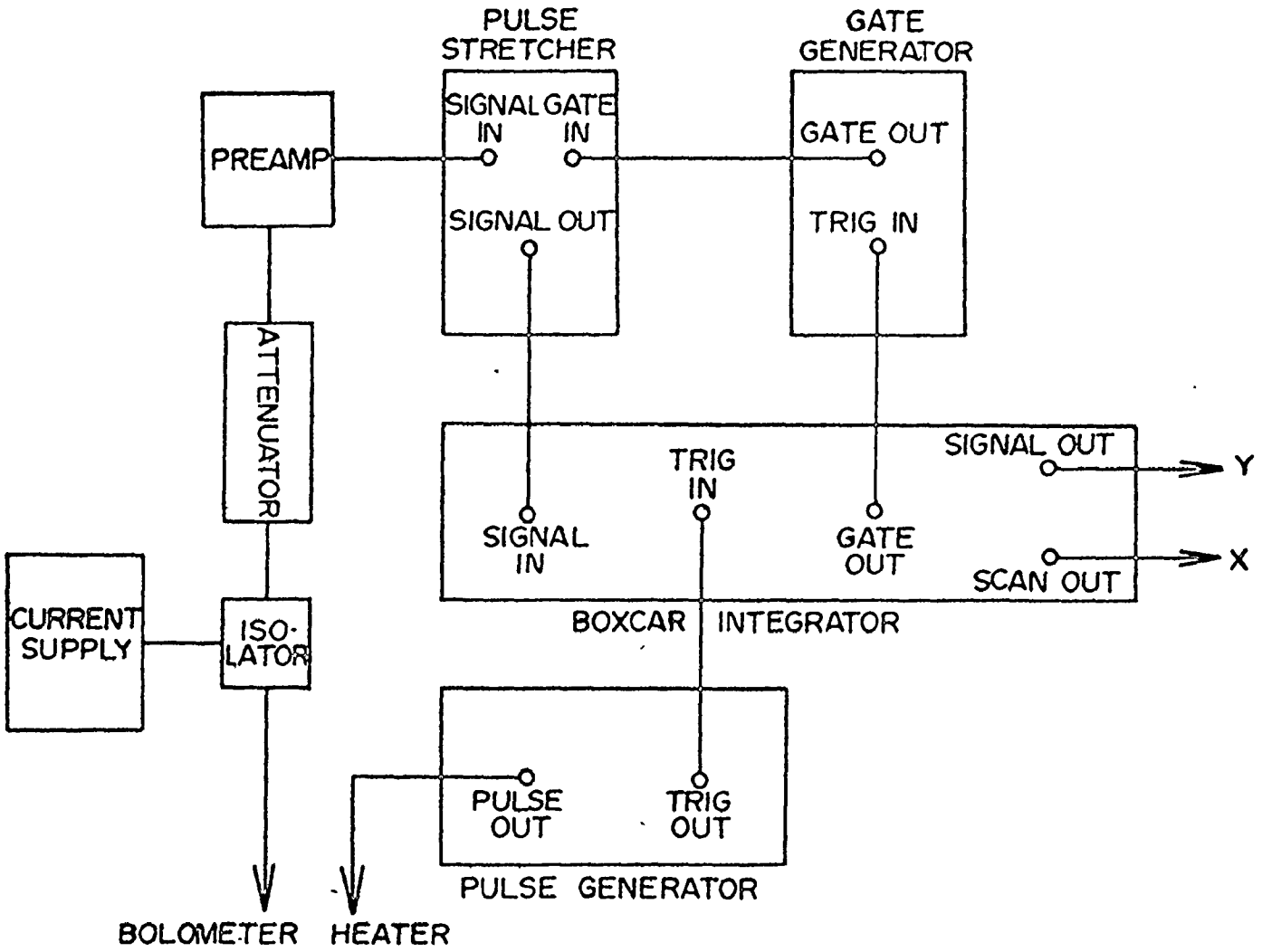
PULSE
STRETCHER
GATE
GENERATOR
SIGNAL
IN
GATE
IN
GATE OUT
PREAMP
SIGNAL OUT
TRIG IN
ATTENUATOR
SIGNAL OUT
Y
TRIG
IN
SIGNAL
IN
GATE
OUT
SCAN OUT
X
CURRENT
SUPPLY
ISO-
LATOR
BOXCAR INTEGRATOR
PULSE
OUT
TRIG
OUT
PULSE GENERATOR
BOLOMETER
HEATER

a trigger pulse which was fed to the boxcar integrator. After the adjustable delay set by the integrator, it produced a 10^{-6} sec gate pulse. The leading edge of this pulse acted as a trigger for the gate generator. This produced a narrow 2×10^{-8} sec gate pulse which was fed to the pulse stretcher.

Meanwhile, after a delay of about 10^{-6} sec, set by the pulse generator, a heater voltage pulse was produced with an adjustable amplitude V_h, and a width of about 6×10^{-8} sec. This created the heat pulse signal in the bolometer circuit which was amplified by a 40 db preamplifier and fed to the pulse stretcher. During the 2×10^{-8} sec narrow gate interval, the heat pulse signal was sampled by the pulse stretcher and stored on a capacitor which had a long discharge time of 10^{-5} sec. The stretched signal was then fed to the boxcar integrator where it could be sampled by the long 10^{-6} sec gate.

Finally, the output of the integrator was fed to the Y axis of an X-Y recorder, while the scan ramp which swept the gate across the input signal was fed to the X axis. Thus, the averaged heat pulse signal was traced out on the recorder. The signals were reproducible to about ±0.5%. This is limited mainly by small drifts in the bolometer bias temperature.

The heat pulse signals could be investigated for various pulse temperatures T_h by varying the amplitude of the heater voltage V_h. Using equation (2.56), the heat pulse temperature can be calculated from

$$T_h = \left(\frac{P_h}{\sigma A_h} + T_s^4\right)^{1/4} \qquad (3.14)$$

where T_s is the ambient sample temperature, P_h is the power delivered to the heater, A_h is the area of the heater, and σ is the Stefan-Boltzmann constant for phonon radiation. The heater power is

$$P_h = V_h^2/R_h \qquad (3.15)$$

where V_h is the heater voltage, and R_h is the heater resistance, typically about 50 Ω. For the heater described in section C of this chapter, $A_h = 0.015\ cm^2$. From equation (2.56), the Stefan-Boltzmann constant is

$$\sigma = \frac{\pi^2}{120}\frac{K_b^4}{\hbar^3}\left(\frac{1}{V_{hL}^2} + \frac{2}{V_{hT}^2}\right) \qquad (3.16)$$

For a constantan heater, the velocities of longitudinal and transverse phonons are[53] $v_{hL} = 5.24\times10^5$ cm/sec, and $v_{hT} = 2.64\times10^5$ cm/sec. Therefore, for constantan, $\sigma = 0.0824$ watts $cm^{-2}K^{-4}$.

In order to accurately compare the magnitudes of the signals for different values of V_h, the gains of all the elements in the circuit were left constant, and the signal was attenuated by a precision attenuator. In a typical experiment, heat pulse signals were recorded starting with the smallest V_h (usually about 1.0 v) which gave a measurable signal with no attenuation. V_h was then increased in steps until the signal was noticeably distorted due to the bolometer being driven above the linear range of its characteristic (usually above 10 v).

CHAPTER IV

EXPERIMENTAL RESULTS

A. Thermal Conductivity

The thermal conductivity with no applied magnetic field is shown in Fig. 4.1 for the cylindrical sample TC3. This shows a log-log plot of the conductivity against the sample temperature. A dashed line with a slope of 3 has been drawn in for reference. As pointed out in Chapter II, if scattering from the boundaries of the sample is the dominant phonon scattering process, the conductivity should exhibit a characteristic T^3 temperature dependence. It can be seen from the diagram that only at the lowest temperatures does the conductivity approach a T^3 dependence.

Below about 1.0 K, the slope of the conductivity curve is less than 3, while above 1.0 K it is greater than 3. This dip in the conductivity is characteristic of resonant scattering of the phonons by impurities[39,40]. The maximum in the dip occurs approximately at the temperature T at which the most important phonons for heat conduction have frequencies, $\omega = 3.8\ k_B T/\hbar$ equal to the resonant frequency, ω_o of the impurity. Therefore, if the dip at 1.0 is caused by a single resonance, its frequency is approximately given by $\hbar\omega_o/k_B = 3.8$ K. It is

FIG. 4.1 Temperature dependence of the thermal conductivity for sample TC3. Heat flow is along the [001] direction. The sample diameter is 0.856 cm. A dashed line with a slope of 3 is shown for reference.

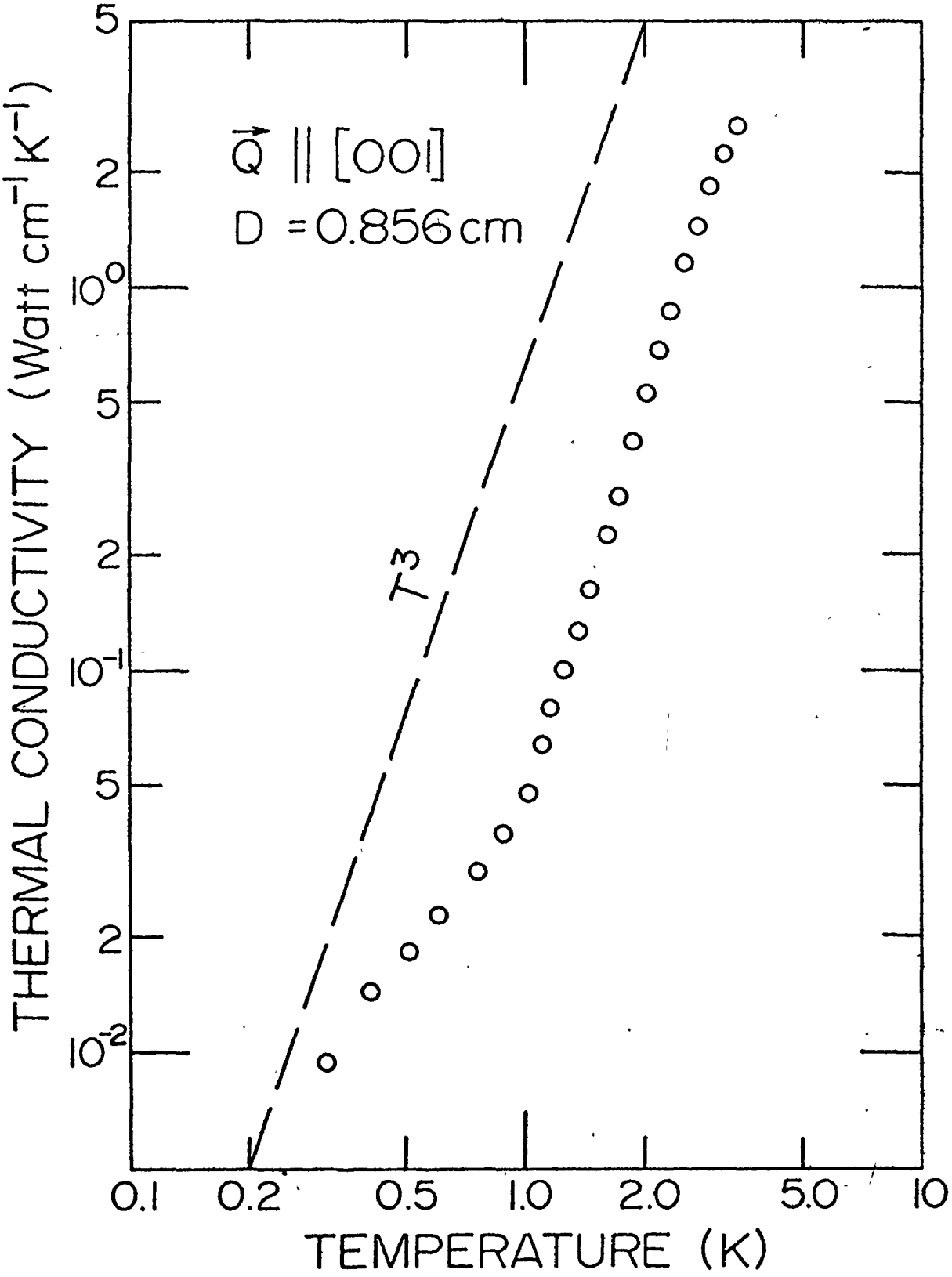
THERMAL CONDUCTIVITY (Watt cm⁻¹K⁻¹)
5
2
10⁰
5
2
10⁻¹
5
2
10⁻²
Q ⃗ || [001]
D = 0.856 cm
T³
0.1
0.2
0.5
1.0
2.0
5.0
10
TEMPERATURE (K)

possible that the dip is caused by more than one resonance. Since the phonon frequency distribution is very broad, several closely spaced resonances would not be resolved by thermal conductivity measurements.

It is clear that this dip is not caused by a resonant interaction of the phonons with the magnons. The point of intersection of the magnon and phonon dispersion curves must occur at an energy above the anisotropy gap in the magnon spectrum. For MnF_2, this is $\hbar\omega(0)/k_B$ = 12.5 K, so the magnon-phonon resonant interaction could produce a dip in the conductivity only at temperatures above $\hbar\omega(0)/3.8\ k_B$ = 3.3 K.

The gradual decrease in the slope of the conductivity curve above 2.0 K is probably due to the onset of point defect scattering. As indicated in Chapter II, if the measurements were extended to higher temperatures, the conductivity would eventually reach a peak, then begin to decrease, as phonon-phonon interactions become the dominant scattering mechanism. It is not yet possible to fit a theoretical expression to the conductivity results, because it is not known which phonon modes are being resonantly scattered. This information can be deduced from the heat pulse results.

B. Heat Pulses

Typical heat pulse signals are shown in Figs. 4.2-4.4 for the three heat pulse samples. The zero of the time scale

corresponds to the time of application of the voltage pulse to the heater. This is indicated by the onset of ringing in the bolometer circuit due to direct electrical pickup. The time scale is set by the boxcar integrator.

The first phonons to arrive at the bolometer are ballistic phonons which travel directly along the path length L between the heater and the bolometer. This is a symmetry direction of the crystal, so the group velocities of these phonons are equal to their phase velocities. Therefore, the arrival time of the leading edge of each heat pulse is given by

$$t_o = L/v_i \tag{4.1}$$

where v_i is the phase velocity of each phonon mode i. The phase velocities were calculated from equation (2.22) using measured values of the elastic constants for MnF_2 [33]. (See also section A of Chapter V.) The calculated arrival times are shown in Figs. 4.2-4.4. It can be seen that these are in good agreement with the experimental measurements.

In the [001] direction, the two transverse modes are degenerate. The phase velocities are given by

$$\rho v_L^2 = C_{33}$$

and

$$\rho v_T^2 = C_{44} \tag{4.2}$$

where ρ is the crystal density, and C is an elastic constant. From Fig. 4.2, it can be seen that the heat from the transverse phonons does not arrive as a ballistic pulse, but rather as a

FIG. 4.2 Heat pulses for sample HP2. Propagation is along the [001] direction with a path length of 2.72 mm. The heater power is 0.5 watts which corresponds to a pulse temperature of 4.5 K. Calculated pulse arrival times are also shown.

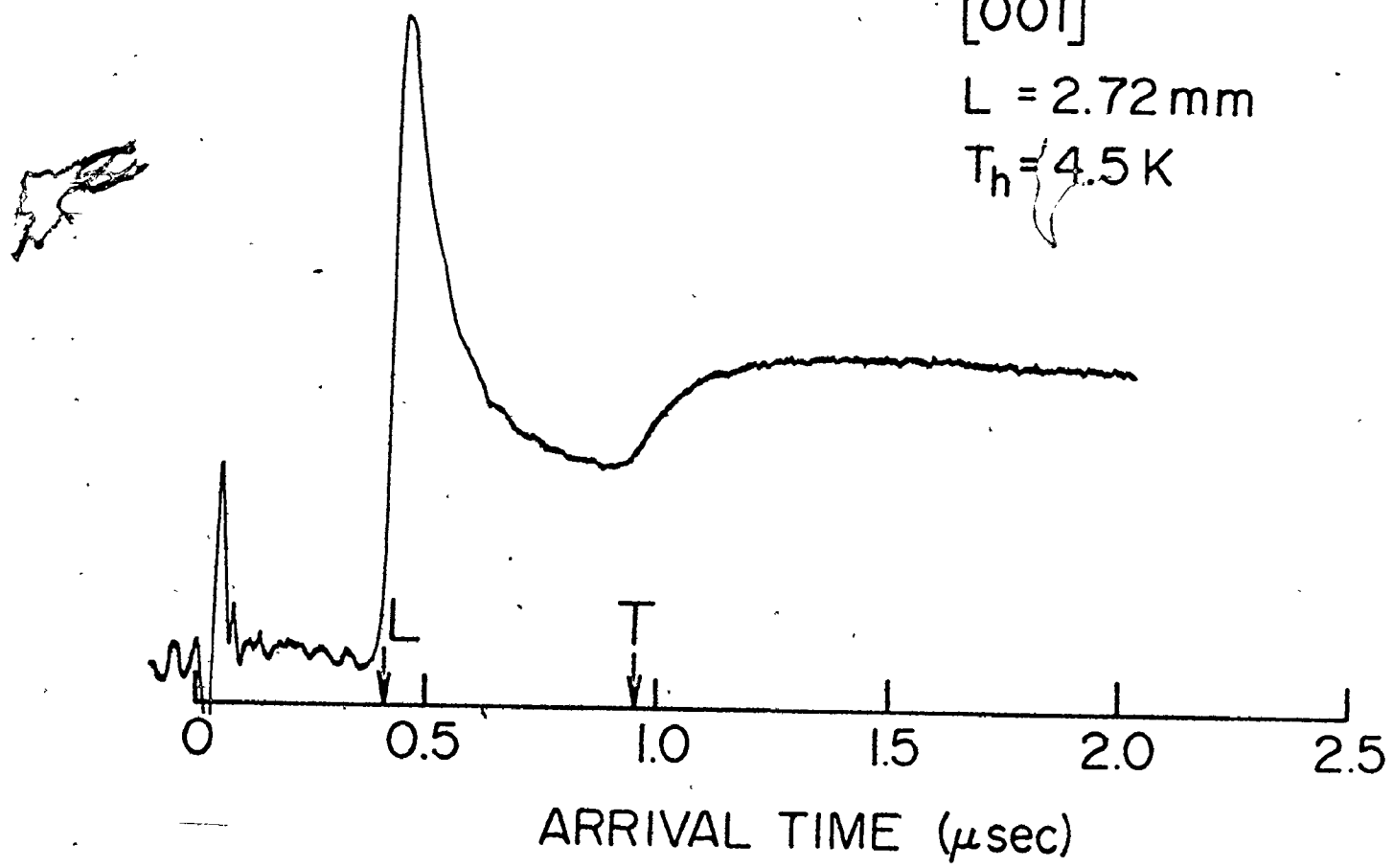
[001]
L = 2.72 mm
T_h = 4.5 K
L
T
0
0.5
1.0
1.5
2.0
2.5
ARRIVAL TIME (μsec)

FIG. 4.3 Heat pulses for sample HP3. Propagation is along the [110] direction with a path length of 3.61 mm. The heater power is 0.5 watts which corresponds to a pulse temperature of 4.5 K. Calculated pulse arrival times are also shown.

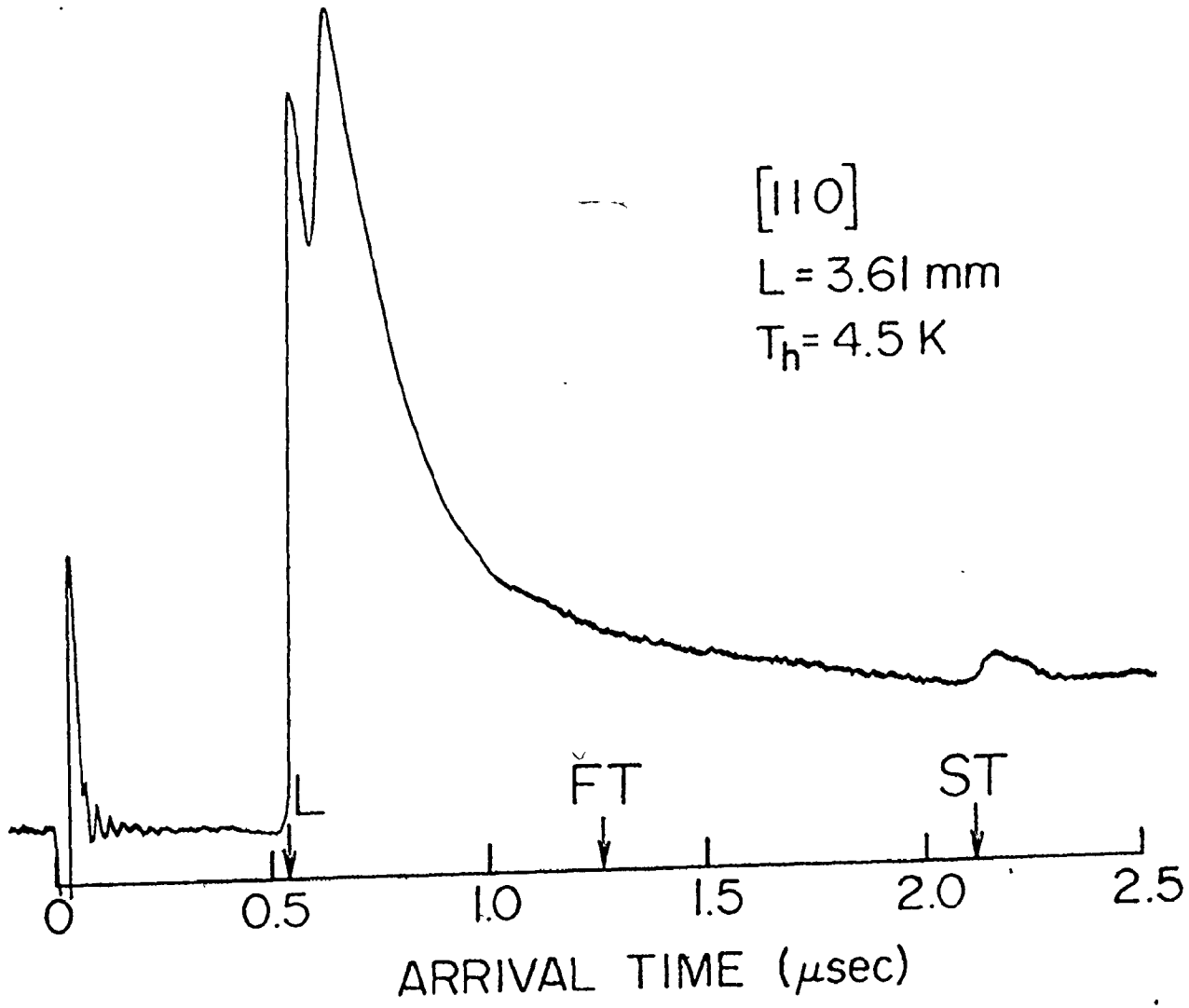
[110]
L = 3.61 mm
T_h = 4.5 K
L
FT
ST
0
0.5
1.0
1.5
2.0
2.5
ARRIVAL TIME (μsec)

FIG. 4.4 Heat pulses for sample HP5. Propagation is along the [110] direction with a path length of 1.32 mm. The heater power is 0.5 watts which corresponds to a pulse temperature of 4.5 K. Calculated pulse arrival times are also shown.

[110]

L = 1.32 mm

T_h = 4.5 K

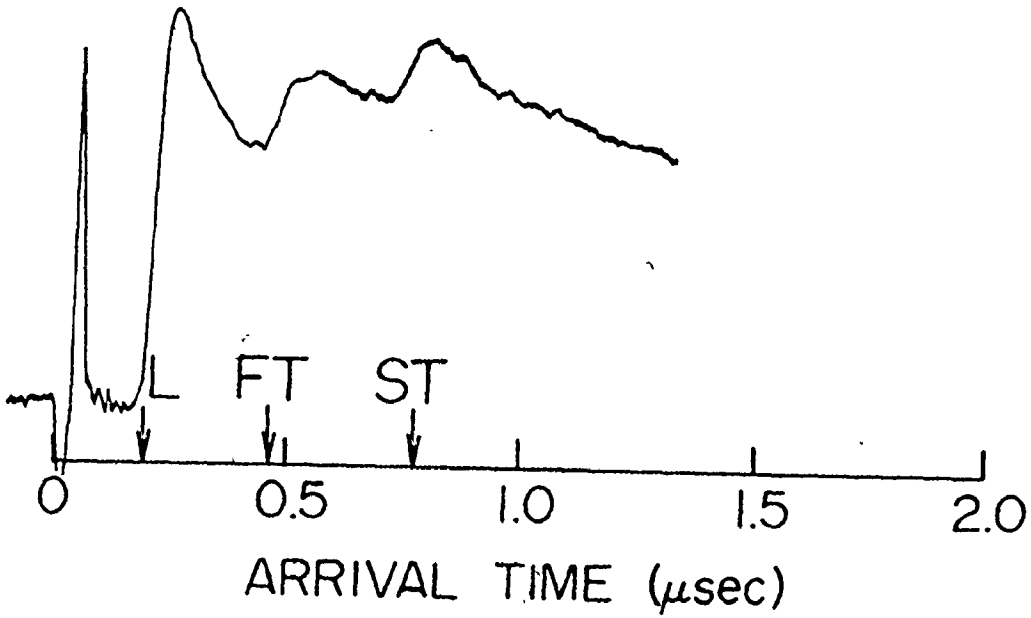

broad diffusive ramp. This indicates that these phonons have been strongly scattered.

In the [110] direction, there are three modes with phase velocities given by

$$\rho v_L^2 = \frac{1}{2}(C_{11} + C_{12} + 2C_{66})$$
$$\rho v_{FT}^2 = C_{44} \qquad (4.3)$$

and

$$\rho v_{ST}^2 = \frac{1}{2}(C_{11} - C_{12}) \ .$$

The presence of an extra heat pulse in Fig. 4.3, arriving just after the longitudinal pulse is a consequence of elastic anisotropy. Phonons emitted from the heater with phase velocities in some other direction have their group velocities along the heater-detector direction, and therefore, are detected by the bolometer. The nature of these phonons will be discussed in Chapter V.

From Fig. 4.3, it can be seen that for a fairly thick [110] sample, the heat pulse due to the fast transverse phonons is missing entirely. However, this pulse is present in a thinner sample, as shown by Fig. 4.4. Since its intensity relative to the other pulses decreases with increasing path length, it appears that this pulse has been attenuated by a factor $\exp(-t_o/\tau_i)$, where τ_i is the relaxation time for this mode.

In both the [001] and [110] directions, it is the phonons associated with the C_{44} elastic constant which are being scattered. In terms of group theory, these are phonons of E_g symmetry[82].

The heat pulse results suggest that perhaps it is the scattering of the E_g phonons that causes the resonance dip noted in the thermal conductivity.

This is consistent with measurements of the elastic constants of MnF_2 by Melcher[33], using ultrasonic velocity measurements. It was found that the C_{44} elastic constant decreased sharply at low temperatures. This decrease in the velocity of sound could be due to the dispersion produced by a resonant interaction of this mode with an impurity. Only the C_{44} constant showed this effect. In Chapter V, it will be shown that the resonant scattering in the thermal conductivity, the attenuation of the heat pulses, and the decrease in the C_{44} elastic constant can all be quantitatively accounted for by a resonant interaction of the E_g phonons with an impurity.

The heat pulse signals in Figs. 4.2-4.4 are all for a heater power of 0.5 watts which, from equation (3.14), corresponds to a characteristic temperature T_h for the heat pulse of 4.5 K. The power dependence of the heat pulse intensities is shown in Figs. 4.5-4.7. The intensity was calculated from the height of the pulse in the heat pulse signal, divided by the attenuation factor that was used in the bolometer circuit. For longitudinal pulses, the height was measured from the signal baseline. For transverse pulses, it was taken to be the height above the extrapolated diffusive tail from the previous pulse. Since the [001] transverse pulse did not show a true

ballistic peak, its height was arbitrarily measured at an arrival time of 1.2 μsec.

Figs. 4.5-4.7 show log-log plots of the heat pulse intensity I against the heater power P_h. The corresponding pulse temperatures T_h are shown on the upper scale. The data can be fit fairly well by a straight line with a slope of 1. Therefore, the intensity varies linearly with the heater power, as predicted by equation (2.57). At the highest heater powers, the intensities began to be attenuated because the bolometer was driven above the linear range of its characteristic. This limits the pulse temperature to a range of about 2.5 K to 6.0 K.

The scattered transverse pulses in Figs. 4.5 and 4.7 can also be fitted, within experimental error, by a linear dependence on P_h. Equation (2.64) predicts that these pulses should show a different dependence on T_h because of the frequency dependence of the relaxation time. However, from the thermal conductivity results in Fig. 4.1, it can be seen that above the resonance at 1.0 K, the effect of the resonant scattering does not change very much with temperature. Therefore, it is not surprising that the additional T_h dependence cannot be noticed over this short range of pulse temperatures. If a heat pulse cryostat were constructed which would allow measurements below 1.0 K, one would expect to see the scattered pulses grow in intensity relative to the ballistic pulses as T_h was lowered. Since the ratios of the pulse heights were the same for all heater powers,

FIG. 4.5 Dependence of the heat pulse intensity on heater power for sample HP2. The pulse temperatures are also shown. The straight lines through the experimental points have a slope of 1.

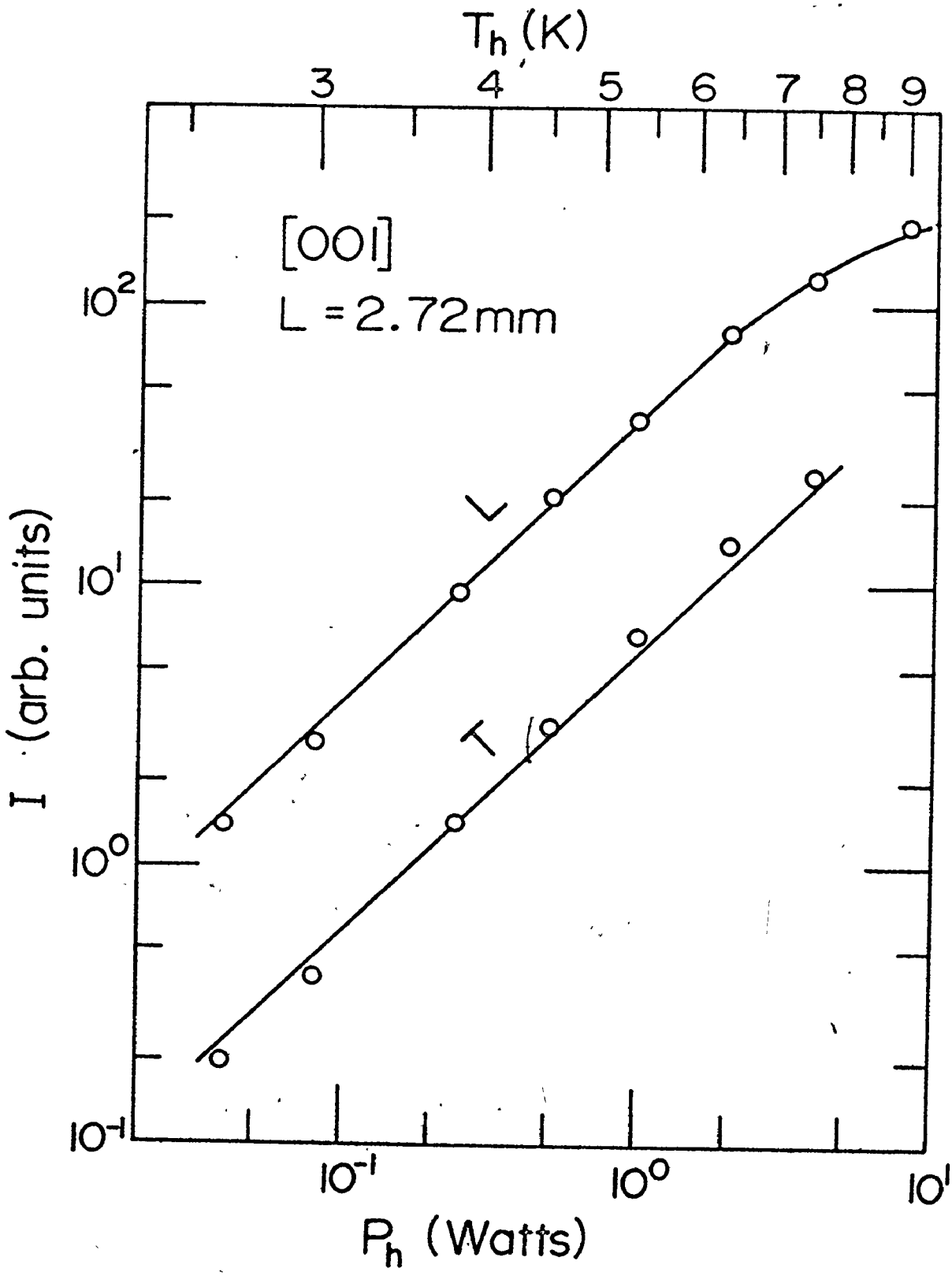
T_h (K)
3
4
5
6
7
8
9
[001]
L = 2.72mm
10^2
10^1
10^0
10^{-1}
I (arb. units)
L
T
10^{-1}
10^0
10^1
P_h (Watts)

FIG. 4.6 Dependence of the heat pulse intensity on heater power for sample HP3. The pulse temperatures are also shown. The straight lines through the experimental points have a slope of 1.

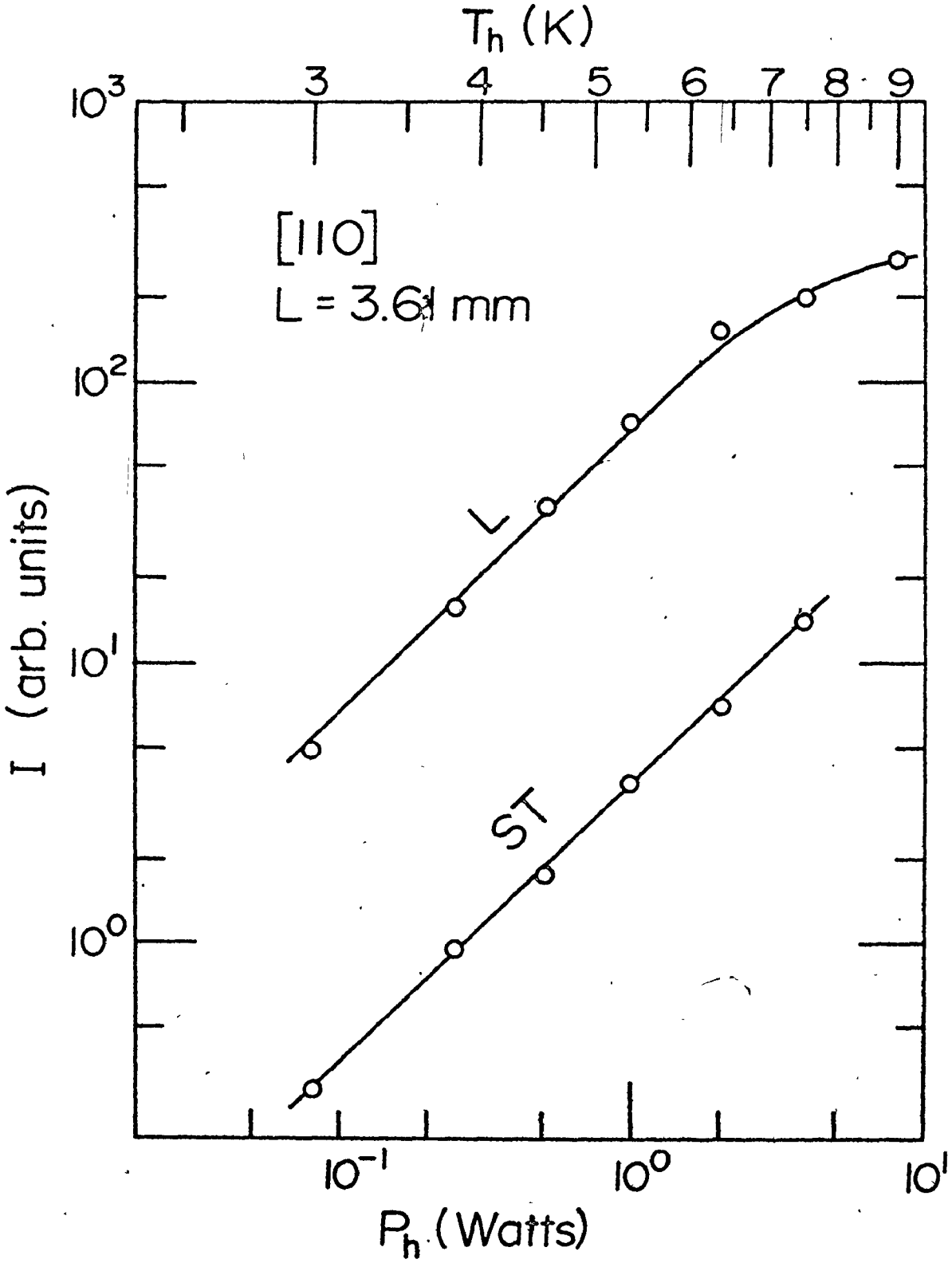
T_h (K)
3
4
5
6
7
8
9
10^3
10^2
10^1
10^0
[110]
L = 3.61 mm
L
ST
I (arb. units)
10^{-1}
10^0
10^1
P_h (Watts)

FIG. 4.7 Dependence of the heat pulse intensity on heater power for sample HP5. The pulse temperatures are also shown. The straight lines through the experimental points have a slope of 1.

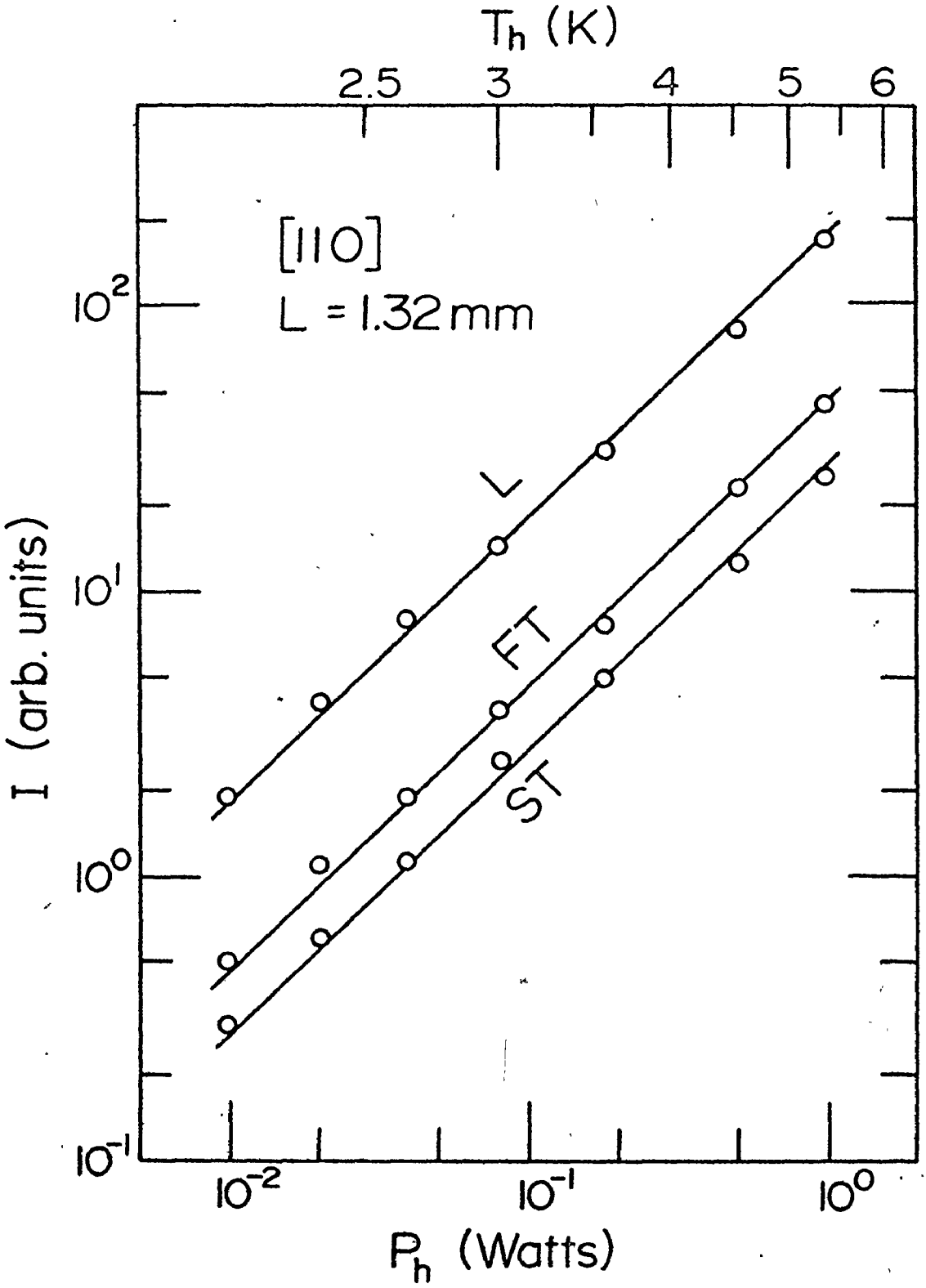
T_h (K)
2.5
3
4
5
6
[110]
L = 1.32 mm
10^2
10^1
10^0
10^{-1}
I (arb. units)
L
FT
ST
10^{-2}
10^{-1}
10^0
P_h (Watts)

the shapes of the heat pulse signals, for any value of T_h in the range that could be investigated, were similar to those shown for T_h = 4.5 K in Figs. 4.2-4.4.

C. Magnetic Field Effects

MnF_2 becomes antiferromagnetically ordered below its Néel temperature T_N = 67.34 K[83], with the spins of the Mn^{++} ions aligned parallel or antiparallel to the [001] easy axis of magnetization. When a magnetic field was applied parallel to the [001] direction, the conductivity did not change, within experimental error, in fields up to 60 kOe for any temperature in the range that was investigated. This is shown by Fig. 4.8 which shows the fractional change in conductivity as a function of magnetic field.

As indicated in Chapter II, when a magnetic field is applied parallel to the easy axis of a uniaxial antiferromagnet, the magnon dispersion curve splits into two branches, one being raised in energy, and the other lowered. The lower branch acquires a much larger thermal population, so the net magnon conductivity increases. If a significant fraction of the heat current were being carried by the magnons, this would produce an increase in the total conductivity with magnetic field. Therefore, the experimental results show no evidence for heat conduction by the magnons. In Chapter V, the expected magnon contribution to the total conductivity will be calculated,

FIG. 4.8 Magnetic field dependence of the thermal conductivity for fields along the [001] direction. The relative change in the conductivity from its zero field value is shown.

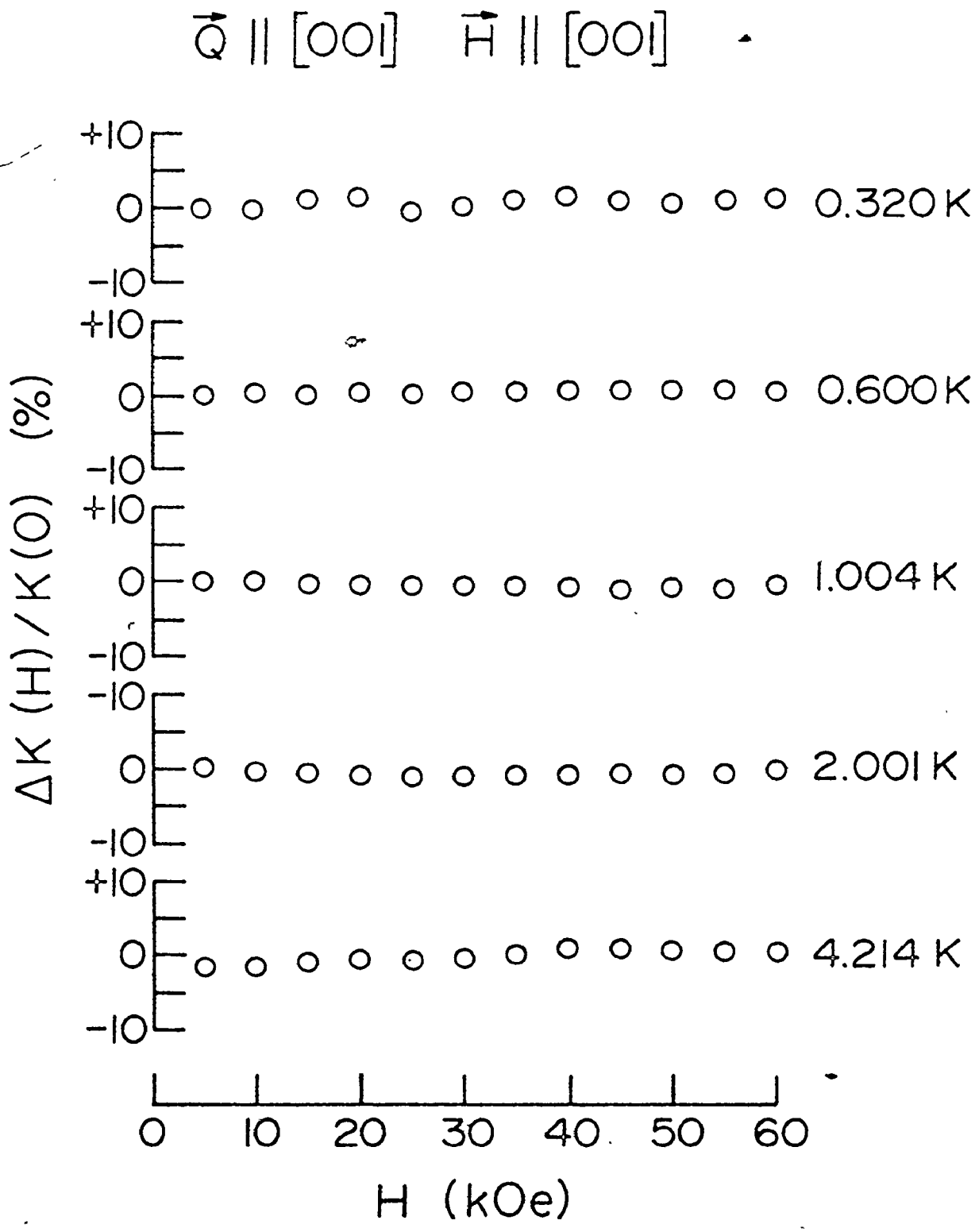
$\vec{Q} \parallel [001]$ $\vec{H} \parallel [001]$
+10
0
-10
0.320 K
0.600 K
1.004 K
2.001 K
4.214 K
ΔK (H) / K (0) (%)
0
10
20
30
40
50
60
H (kOe)

and possible reasons for the absence of this contribution will be discussed.

The results also show no variation in the conductivity that could be attributed to a resonant interaction of the phonons with the magnons. As the magnetic field is increased, the points of intersection of the magnon branches with the phonon dispersion curves move to different frequencies, causing a change in the phonon conductivity. Such effects have been noted in other magnetic materials[5,13,16,17]. The fact that there is no change for MnF_2 indicates that the resonant magnon-phonon interaction must be small.

In the course of the experiments, it was noticed that if the field was applied at an angle to the [001] direction, large changes in the conductivity resulted. This was achieved by mounting the sample at an angle to the copper post in the sample chamber. The maximum angle that could be accommodated by the tail of the sample can was about 25°. The change in conductivity for magnetic fields applied at this angle is shown in Fig. 4.9 for various temperatures. Within experimental error, these results depended only on the angle from the [001] axis, and not on the particular crystallographic direction along which the magnetic field was applied.

These results are not evidence for magnon conductivity. They can be accounted for using only the phonon contribution. The results shown in Fig. 4.9, plus those at intermediate

FIG. 4.9 Magnetic field dependence of the thermal conductivity for fields at 25° to the [001] direction. The relative change in the conductivity from its zero field value is shown.

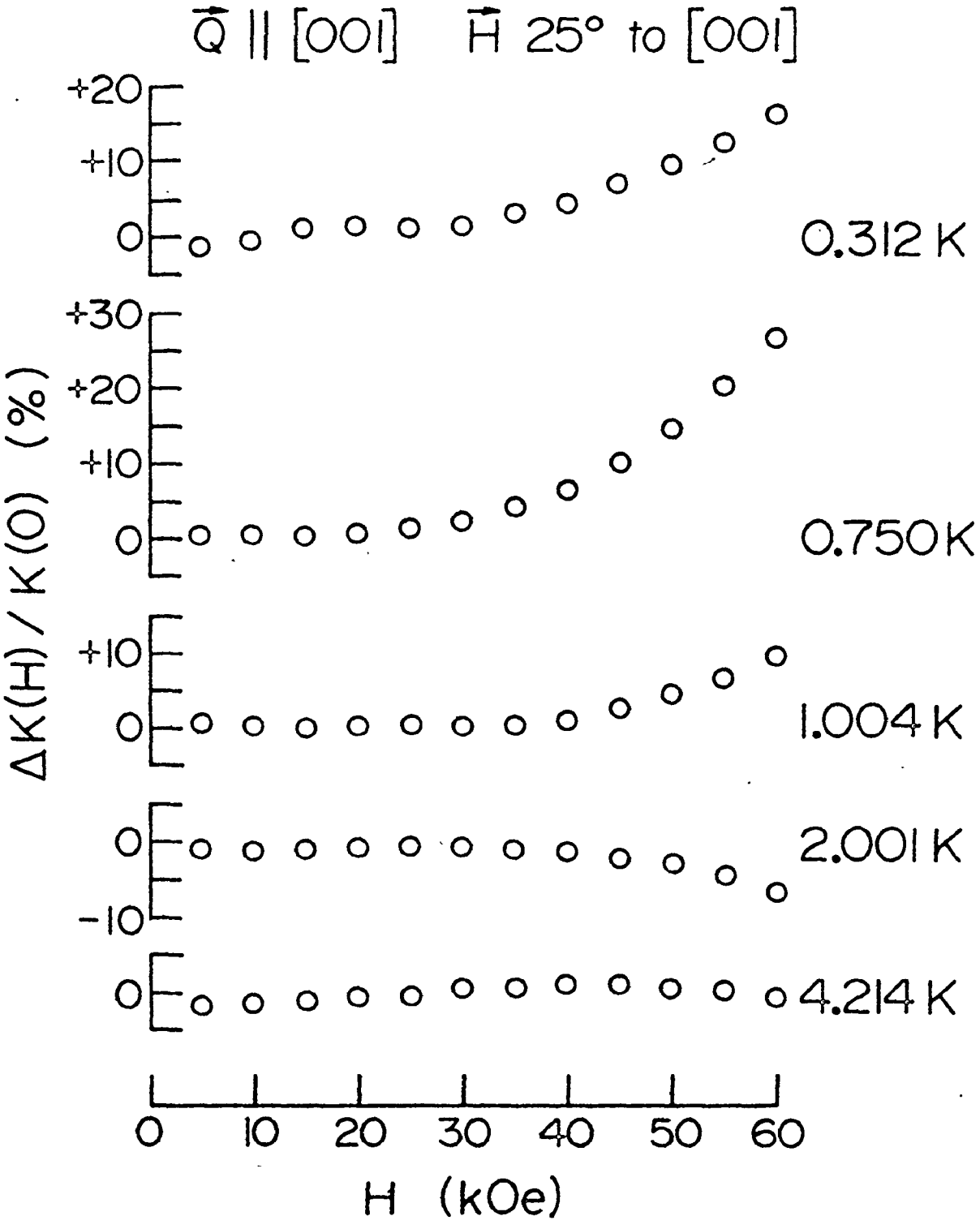
$\vec{Q}$ || [001] $\vec{H}$ 25° to [001]
+20
+10
0
0.312 K
+30
+20
+10
0
0.750 K
+10
0
1.004 K
0
-10
2.001 K
0
4.214 K
ΔK(H) / K(0) (%)
0
10
20
30
40
50
60
H (kOe)

FIG. 4.10 Relative change in the thermal conductivity at 60 kOe for a field at 25° to the [001] direction.

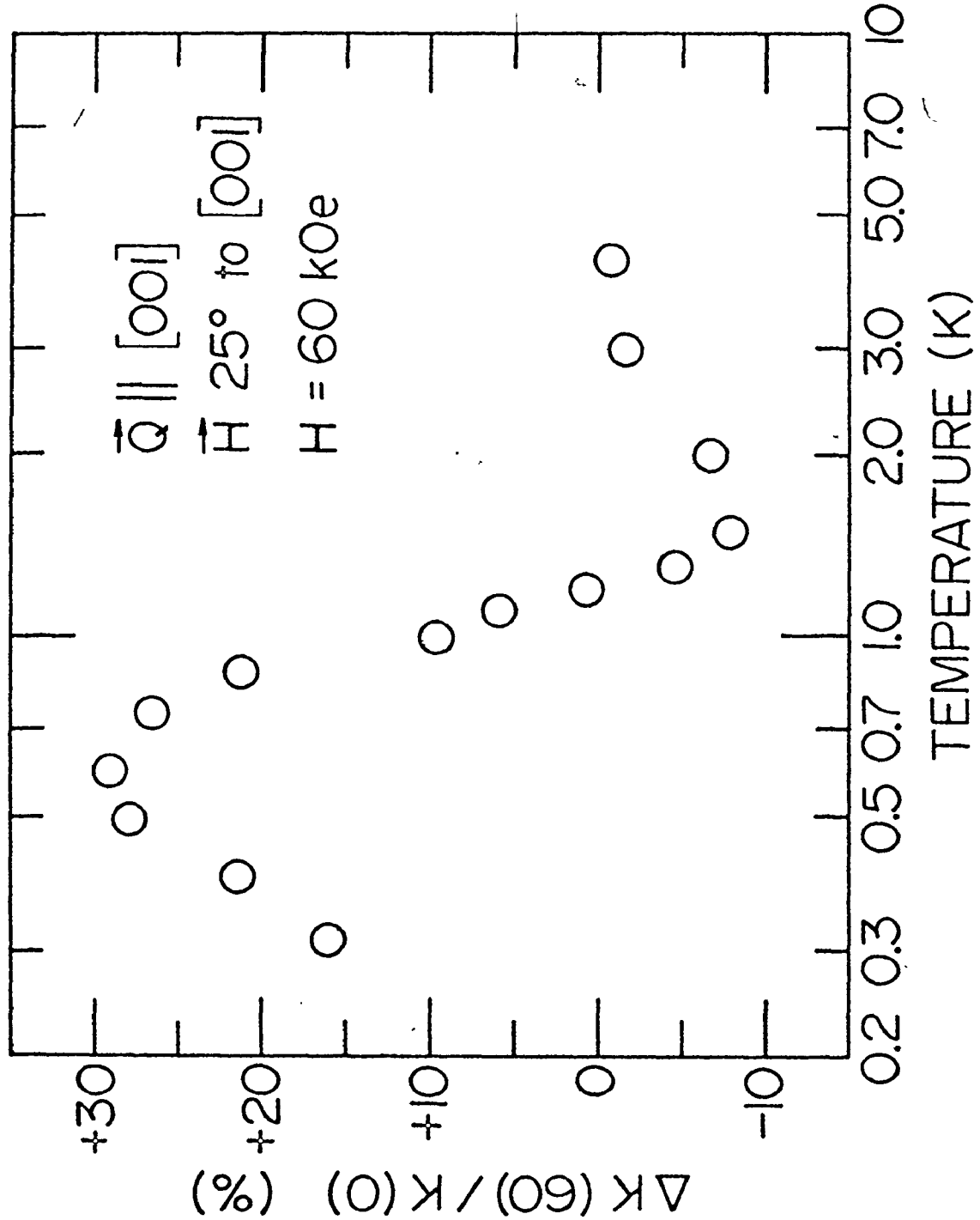
$\vec{Q} \parallel [001]$
$\vec{H}$ 25° to [001]
H = 60 kOe
+30
+20
+10
0
-10
$\Delta K\,(60)\,/\,K\,(0)$ (%)
0.2 0.3 0.5 0.7 1.0 2.0 3.0 5.0 7.0 10
TEMPERATURE (K)

temperatures are summarized in Fig. 4.10, which shows the relative change in conductivity at 60 kOe as a function of temperature. Below about 1.2 K, the conductivity increased with field, the maximum effect being at about 0.6 K, while above 1.2 K, the conductivity decreased. At any temperature, the shape of the field dependence was similar to those shown in Fig. 4.9.

These results are characteristic of a shift in the resonant frequency of the impurity[84]. With reference to Fig. 4.1, if the resonant frequency increases with magnetic field, the resonance dip, which was at 1.0 K with no applied field, will move to higher temperatures. Therefore, above 1.0 K this will produce a lower conductivity, while below 1.0 K it will cause a higher conductivity. In Chapter V, these results will be quantitatively explained in terms of theoretical expressions for the phonon thermal conductivity. Also, a possible mechanism for producing a shift in the resonant frequency with magnetic field will be discussed.

CHAPTER V

CALCULATIONS AND DISCUSSIONS

A. Phonon Velocities

As mentioned in Chapter II, in order to properly analyze the thermal conductivity[32] and heat pulse[51] results, it is necessary to be able to calculate the phase and group velocities of phonons travelling in any direction in the crystal. At low temperatures, this can be accomplished using the theory of elastic waves travelling in a continuous, but anisotropic medium. The phase velocity with which the wavefront travels through the medium is derived in Appendix A, following the notation of Farnell[35]. The group velocity, with which energy is transported by the wave, has been analyzed by Musgrave[85]. This method allows group velocities to be calculated algebraically for crystals of hexagonal[85] or cubic[86] symmetry. For other symmetries, the group velocity can be calculated numerically using an expression due to Fedorov[36], which is also outlined in Appendix A.

To find the phase and group velocities associated with a wave vector pointing in any direction, it is only necessary to know the elastic constants and the density of the medium. The six elastic constants of MnF_2 have been measured at 4.2 K by Melcher[33], and are listed at the bottom of Table 5.1. MnF_2

has a density of 3.925 g/cm^3 at room temperature[87] and, allowing for thermal expansion[88], of 3.93 g/cm^3 at 4.2 K.

Along symmetry directions of the crystal, the solutions to equation (2.22) for the phase velocities are particularly simple. Also, the group velocities are equal to the phase velocities for wave vectors along these directions. These velocities are listed in Table 5.1 for the three symmetry axes of MnF_2.

The phase and group velocity surfaces for the entire crystal were calculated numerically from equations (2.22) and (2.23), using a CDC 6400 computer. Cross sections through these surfaces are shown in Figs. 5.1-5.3 for the three mirror planes of MnF_2. For a phase velocity vector lying in such a plane, the group velocity vector associated with it also lies in the plane. The phase velocities are shown by the solid lines, and the group velocities by the dashed lines.

Fig. 5.1 shows a cross section of the velocity surfaces in the (001) plane. The most striking feature is the multivalued nature of one transverse group velocity surface. This results from the "cusps" that form around the relative maxima in the phase velocity surface in the <100> directions. In general, as many as three group velocities can exist in a given direction for each polarization[49]. Later in this chapter it will be shown that the phonons in these cusps are responsible for the extra pulse noted in the heat pulse results.

TABLE 5.1 Phonon velocities along symmetry directions of MnF_2.

$\vec{k}$ ||	$\hat{e}$ ||	ρv^{2*}	v (10^5 cm/sec)
[001]	[001]	C_{33}	V_L = 6.652
[001]	$\perp$[001]	C_{44}	V_T = 2.854
[100]	[100]	C_{11}	V_L = 5.271
[100]	[010]	C_{66}	V_{FT}= 4.437
[100]	[001]	C_{44}	V_{ST} = 2.854
[110]	[110]	$\frac{1}{2}(C_{11}+C_{12}+2C_{66})$	V_L = 6.676
[110]	[001]	C_{44}	V_{FT}= 2.854
[110]	[1$\bar{1}$0]	$\frac{1}{2}(C_{11}-C_{12})$	V_{ST}= 1.703

*The values used for the elastic constants in 10^{11} dynes/cm^2 were C_{11} = 10.92, C_{33} = 17.39, C_{44} = 3.202, C_{66} = 7.736, C_{12} = 8.64 and C_{13} = 7.46.

FIG. 5.1 Phonon velocities in the (001) plane of MnF_2. Phase velocities are shown by the solid lines and group velocities by the dashed lines.

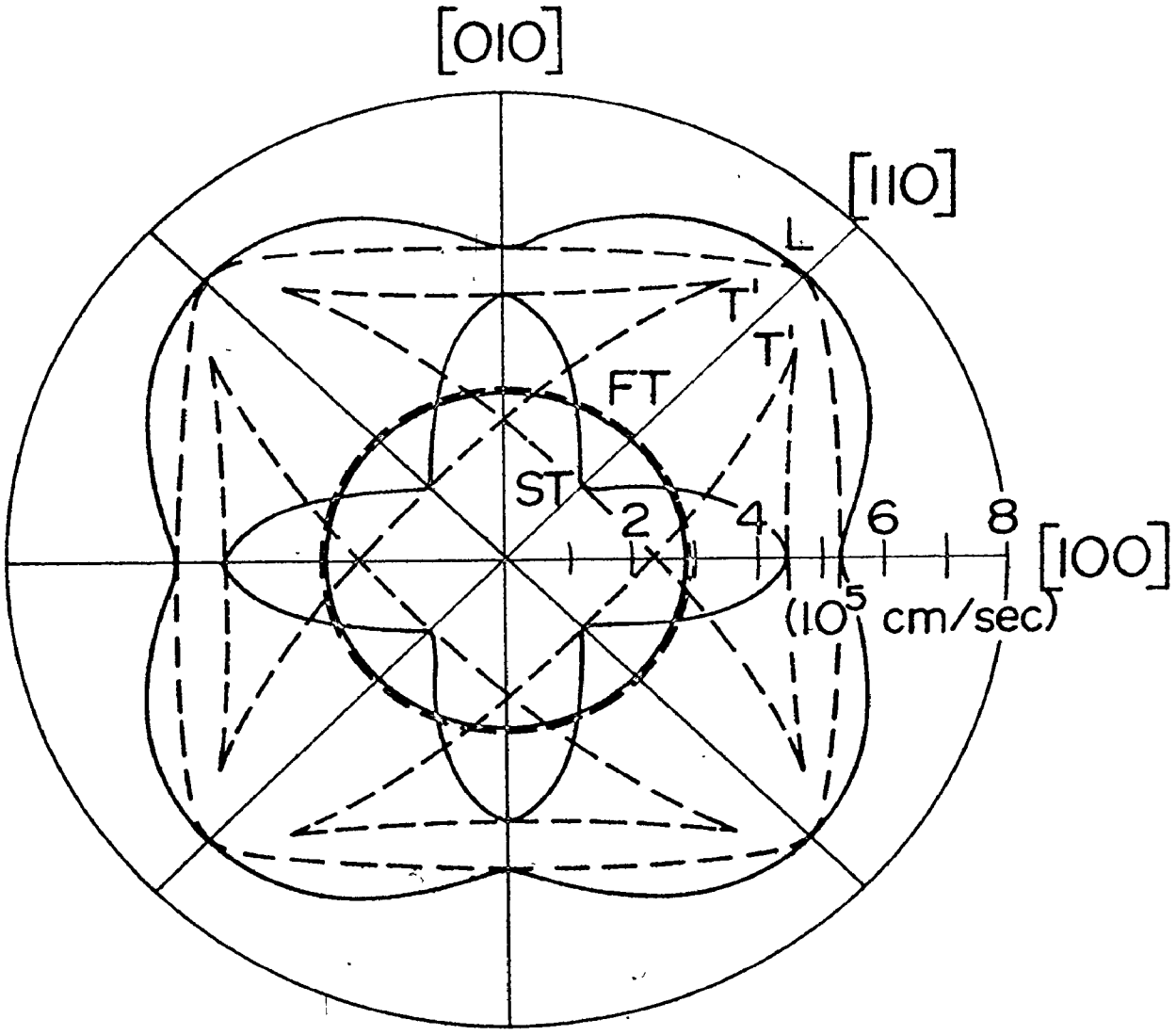
[010]
[110]
[100]
L
T'
T'
FT
ST
2
4
6
8
(10^5 cm/sec)

FIG. 5.2 Phonon velocities in the $(0\bar{1}0)$ plane of MnF_2. Phase velocities are shown by the solid lines and group velocities by the dashed lines.

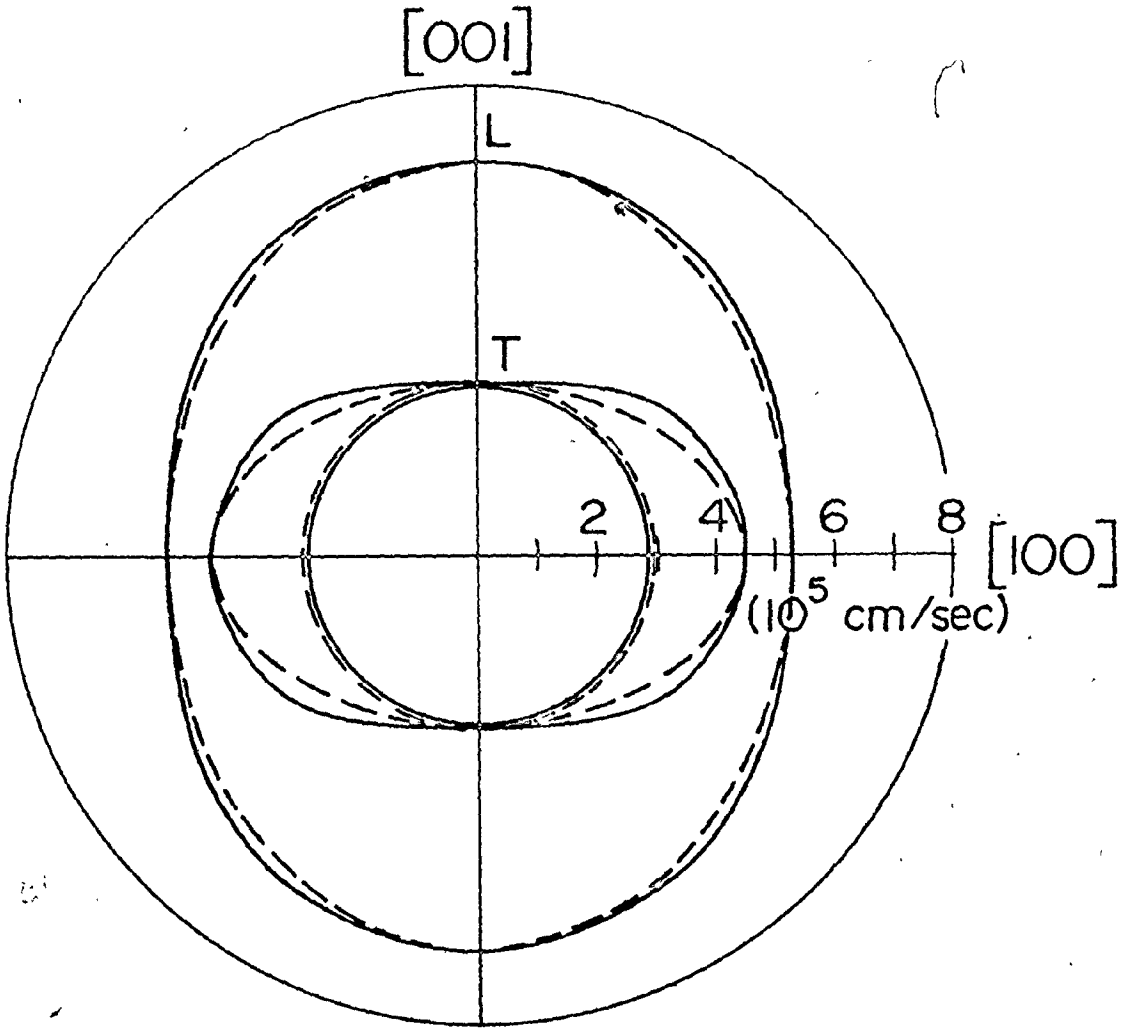
[001]
L
T
2
4
6
8
[100]
(10^5 cm/sec)

FIG. 5.3 Phonon velocities in the $(1\bar{1}0)$ plane of MnF_2. Phase velocities are shown by the solid lines and group velocities by the dashed lines.

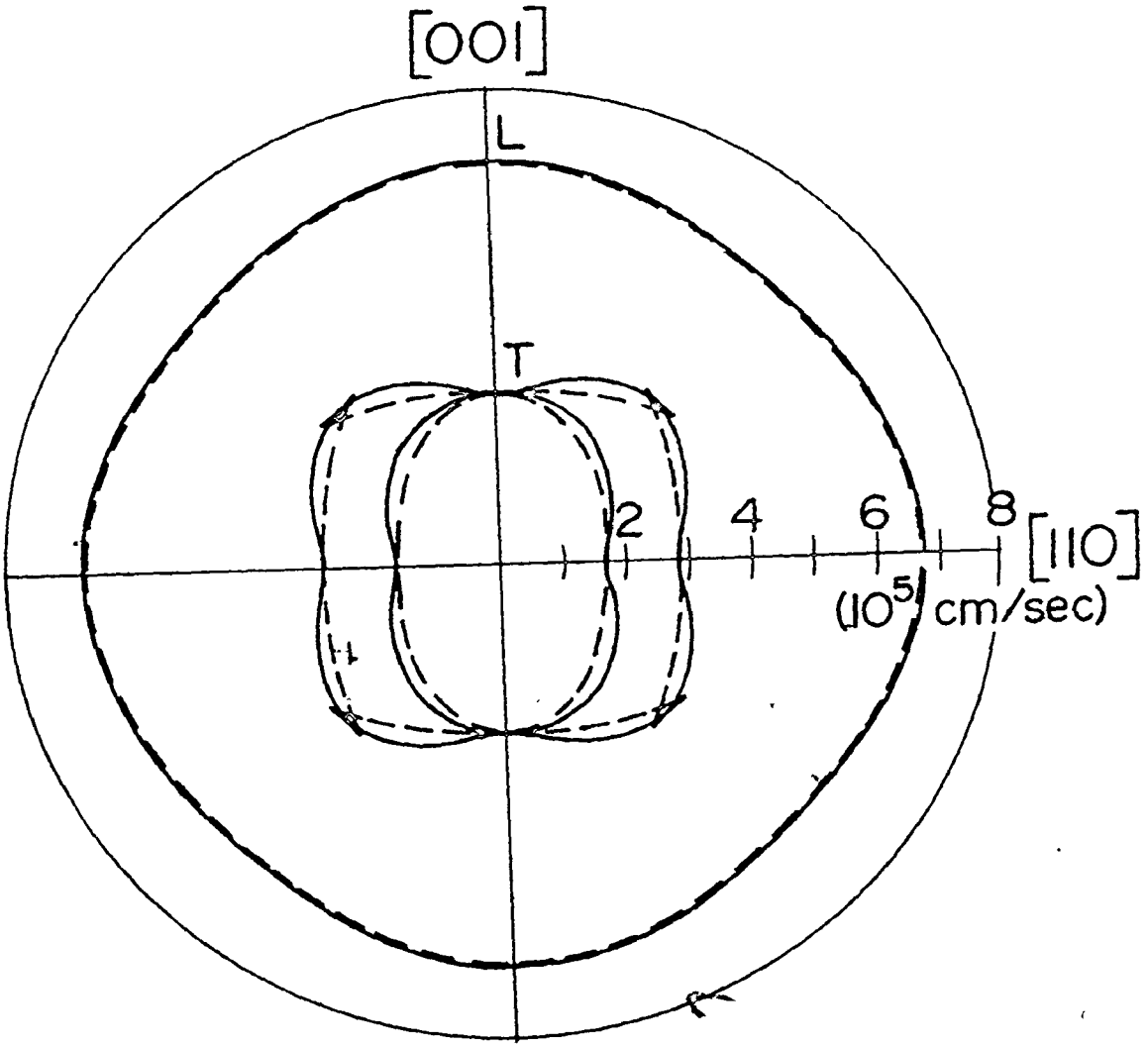
[001]
L
T
2
4
6
8
[110]
(10^5 cm/sec)

The angle between a group velocity vector in the tip of one of these cusps and its associated phase velocity vector can be as much as 60°. This large deviation is due to the large anisotropy in this phase velocity surface. In contrast, the other transverse velocity surface is isotropic, so the phase and group velocity vectors coincide. In the $(0\bar{1}0)$ and $(1\bar{1}0)$ planes, shown in Figs. 5.2 and 5.3, there is little anisotropy, so the differences between the phase and group velocity surfaces are not very large.

These diagrams do not show the effects of phonon focusing[51]. Because of elastic anisotropy, even a uniform angular distribution of phase velocity vectors may produce group velocity vectors which are bunched around certain directions. Thus, the energy flux will be focused, or enhanced in these directions, and defocused, or decreased in other directions. Focusing effects will be discussed in the following sections.

B. Thermal Conductivity

The first step in quantitatively fitting the thermal conductivity results is to calculate the boundary limited conductivity. If the isotropic approximation is used, then from equation (2.27), the Casimir limit[37] is

$$K_b^c = \frac{2\pi^2}{45} \frac{k_B^4 T^3}{\hbar^3} D\left(\frac{1}{v_L^2} + \frac{2}{v_T^2}\right) \qquad (5.1)$$

where v_L and v_T are the phase velocities along the [001] heat

flow direction. Using the velocities listed in Table 5.1, this gave a boundary limit of $K_b^c = 0.364\ D\ T^3$ watts $cm^{-1} \cdot K^{-1}$.

The experimentally measured conductivity was higher than the Casimir limit at the lowest temperature. Since the results show no evidence for a magnon contribution to the total conductivity, this higher value is probably due to phonon focusing effects. These were included by numerically calculating the boundary limit using equation (2.26),

$$K_b = \frac{2}{45} \frac{k_B^4 T^3}{\hbar^3} D \sum_i \int \frac{v_G(\Omega,i)}{v^3(\Omega,i)} \frac{\cos^2\theta_G(\Omega,i)}{\sin\theta_G(\Omega,i)} d\Omega \qquad (5.2)$$

where the phase and group velocities for each mode (Ω,i) were calculated using the techniques outlined in the previous section. This gave a boundary limit $K_b = 0.438\ D\ T^3$ watts $cm^{-1}\ K^{-1}$, which is about 20% higher than the Casimir limit. This is shown as the solid line in Fig. 5.4.

As pointed out in Chapter II, the resonant interaction of the phonons with the impurity produces a gap in the phonon spectrum at the resonant frequency. This shifts the phonon frequencies and alters the dispersion relations. However, the assumption was made that the gap was small so that the differences between the perturbed and unperturbed frequencies and velocities could be neglected. Therefore, the conductivity could be calculated using equation (2.21),

$$K = \frac{1}{(2\pi)^3} \frac{k_B^4 T^3}{\hbar^3} \sum_i \int \frac{v_G^2(\Omega,i)}{v^3(\Omega,i)} \cos^2\theta_G(\Omega,i) \int \frac{x^4 e^x}{(e^x-1)^2} \tau_T(x,\Omega,i)\, dx\, d\Omega \qquad (5.3)$$

FIG. 5.4 Calculated temperature dependence of the thermal conductivity for sample TC3. The calculated limit for boundary scattering is shown. The solid line is the best fit to the experimental results.

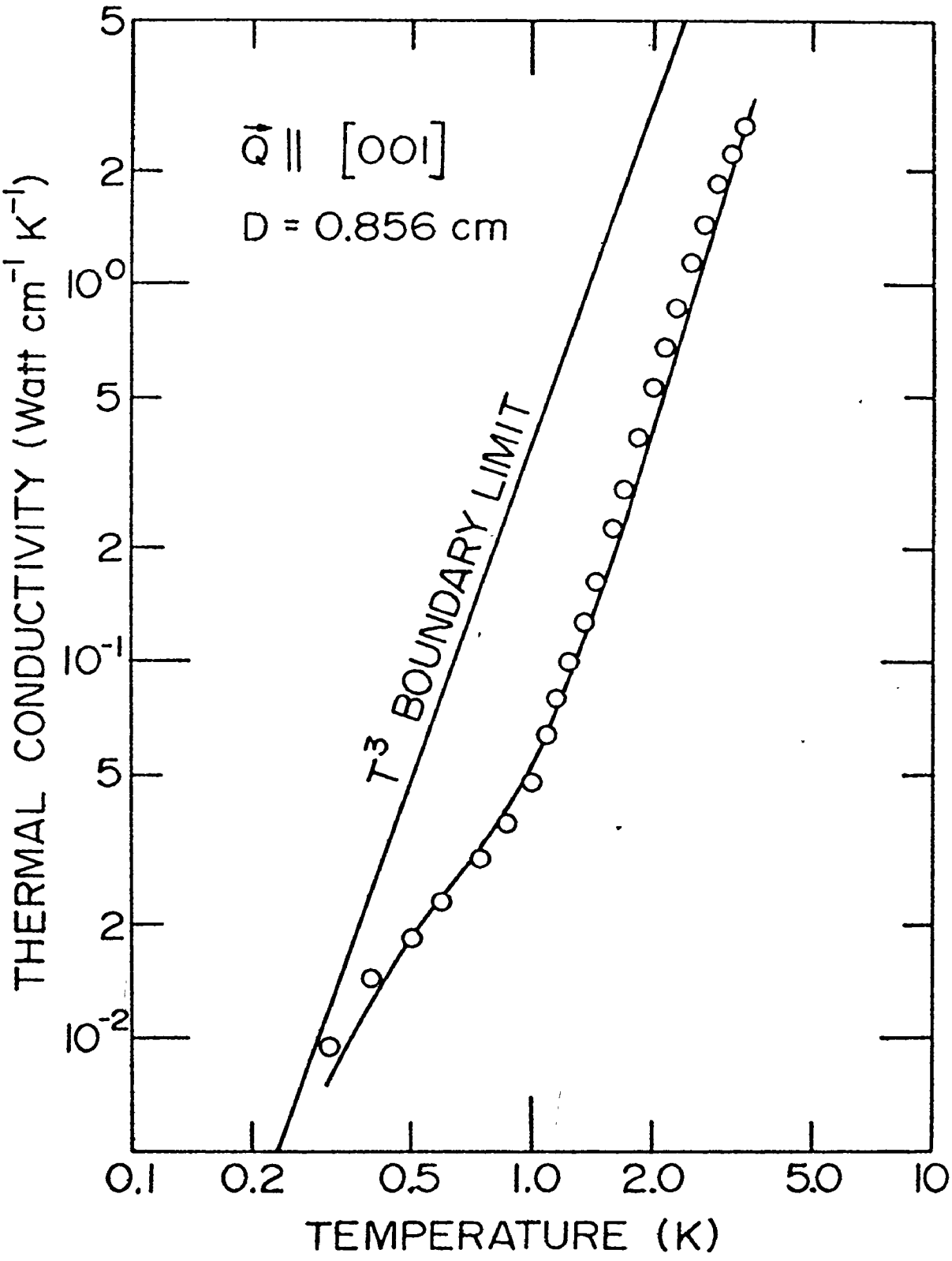
$\vec{Q} \parallel [001]$
D = 0.856 cm
T^3 BOUNDARY LIMIT
THERMAL CONDUCTIVITY (Watt cm^{-1} K^{-1})
TEMPERATURE (K)
5
2
10^0
5
2
10^{-1}
5
2
10^{-2}
0.1
0.2
0.5
1.0
2.0
5.0
10

where $x = \hbar\omega/k_B T$. The validity of this assumption will be examined later in this chapter.

To use equation (5.3), a suitable expression for the total relaxation time τ_T must be chosen. The shape of the conductivity curve suggests that, over the temperature range of interest, the important phonon scattering processes are boundary scattering, point defect scattering, and resonant scattering. From equations (2.25) and (2.28), the relaxation rates for the first two processes are

$$\tau_b^{-1}(\Omega,i) = \frac{3\pi}{4} \frac{\sin\theta_G(\Omega,i)}{D} \quad v_G(\Omega,i) \tag{5.4}$$

and

$$\tau_p^{-1}(x,\Omega,i) = B \frac{\omega^4}{v^4} = B' \frac{T^4 x^4}{v^4(\Omega,i)} \tag{5.5}$$

where $B' = (k_B/\hbar)^4 B$ is an adjustable parameter for the strength of the point defect scattering.

The heat pulse and elastic constant measurements suggest that it is the phonons of E_g symmetry associated with the C_{44} elastic constant which are being resonantly scattered. This is consistent with recent measurements of the thermal conductivity of MnF_2 by Hartmann[19]. The conductivity was measured for two samples cut from the same boule, one with heat flow along the [001] direction, and the other along the [100] direction. It was found that the low temperature conductivity was higher for the [100] direction, even though the boundary limits were about the same for both samples. This suggests that the resonance dip was

shallower for heat flow along the [100] axis. From Table 5.1, it can be seen that along this direction, only one transverse mode has E_g symmetry. Therefore, if only E_g phonons are resonantly scattered, the other transverse mode can still carry a considerable amount of heat.

From equation (2.33), the resonant relaxation rate for the E_g phonons can be expressed as

$$\tau_{E_g}^{-1} = \frac{2A^2\rho_i}{\pi v_{E_g}^3} \frac{\omega^4}{(\omega^2-\omega_o^2)^2} \tanh \frac{\hbar\omega_o}{2k_BT} \qquad (5.6)$$

where the changes in the dispersion relations have again been neglected. Since these phonons travel along symmetry directions, their group velocity equals their phase velocity, $v_{E_g} = (C_{44}/\rho)^{1/2}$. In terms of the dimensionless variable x, equation (5.6) becomes

$$\tau_{E_g}^{-1}(x) = \frac{A'}{v_{E_g}^3} \frac{x^4}{(x^2-x_o^2)^2} \tanh \frac{x_o}{2} \qquad (5.7)$$

where $A' = 2A^2\rho_i/\pi$, and $x_o = \hbar\omega_o/k_BT$ are adjustable parameters for the strength and frequency of the scattering.

Any phonon mode (Ω,i) will in general have some component of E_g symmetry, and therefore will have a certain resonant relaxation rate. This can be calculated in the following manner. An unscattered phonon can be thought of as an elastic wave with a time dependence $e^{i\omega t} = e^{ikvt}$, where v is the phase velocity. Therefore, the time dependence of a scattered wave can be expressed in terms of a complex phase velocity $\tilde{v} = v + iv''$, by $e^{i\omega t}e^{-t/\tau} = e^{ik\tilde{v}t}$, where the imaginary part of the phase velocity is related to the relaxation rate by $\tau^{-1} = kv''$.

In particular, if one assumes a value for the relaxation rate of an E_g phonon with some particular frequency ω, the imaginary part of the phase velocity of this phonon can be calculated from

$$\tau_{E_g}^{-1} = kv''_{E_g} = \omega v''_{E_g}/v_{E_g} \quad . \tag{5.8}$$

This in turn allows a complex elastic constant for this phonon to be calculated from

$$\tilde{C}_{44} = \rho \tilde{v}_{E_g}^{\ 2} \quad . \tag{5.9}$$

If this complex elastic constant is then used in equation (2.22), the phase velocity that is computed numerically for a phonon in any direction will in general also be complex. From the imaginary part of the phase velocity, the resonant relaxation rate for this general phonon can be expressed as

$$\tau_r^{-1} = kv'' = \omega v''/v \quad . \tag{5.10}$$

By combining equations (5.10) and (5.8), the ratio of the relaxation rate of a general phonon to that of an E_g phonon with the same frequency is

$$\frac{\tau_r^{-1}}{\tau_{E_g}^{-1}} = \frac{v''}{v''_{E_g}} \frac{v_{E_g}}{v} \quad . \tag{5.11}$$

By using the above procedure to calculate this ratio numerically, it was found to be independent of the initial value chosen for $\tau_{E_g}^{-1}$. The ratio depends only on the component of E_g symmetry in the general phonon. Therefore, the resonant relaxation rate for any phonon (Ω,i) can be expressed as

$$\tau_r^{-1}(x,\Omega,i) = \frac{v''(\Omega,i)}{v''_{E_g}} \frac{v_{E_g}}{v(\Omega,i)} \tau_{E_g}^{-1}(x) \qquad (5.12)$$

where the ratio $v''(\Omega,i)/v''_{E_g}$ had to be calculated only once for each mode (Ω,i)

By combining equations (5.12), (5.7), (5.5), and (5.4), the total relaxation rate is found to be

$$\tau_T^{-1}(x,\Omega,i) = \frac{3\pi}{4} \frac{\sin\theta_G(\Omega,i)}{D} v_G(\Omega,i) + \frac{B'T^4x^4}{v^4(\Omega,i)} + \frac{v''(\Omega,i)}{v''_{E_g}} \frac{A'}{v(\Omega,i)v_{E_g}^2} \frac{x^4}{(x^2-x_o^2)^2} \tanh\frac{x_o}{2} . \qquad (5.13)$$

After substituting (5.13) into (5.3), the resulting expression was used to numerically calculate the conductivity as a function of temperature, using A', B', and x_o as adjustable parameters. The best fit, shown as a solid line in Fig. 5.4, was achieved using $A' = 1.8\times10^{23}$ cm^3sec^{-4}, $B' = 1.0\times10^{22}$ $cm^4sec^{-5}K^{-4}$, and $x_o/T = 4.0$. Therefore, from the computer fit the resonant frequency of the impurity is $\hbar\omega_o/k_B = 4.0$ K, compared to the value of 3.8 K estimated by "rule of thumb" in Chapter IV. While the fit shown in Fig. 5.4 is not perfect, it must be emphasized that only three adjustable parameters were used.

Many other expressions for phonon resonant relaxation rates have been suggested, some phenomenological[39,40,89], and others based on theoretical considerations[90]. An attempt was made to fit the conductivity with the empirical relaxation rate used by Pohl[39,91],

$$\tau_R^{-1} = \frac{A\omega^2}{(\omega^2-\omega_o^2)^2} . \qquad (5.14)$$

However, the best fit was much poorer than that achieved using expression (5.6).

The thermal conductivity was also calculated using (5.6), but making the isotropic approximation which neglects all the angular dependence in the conductivity integral. Again, the best fit was worse than that shown in Fig. 5.4. Moreover, it is important to include the modal dependence so that the resonant scattering parameters which are calculated are those appropriate for the E_g phonon, rather than an average over all phonon modes. Thus, these are the correct parameters to compare to the heat pulse and elastic constant results.

C. Heat Pulses

It can be shown quantitatively that the attenuation of the E_g heat pulse is caused by the same resonant scattering that was noted in the thermal conductivity. The usual method[56] for extracting information about scattering rates from a heat pulse experiment involves fitting a theoretical expression to the attenuated pulse height versus pulse temperature curve, in much the same fashion that the thermal conductivity curve was fitted. However, since the heat pulse measurements showed no appreciable variation with T_h over the range that could be investigated, an alternate method of analyzing the results was used. First, the heat pulse signals for ballistic propagation were calculated numerically, being careful to include phonon focusing effects. Then, the attenuation factors were calculated using the scattering

parameters obtained from the thermal conductivity fit. It was shown that including these factors in the calculation of the heat pulse signal gave relative pulse heights which agreed with the experimental results.

The ballistic pulse heights were calculated using the following model. It was assumed that the heater generated a uniform angular distribution of phonon wave vectors in the sample[51]. A computer program was written which calculated the three phase and group velocity vectors for each wave vector using equations (2.22) and (2.23). Wave vectors were chosen at solid angle intervals of $\frac{1}{2}° \times \frac{1}{2}°$. If a group velocity vector $\vec{v}_G$ fell within the solid angle subtended by the bolometer at the heater, its path length ℓ to the bolometer, and its arrival time $t_o = \ell/v_G$ were calculated. The solid angle was adjusted to take into account the finite size of the heater. After including the finite duration of the input pulse, the number of phonons arriving at the bolometer in each 10 nsec interval was counted, thus producing a histogram of the heat pulse signal.

The relative pulse heights also depend on the relative abundances of transverse and longitudinal phonons generated in the sample by the heater. From equation (2.58), the intensity of a given polarization is proportional to the inverse square of the velocity of that polarization in the heater. Therefore, the count of a transverse phonon was weighted relative to that for a longitudinal phonon by a factor v_{hL}^2/v_{hT}^2, which for a constantan heater

is 3.94.

The calculated ballistic pulse signals, normalized to the longitudinal pulse height, are shown by the dotted lines in Figs. 5.5-5.7. It can be seen that in all cases, the arrival times of the calculated pulses agree very well with the experimental results.

The computer model correctly predicts the extra heat pulse, labelled T' in Fig. 5.6. The origin of the phonons responsible for this pulse can be seen by referring to the [110] direction in Fig. 5.1. Since fairly thin samples were used, the bolometer subtended a large solid angle at the heater (about 22.5° on either side of the [110] direction in Fig. 5.1). Thus, phonons in the cusps labelled T' were detected by the bolometer. The T' pulse is fairly large because phonons are strongly focused into the tips of these cusps.

As noted in section A of this chapter, there are large angles between the group velocity vectors in these cusps and their associated phase velocities. In fact, some of these phase velocities are at angles as small as 10° to the heater-sample boundary (which corresponds to the $[1\bar{1}0]$ direction in Fig. 5.1). However, the phase velocities across the interface obey an acoustic Snell's law, which from equation (2.47) can be expressed as

$$\frac{\cos\phi_h}{v_h} = \frac{\cos\phi_s}{v_s} \qquad (5.15)$$

where ϕ_h and ϕ_s are the angles between the interface and the phase velocities, $\vec{v}_h$ and $\vec{v}_s$ in the heater and sample respectively.

FIG. 5.5 Calculated heat pulses for sample HP2. The solid line is the experimental result. The dotted line is the pulse signal calculated without scattering, and the dashed line, including scattering.

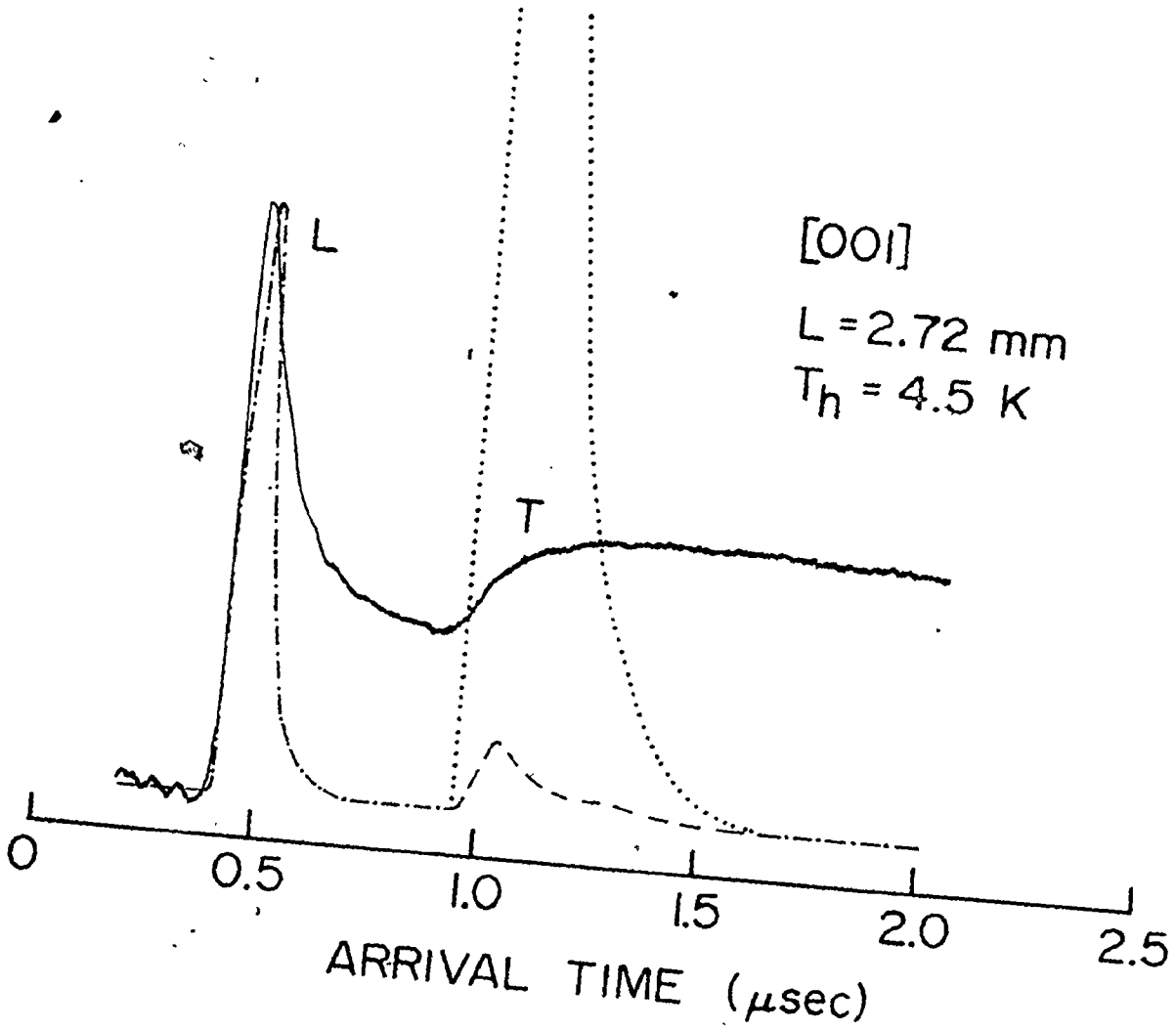
L
T
[001]
L = 2.72 mm
T_h = 4.5 K
0
0.5
1.0
1.5
2.0
2.5
ARRIVAL TIME (μsec)

FIG. 5.6 Calculated heat pulses for sample HP3. The solid line is the experimental result. The dotted line is the pulse signal calculated without scattering, and the dashed line, including scattering.

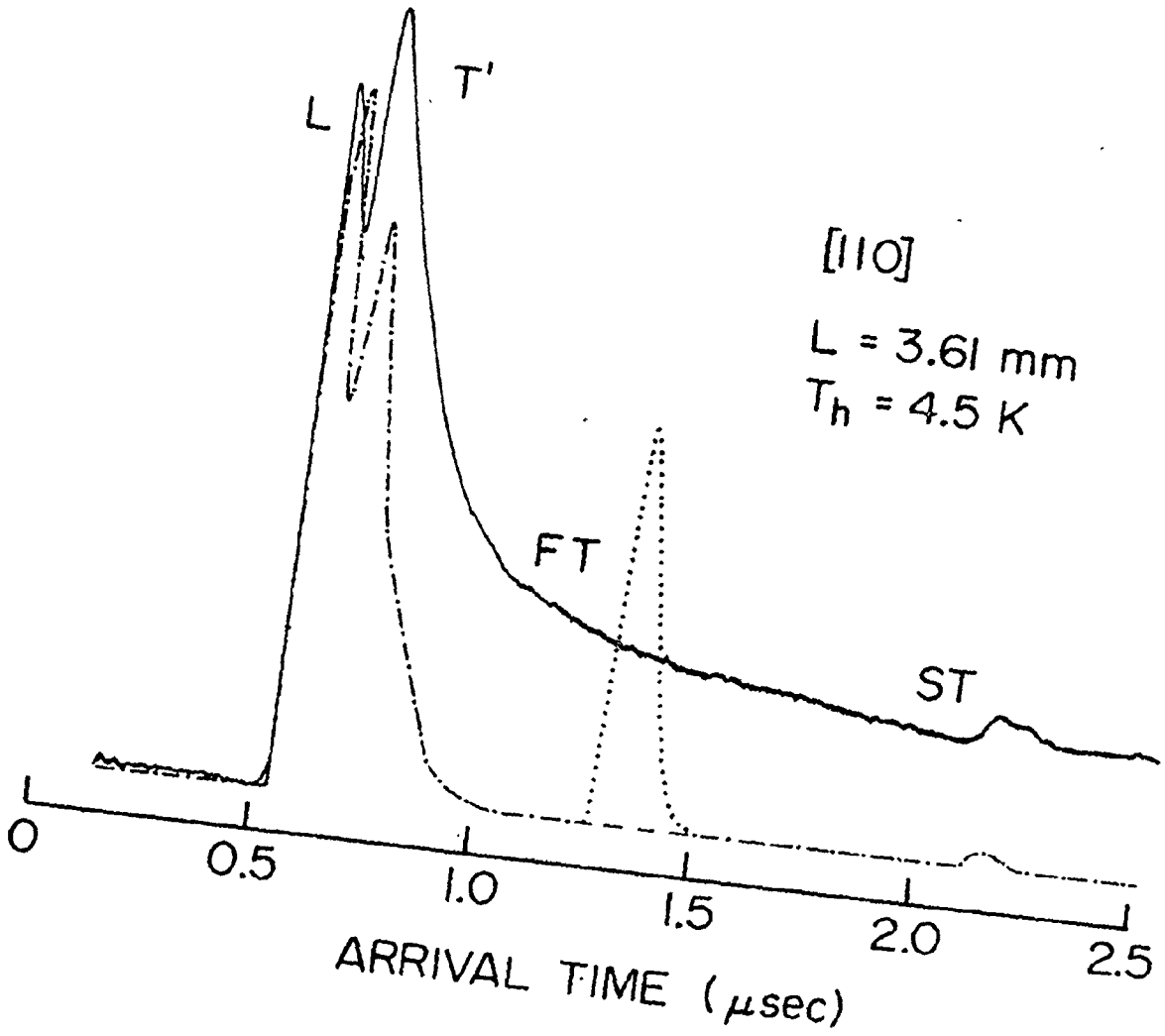
L
T'
[110]
L = 3.61 mm
T_h = 4.5 K
FT
ST
0
0.5
1.0
1.5
2.0
2.5
ARRIVAL TIME (μsec)

FIG. 5.7 Calculated heat pulses for sample HP5. The solid line is the experimental result. The dotted line is the pulse signal calculated without scattering, and the dashed line, including scattering.

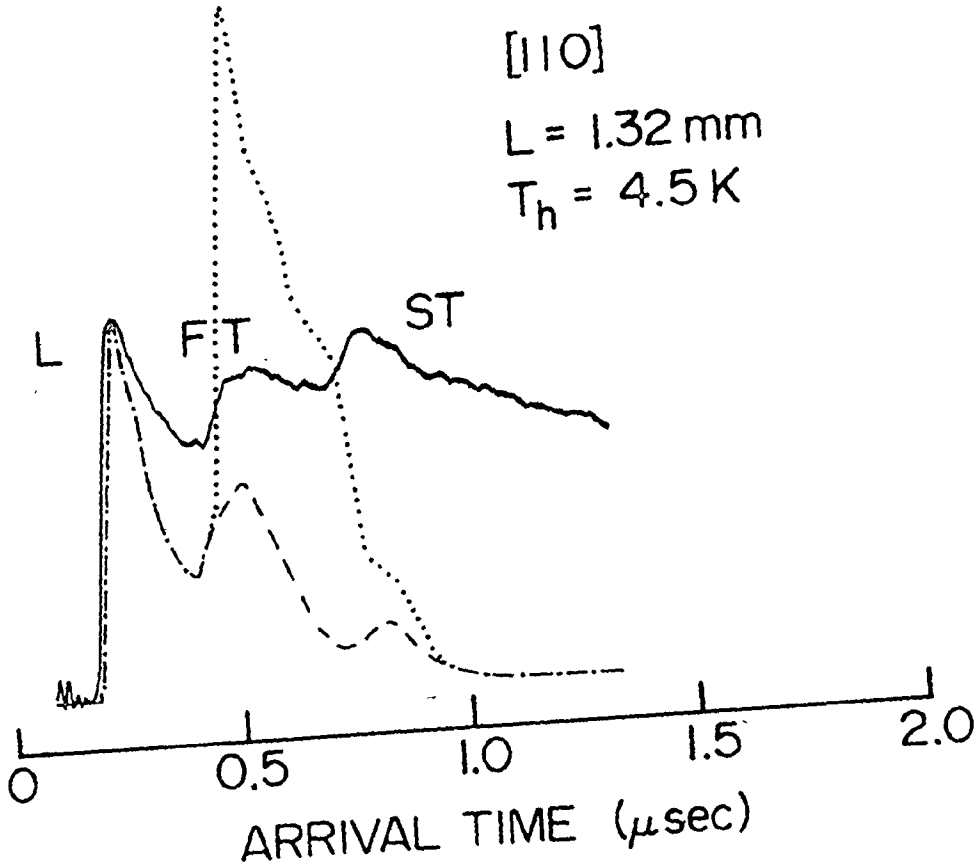
[110]
L = 1.32 mm
T_h = 4.5 K
L
FT
ST
0
0.5
1.0
1.5
2.0
ARRIVAL TIME (μsec)

It is the phase velocity, not the group velocity which follows the acoustic Snell's law. The situation is analogous to the propagation of the extraordinary light ray in doubly refracting crystals. The phase velocity of the E ray, rather than its group velocity, obeys the optical Snell's law.

From equation (5.15), if $v_s < v_h$, phonon wave vectors cannot be generated in the sample at an angle less than the critical angle,

$$\phi_s^c = \cos^{-1}(v_s/v_h). \qquad (5.16)$$

In Fig. 5.1, the critical angle is about 17° to the $[1\bar{1}0]$ direction. It was found that it was necessary to include this condition in the computer model in order to obtain the correct shape for the T' pulse. Critical angles for propagation across an interface have also been observed experimentally for phonon radiation from a solid into liquid helium[92].

For the thinner [110] sample shown in Fig. 5.7, the L and T' pulses are not resolved. This is correctly predicted by the computer model. For both [110] samples, the relatively large L and small ST pulses are due to the fact that longitudinal phonons are strongly focused into the $[1\bar{1}0]$ direction, while slow transverse phonons are strongly defocused. In the [001] direction, focusing effects are not as important. The ballistic transverse pulse is predicted to be much larger than the longitudinal pulse, as shown in Fig. 5.5.

With the exception of the pulses associated with the E_g

phonons, the calculated ballistic pulse heights in Figs. 5.5-5.7 agree fairly well with the experimental pulse heights above the diffusive background. The agreement is quite good, considering the approximations made in the perfect-coupling black-body model. The fact that the calculated E_g ballistic pulse heights do not agree with experiment is further evidence that these pulses have indeed been attenuated.

This attenuation can be included in the calculation by multiplying the count of each phonon (Ω,i) in the histogram by the factor given by equation (2.65),

$$\frac{I_B'(\Omega,i)}{I_B(\Omega,i)} = \frac{15}{\pi^4}\frac{T_h^4}{T_h^4-T_s^4}\int g(x,T_h,T_s)e^{-t_o/\tau_T(x,\Omega,i)}dx \qquad (5.17)$$

where $x = \hbar\omega/k_BT_h$. The total relaxation rate τ_T^{-1} is given by the sum of the point defect and resonant scattering rates. From equations (5.12), (5.6) and (5.5), this can be expressed as

$$\tau_T^{-1}(x,\Omega,i) = \frac{B'T_h^4x^4}{v^4(\Omega,i)} + \frac{v''(\Omega,i)}{v_{E_g}''}\frac{A'}{v(\Omega,i)v_{E_g}^2}\frac{x^4}{(x^2-x_o^2(T_h))^2}\tanh\frac{x_o(T_s)}{2} \qquad (5.18)$$

where $x_o(T_h) = \hbar\omega_o/k_BT_h$, and $x_o(T_s) = \hbar\omega_o/k_BT_s$. The tanh function in the resonant relaxation rate refers to the populations of the impurity levels[42,43] which depend on the ambient sample temperature T_s rather than the heat pulse temperature T_h.

The attenuation factors given by (5.17) were included in the computer calculation using the same parameters A', B', and ω_o

that were calculated from the thermal conductivity fit. This assumes that the impurity concentration in the heat pulse samples was the same as that in the thermal conductivity sample. This is probably a fairly good assumption. Preliminary heat pulse experiments were performed with a small slice cut from one end of the thermal conductivity sample TC3. With propagation along the [001] direction, the heat pulse signal was very similar to that shown in Fig. 5.5. The transverse pulse was highly attenuated relative to the longitudinal pulse.

The pulse signals calculated by including the attenuation are shown by the dashed lines in Figs. 5.5-5.7, normalized to the longitudinal pulse height. These results were calculated for T_s = 2.0 K, and T_h = 4.5 K. Only the relative heights of the pulses associated with E_g phonons changed appreciably from their ballistic value. As can be seen from the diagrams, these pulse heights now agree fairly well with the experimental results. The calculations were also carried out for other pulse temperatures in the range 2.5-6.0 K. The calculated relative pulse heights showed little variation with T_h, as was found experimentally.

The heat which is scattered out of the ballistic pulses arrives diffusively at the bolometer. This was not included in the calculations. However, it was noted that the experimental diffusive tails agree qualitatively with the shapes predicted by equation (2.67) .

D. C_{44} Elastic Constant

As mentioned in the previous chapter, Melcher[33] noted an anomalous decrease in the C_{44} elastic constant of MnF_2 at low temperatures. His results[93] below 20 K are shown in Fig. 5.8. This effect could be due to the decrease in the velocity of sound produced by the interaction of the E_g elastic waves with the impurity. This would produce an elastic constant,

$$C'_{44} = \rho v'^2_{E_g} = \rho v^2_{E_g} (1 + \frac{\Delta\omega}{\omega})^2 \qquad (5.19)$$

where v'_{E_g} and v_{E_g} are the perturbed and unperturbed phase velocities for this mode, and $\Delta\omega = \omega' - \omega$ is the change in frequency for a given wave vector due to the interaction. If the fractional frequency shift is assumed to be small, (5.19) becomes

$$C'_{44} \approx C_{44}(1 + 2\frac{\Delta\omega}{\omega}) \qquad (5.20)$$

where C_{44} is the unperturbed elastic constant.

From the thermal conductivity fit, the impurity resonant frequency is $\omega_o = k_B T x_o/\hbar = 5.2\times10^{11}$ sec^{-1}. The elastic constant measurements were performed at a frequency ν = 31 MHz. Therefore, ω'^2 can be neglected compared to ω_o^2 in equation (2.31) for the fractional frequency shift. Substituting this into (5.20), the elastic constant can be expressed as

$$C'_{44}(T) \approx C_{44}(1 - \frac{2A\rho_i}{\omega_o^2} \tanh \frac{\hbar\omega_o}{2k_B T}) \qquad (5.21)$$

which is a function of temperature because the difference in population between the ground and excited impurity levels increases as the temperature is lowered[41].

FIG. 5.8 Temperature dependence of the C_{44} elastic constant of MnF_2. The data was obtained from R. L. Melcher (reference 33). The solid line is the best fit to the experimental results.

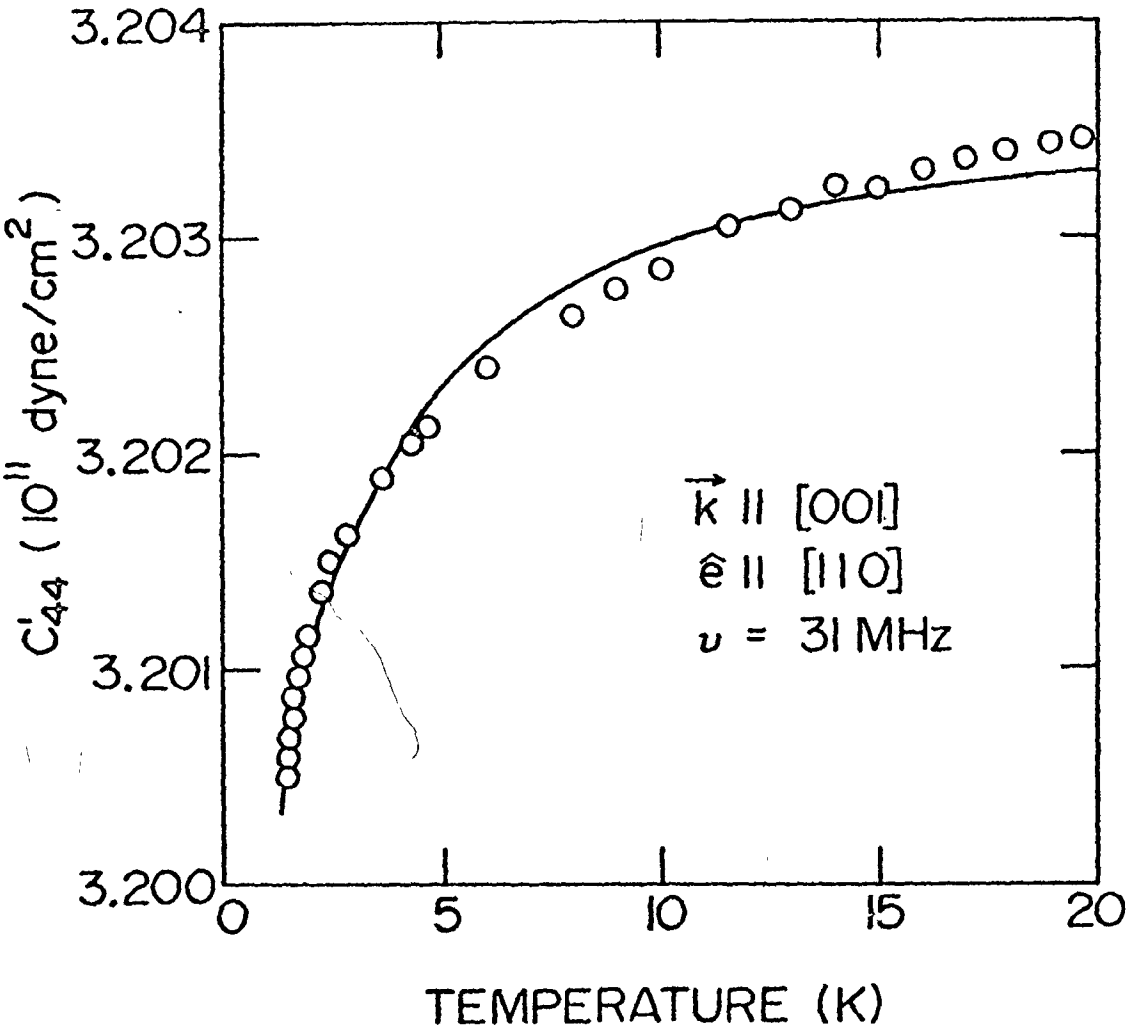
3.204
3.203
3.202
3.201
3.200
C'_{44} (10^{11} dyne/cm^2)
0
5
10
15
20
TEMPERATURE (K)
$\vec{k}$ II [001]
$\hat{e}$ II [110]
υ = 31 MHz

Assuming that the unperturbed C_{44} was independent of temperature below 20 K, expression (5.21) was fitted to the elastic constant data, using C_{44} and $A\rho_i$ as adjustable parameters. The best fit, shown as the solid line in Fig. 5.8, was obtained using $C_{44} = 3.2037\times10^{11}$ dynes/cm^2, and $A\rho_i = 1.5\times10^{20}$ sec^{-2}. The agreement with the experimental data is reasonable. The discrepancy at higher temperatures is probably due to the assumption that C_{44} is temperature independent. Melcher's data above 20 K[33] suggest that the unperturbed elastic constant may still be changing slightly with temperature. The fit is not very sensitive to the value chosen for ω_o. Nevertheless, the fit was appreciably worse for ω_o much larger or much smaller than 5×10^{11} sec^{-1}. This suggests that this effect is indeed caused by the same impurity that was responsible for the resonant scattering in the thermal conductivity and heat pulse experiments.

If it is assumed that Melcher's samples (which were also obtained from Optovac) contained roughly the same impurity concentration as the thermal conductivity sample, then an estimate of this concentration can be made. From the conductivity fit, it was found that $A^2\rho_i = \pi A'/2 = 2.8\times10^{23}$ cm^{3}sec^{-4}. Combining this with the fitted value for $A\rho_i$, one finds that $A = 1.9\times10^3$ cm^{3}sec^{-2}, and $\rho_i = 8.0\times10^{16}$ cm^{-3}. Even allowing for the assumptions made in this estimate, this suggests that the impurity concentration is very low. Therefore, the impurity must be a strong phonon scatterer to produce a large depression of the

FIG. 5.9 Calculated dispersion relations for the E_g phonon mode. The calculation is for a temperature of 1.0 K.

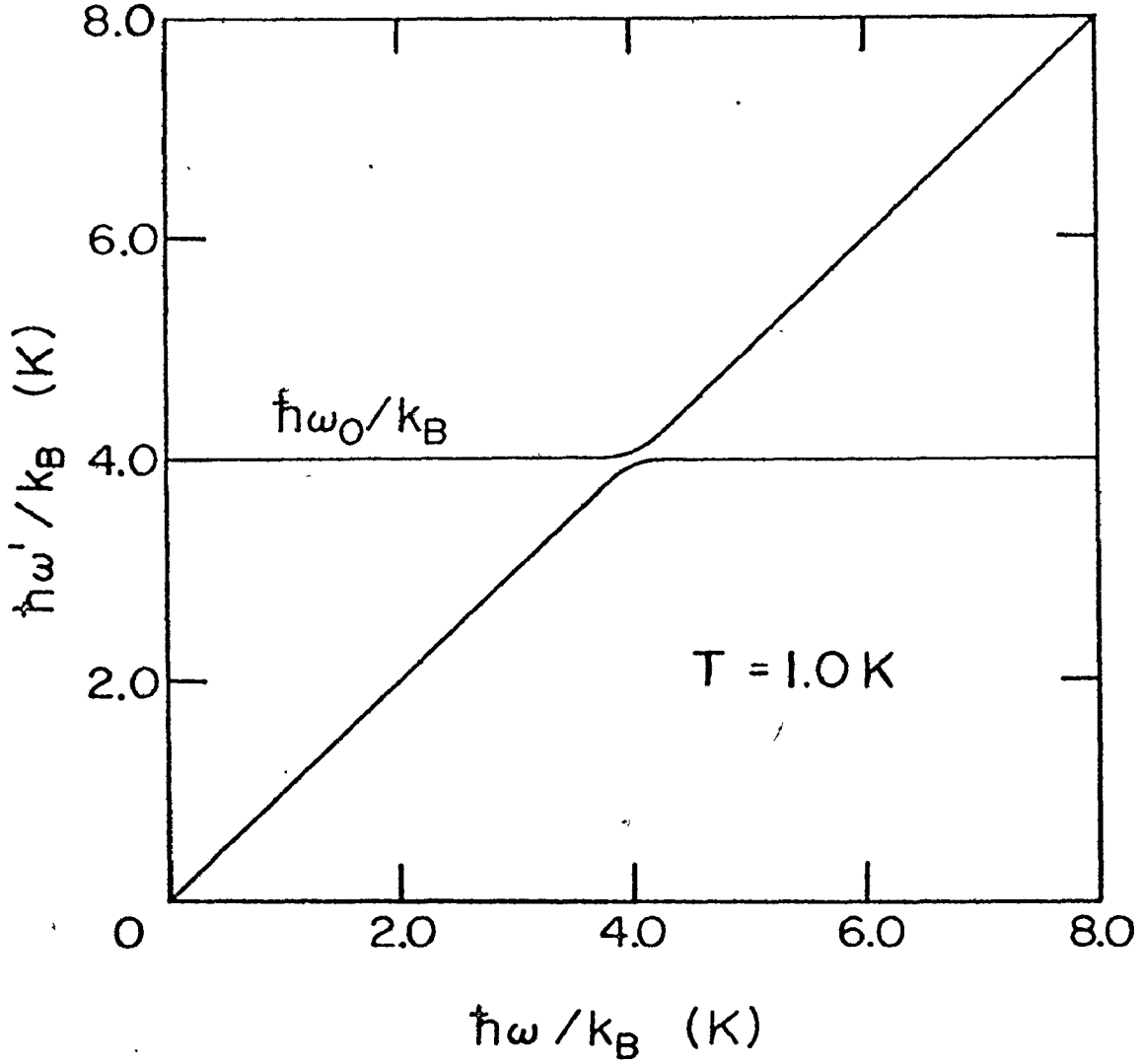
8.0
6.0
4.0
2.0
0
2.0
4.0
6.0
8.0
$\hbar\omega_0/k_B$
$\hbar\omega'/k_B$ (K)
$\hbar\omega/k_B$ (K)
T = 1.0 K

thermal conductivity for this low concentration.

Once the value for $A\rho_i$ is known, the dispersion relations for the E_g mode can be calculated from equation (2.31),

$$\frac{\omega'-\omega}{\omega} = \frac{A\rho_i}{\omega'^2-\omega_o^2} \tanh \frac{\hbar\omega_o}{2k_BT} . \qquad (5.22)$$

For a given temperature, this is a cubic equation in ω'. One root is the phonon-like solution, one is the impurity-like solution, and there is one extraneous negative root. The solution to (5.22) is shown in Fig. 5.9 for the temperature T = 1.0 K. This is a dispersion curve because the horizontal axis, $\omega = v_{E_g} k$ is proportional to the wave vector k. It can be seen that only very close to the crossover is the phonon dispersion relation appreciably affected by the coupling to the impurity mode. This is in contrast to other systems like KCl:CN, where the gap can be much larger[41].

This justifies the assumption that the extra dispersion could be neglected in calculating the thermal conductivity. While very accurate ultrasonic techniques allow the dispersion to be measured, even very close to $\omega = 0$, thermal conductivity measurements are not nearly so sensitive. The phonons near the crossover do not contribute to the heat current anyway, so their dispersion is not important. This is unlike the KCl:CN system, where it has been shown[42] that the dispersion should be included in the thermal conductivity calculation.

E. OH^- Tunneling States

So far in this chapter, the identity of the impurity which causes the resonant scattering has not been mentioned. The presence of this impurity in MnF_2 seems to be very common. Large resonance dips, such as that shown for sample TC3, were noted in preliminary thermal conductivity experiments with other Optovac samples. Similar dips have been measured for MnF_2 samples from various sources by other workers[18,19,24].

The impurity is almost certainly OH^-. Experiments at Cornell[24] have shown that intentionally doping an MnF_2 sample with OH^- by adding MnO(OH) to the melt increases the resonance dip at 1.0 K. It has also been noted[18,23] that the MnF_2 powder used as a starting material for the crystal growing process is extremely susceptible to hydrolysis. Various attempts to eliminate these OH^- impurities have been unsuccessful[19,23]. This is not surprising if the impurity concentration is very small, as suggested by the calculation in the previous section.

The question remains as to what is the physical nature of the OH^- impurity states which resonantly scatter the phonons. It is well established in the case of alkali halide crystals that molecular impurities such as OH^- can produce effects similar to those observed in MnF_2. When such a molecule substitutes for a halogen ion, it has several equilibrium orientations in its lattice site, and can tunnel between them. A summary of experimental results concerning tunneling states in alkali halides is presented in a review article by Narayanamurti and Pohl[26].

Tunneling state energy levels typically have small separations of the order of 1 cm^{-1} (1 cm^{-1} corresponds to about 1.44 K). Phonons with these energies cause transitions between the tunneling levels and are resonantly scattered, thus producing dips in the low temperature thermal conductivity. If only two impurity levels are involved in MnF_2, then from the thermal conductivity fit, their separation is predicted to be 4.0 K, or 2.8 cm^{-1}.

The tunneling states are usually very pronounced phonon scatterers, so a small impurity concentration can produce a large depression in the thermal conductivity from its boundary limit. To give just one example, a concentration of about 10^{17} cm^{-3} of OH^- in NaCl reduces the conductivity at 1.0 K by an order of magnitude[89]. This is comparable to the decrease observed in MnF_2 for the calculated concentration of 8×10^{16} cm^{-3}.

The resonant interaction of certain phonon modes with the tunneling states alters the phonon dispersion relations. In several systems[26], this has been evidenced by a decrease in the elastic constants for these modes at low temperatures. From these measurements, a characteristic quantity called the elastic dipole moment α can be calculated. Essentially, α gives the shift in the tunneling state energies for a unit applied stress[26]. This can be calculated for MnF_2 from the resonant scattering strength parameter A. From equation (2.32), A is related to the

energy shift per unit strain W by

$$A = \frac{W^2 \omega_o}{\hbar C_{44}} . \qquad (5.23)$$

Using the calculated values for A and ω_o, W was found to be 1.1×10^{-12} ergs, or 8.0×10^{3} K per unit strain. Therefore, $\alpha = W/C_{44}$ is about 3.4×10^{-24} cm^3. This is the same order of magnitude that is typically found in other systems[26]. For example, $\alpha = 5.9\times10^{-24}$ cm^3 for OH^- in KCl[94].

Because of all these similarities, tunneling states of the OH^- molecule appear to be likely candidates for the resonant scatterers in MnF_2. There is the possibility that the transitions are not between tunneling states, but between hindered rotor,or librator states of the OH^- molecule. However, as pointed out in Chapter II, a free rotor has energy level separations of the order of the rotational constant,

$$B = \hbar^2/2I \qquad (5.24)$$

where I is the moment of inertia of the molecule. Assuming a bond length for the OH^- of 1.0 Å, one finds that B is about 25 K. The splittings between librator levels are even larger than those between free rotors. Therefore, these levels are too far apart to explain a level separation of 4.0 K.

In the remainder of this section, it will be demonstrated that at least one model for OH^- tunneling states in MnF_2 can be constructed which is consistent with the experimental results. In particular, the model predicts that only phonons of E_g symmetry should cause transitions between the tunneling states.

The rutile crystal structure of MnF_2 is shown in Fig. 5.10. The symmetry group is D_{4h}. The lattice constants a and c of the tetragonal unit cell are 4.873 and 3.310 Å respectively[95], where the c axis corresponds to the Z direction in Fig. 5.10. The distance from the F^- ion d to the Mn^{++} ions a or b is 2.11±0.01 Å, while the distance to c is 2.14±0.02 Å[95]. Angle a-d-b is 103.3°, while angle a-d-c is 128.3°.

To start with the simplest model for the tunneling states, it is assumed that as in the case of alkali halides[96], the OH^- molecule substitutes for a halogen ion, and its equilibrium orientations point towards near neighbour cations. Therefore, if the OH^- molecule substitutes for the F^- ion d in Fig. 5.10, it has potential minima in the directions of the Mn^{++} ions a, b, and c. There is no reason to suppose that the molecule sits exactly at the fluorine site d so that a and b are closer to it than c, but lacking any evidence to the contrary, this will be assumed. Therefore, the potential around the OH^- molecule consists of two equivalent potential wells in the directions of a and b, and a slightly shallower well in the direction of c.

The energy levels of the impurity could be found by calculating how the rotational states of the free OH^- molecule are modified when placed in such a potential. This was the approach used by Devonshire[44,45] for the case of octahedral symmetry. In MnF_2 however, the F^- site has the symmetry of the C_{2v} point group[97], and it is difficult to write a simple expression for the potential. However, since only the low lying states are of interest, it is possible to use the tunneling model

FIG. 5.10 Unit cell of MnF_2. The solid circles are Mn^{++} ions, and the open circles, F^- ions. The axes and labels are referred to in the text.

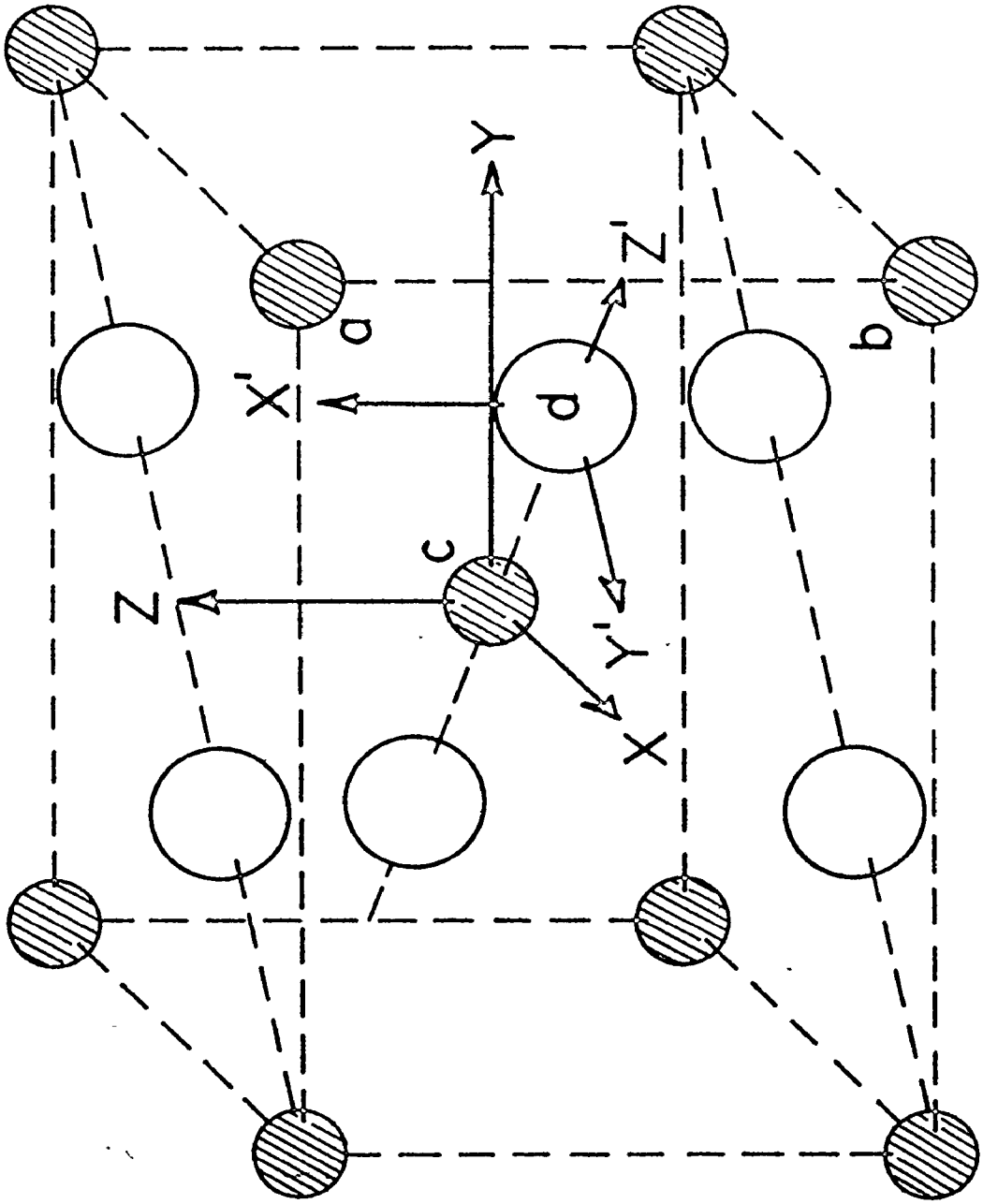
Y
Z'
a
b
X'
d
c
Z
Y'
X

of Gomez et al.[46].

For the moment, the equivalent wells a and b are concentrated on, and the inequivalent well c is neglected. The situation is then analogous to the double well problem that was analyzed in Chapter II. If $|a\rangle$ and $|b\rangle$ represent the ground states of the molecule, localized in wells a and b respectively, then the tunneling states which diagonalize the impurity Hamiltonian are

$$|\psi_1\rangle = (|a\rangle + |b\rangle)/[2(1+S)]^{1/2}$$
$$\text{and} \qquad (5.25)$$
$$|\psi_2\rangle = (|a\rangle - |b\rangle)/[2(1-S)]^{1/2}$$

where $S = \langle a|b\rangle$ is the wavefunction overlap. The corresponding energy levels are

$$E_1 = \langle\psi_1|H|\psi_1\rangle = (E_o+\eta)/(1+S)$$
$$\text{and} \qquad (5.26)$$
$$E_2 = \langle\psi_2|H|\psi_2\rangle = (E_o-\eta)/(1-S)$$

where $E_o = \langle a|H|a\rangle = \langle b|H|b\rangle$, and $\eta = \langle a|H|b\rangle = \langle b|H|a\rangle$.

By noting how $|\psi_1\rangle$ and $|\psi_2\rangle$ transform under the symmetry operations of the C_{2v} group (defined with respect to the X'Y'Z' axes of Fig. 5.10), the eigenstates can be labelled $|\psi_1(A_1)\rangle$ and $|\psi_2(B_1)\rangle$, according to the irreducible representations of C_{2v} that they form[97]. Therefore, neglecting the overlap S compared to unity, the energy levels can be expressed as

$$E_1(A_1) = E_o - \Delta/2$$
$$\text{and} \qquad (5.27)$$
$$E_2(B_1) = E_o + \Delta/2$$

where $\Delta = -2\eta$ is the tunnel splitting. Since $\eta < 0$[46], the ground state is the $E_1(A_1)$ level. If the resonant scattering is

caused by transitions between these two levels, then from the thermal conductivity fit, Δ is 4.0 K.

Including the third potential well c gives rise to another energy level. If the potential barriers between well c and the other two wells were infinite, this level would be

$$E_o' = \langle c|H|c\rangle \tag{5.28}$$

where $|c\rangle$ is the lowest energy state of the molecule when localized in well c. It has been assumed that well c is shallower than a or b, so $E_o' > E_o$. A crude estimate of this energy difference can be made as follows. If the distance from d to c were the same as the distance to a or b, then E_o' would equal E_o. To distort this imaginary lattice so that cd is 2.14 Å, while ad = bd is 2.11 Å, requires an effective strain of $0.03/2.14 = 1.4\times10^{-2}$. Since the energy shift per unit strain is 8.0×10^{3} K, this means that $E_o' - E_o$ is about 100 K. Therefore, the third energy level is well above the low lying doublet, and at low temperatures it will not be thermally populated.

Moreover, it is shown in Appendix B that this situation does not change very much even when tunneling is allowed between c and the other two wells. The $|\psi_2(B_1)\rangle$ state is still an eigenstate of the system. Furthermore, since $|c\rangle$ transforms like A_1, the $|\psi_1(A_1)\rangle$ state does not have its symmetry changed by the admixture of a small amount of the $|c\rangle$ state. Therefore, to a good approximation, one can neglect the presence of the third level, so the wavefunctions and energy levels of the impurity are given by equations (5.25) and (5.27).

These solutions assume a static undistorted host lattice.

If the lattice is distorted either by static strains or time dependent strains (i.e. elastic waves or phonons), the impurity Hamiltonian becomes

$$H' = H + H_s \tag{5.29}$$

where, from equation (2.45), the interaction Hamiltonian is given by

$$H_s = \sum_{ij} (x_{ij} - x_{ij}^o) \frac{\partial V}{\partial x_{ij}} \quad . \tag{5.30}$$

In (5.30), V is the impurity potential which is a function of the coordinates of the neighbouring ions in the lattice, x_{ij} is the j'th coordinate of the i'th neighbour, and x_{ij}^o is its equilibrium value. By expressing the displacements $(x_{ij} - x_{ij}^o)$ in terms of the six strain components $e_{k\ell}$ of the lattice, (5.30) becomes

$$H_s = \sum_{k\ell} \frac{1}{2} \sum_i \left(x_{ik} \frac{\partial V}{\partial x_{i\ell}} + x_{i\ell} \frac{\partial V}{\partial x_{ik}} \right) e_{k\ell} = \sum_{k\ell} h_{k\ell} e_{k\ell} . \tag{5.31}$$

For a given symmetry, it is possible to choose linear combinations of the $e_{k\ell}$'s and of the $h_{k\ell}$'s which transform like the irreducible representations Γ_ν of the symmetry group of the impurity. Then the strain Hamiltonian becomes[46]

$$H_s = \sum_{\mu\nu} h_\mu(\Gamma_\nu) e_\mu(\Gamma_\nu) \tag{5.32}$$

where the index μ accounts for the fact that there may be more than one strain corresponding to a single Γ_ν, or some Γ_ν's may be higher than one dimensional.

From perturbation theory, an elastic wave which causes strains of a given symmetry Γ_ν will produce transitions between

the tunneling states only if the matrix element,

$$\langle\psi_1|H_s|\psi_2\rangle = \langle\psi_1(A_1)|h_\mu(\Gamma_\nu)|\psi_2(B_1)\rangle e_\mu(\Gamma_\nu) \qquad (5.33)$$

is non-zero. Taking the strain outside the matrix element in (5.33) assumes that the strain is spatially constant over the impurity site. This is a good approximation for low temperature, long wavelength phonons. From group theory[97], the only representation which gives a non-vanishing matrix element is $\Gamma_\nu = A_1 \times B_1 = B_1$.

Table 5.2 shows linear combinations of the six strains which transform like irreducible representations of the D_{4h} group of the lattice[82] (with respect to the XYZ axes of Fig. 5.10). The third column gives the elastic constants which relate each of these strains to its corresponding stress, and the last column gives the symmetry of these strains in the C_{2v} group of the impurity site. It can be seen immediately that only the E_g mode, which is related to the C_{44} elastic constant, has a component of B_1 symmetry in the C_{2v} group. Therefore, only elastic waves or phonons of this symmetry should cause transitions and be resonantly scattered. In a sense, this result is obvious. With reference to Fig. 5.10, it can be seen that only an e_{yz} or e_{zx} strain distorts the lattice in such a way as to make the a and b wells inequivalent.

There are other equivalent choices for the X'Y'Z' axes in Fig. 5.10. An alternate choice will result in different labels for the tunneling state symmetries. However, it will still be

TABLE 5.2 Strains in MnF_2 and their symmetries.

Strain	D_{4h} Group	Elastic Constant	C_{2v} Group
e_{zz}	A_{1g}	$\begin{pmatrix} C_{33} & \sqrt{2}\,C_{13} \\ \sqrt{2}\,C_{13} & C_{11}+C_{12} \end{pmatrix}$	A_1
$\frac{1}{\sqrt{2}}(e_{xx}+e_{yy})$	A_{1g}		A_1
$\frac{1}{\sqrt{2}}(e_{xx}-e_{yy})$	B_{1g}	$C_{11}-C_{12}$	B_2
e_{xy}	B_{2g}	C_{66}	A_1
$\begin{pmatrix} e_{yz} \\ e_{zx} \end{pmatrix}$	E_g	$\begin{pmatrix} C_{44} & 0 \\ 0 & C_{44} \end{pmatrix}$	A_2+B_1

found that only an E_g mode will couple the states.

It has been noted in other tunneling systems[98,99] that phonons can cause transitions which should not be allowed by symmetry. For example, transitions between even and odd tunneling states have been observed, which should be forbidden by group theory, since all strains are even. It has been suggested[100] that large internal static strains or electric fields[101] change the tunneling state symmetries, and thus alter the selection rules for phonon scattering. This does not seem to be the case in MnF_2. This may be because the internal strains consist of a random distribution of the six possible types of strain. Since only e_{yz} or e_{zx} strains can distort the impurity site in such a way as to change the tunneling state symmetries, this means that at least two thirds of the impurities are not affected by internal strains.

F. Magnon Conductivity

MnF_2 is a very extensively studied antiferromagnet. The magnetic structure is a simple two sublattice type with the manganese spins on opposite sublattices aligned parallel or antiparallel to the [001] easy axis of magnetization. With reference to Fig. 5.10, if the body centred Mn^{++} ion c has its spin in the +Z direction, then the ions at the corners of the cell have their spins in the -Z direction. However, the nearest neighbours to an ion on one sublattice do not lie on the other sublattice. Manganese ion c has 2 first nearest neighbours in the [001] direction, 8 second nearest neighbours in the [111] directions, and 4 third nearest neighbours in the [100] and [010] directions.

The antiferromagnetic magnon dispersion curves for MnF_2 have been measured by neutron scattering techniques[20,21] and fitted to an expression from spin wave theory[102,103]. This can be expressed in a form similar to equation (2.70) in Chapter II, as

$$\hbar\omega(\vec{q}) = g\mu_B(1+0.073/2S)[(H_{E2}(1+\xi_q)+H_A)^2-H_{E2}^2\gamma_q^2]^{1/2} . \quad (5.34)$$

In this expression, $g = 2.0$ is the g factor, μ_B is the Bohr magneton, $S = 5/2$ is the spin on a manganese ion, and H_A is the effective anisotropy field. The factor $(1 + 0.073/2S)$ accounts for the contribution of higher order terms in the spin Hamiltonian (2.69) to the zero point energy of the system[103]. The function ξ_q is given by

$$\xi_q = \frac{2H_{E1}}{H_{E2}} \sin^2(\frac{cq_z}{2}) - \frac{H_{E3}}{H_{E2}}[\sin^2(\frac{aq_x}{2}) + \sin^2(\frac{aq_y}{2})] \quad (5.35)$$

where $H_{Ei} = 2z_i|J_i|S/g\mu_B$ is the effective exchange field due to the z_i i'th nearest neighbours, with exchange constants J_i. The function γ_q is given by

$$\gamma_q = \cos(\frac{aq_x}{2})\cos(\frac{aq_y}{2})\cos(\frac{cq_z}{2}) \quad (5.36)$$

where a and c are the lattice constants.

By fitting expression (5.34) to the experimental dispersion curves, the parameters were found to be[20,21] $J_1/k_B = 0.32$ K, $J_2/k_B = -1.76$ K, $J_3/k_B = -0.05$ K and $g\mu_B H_A/k_B = 1.06$ K. Therefore, the dominant exchange field is $H_{E2} = 530$ kOe, which comes from the antiferromagnetic exchange interaction with the 8 second nearest neighbours.

The shape of the magnon dispersion curve is shown in Fig. 5.11 for the [001] and [100] directions. For comparison, the phonon dispersion curves, $\omega(k) = v_i k$ are also shown for the longitudinal and transverse modes in the [001] direction. It can be seen that MnF_2 has a large anisotropy gap, $\hbar\omega(0)/k_B = 12.5$ K.

It was pointed out in Chapter II that it is only necessary to know the dispersion relations and the relaxation time for the magnons to be able to calculate their thermal conductivity. Since the relaxation time is unknown, it was assumed to be boundary limited. This at least allows an upper limit for the magnon conductivity to be calculated, using equation (2.75),

$$K_m = \frac{k_B}{6\pi^4} D \sum_j \int \left(\frac{\hbar\omega}{k_B T}\right)^2 \frac{e^{\hbar\omega/k_B T}}{(e^{\hbar\omega/k_B T}-1)^2} \left|\vec{\nabla}_q \omega(\vec{q})\right| \frac{\cos^2\theta_G(\vec{q})}{\sin\theta_G(\vec{q})} d^3q \quad (5.37)$$

where j refers to the two branches of the dispersion curve, which are degenerate with no external magnetic field.

Since the dispersion relations are known, the boundary limited magnon conductivity could be calculated with no approximations. It is clear from Fig. 5.11 that it is a poor approximation to use an average magnon velocity, since the dispersion curves are very nonlinear. It is also important to consider the angular dependence of the dispersion relations in order to include any effects of focusing of the magnons. In fact, the conductivity that was calculated numerically from equations (5.34) and (5.37) was smaller by a factor of about 2.5 than that calculated using the isotropic approximation. This is because the magnons are strongly defocused in the [001] direction.

FIG. 5.11 Magnon dispersion curves for MnF_2. Curves are shown for the [001] and [100] directions. Phonon dispersion curves for the [001] direction are also shown.

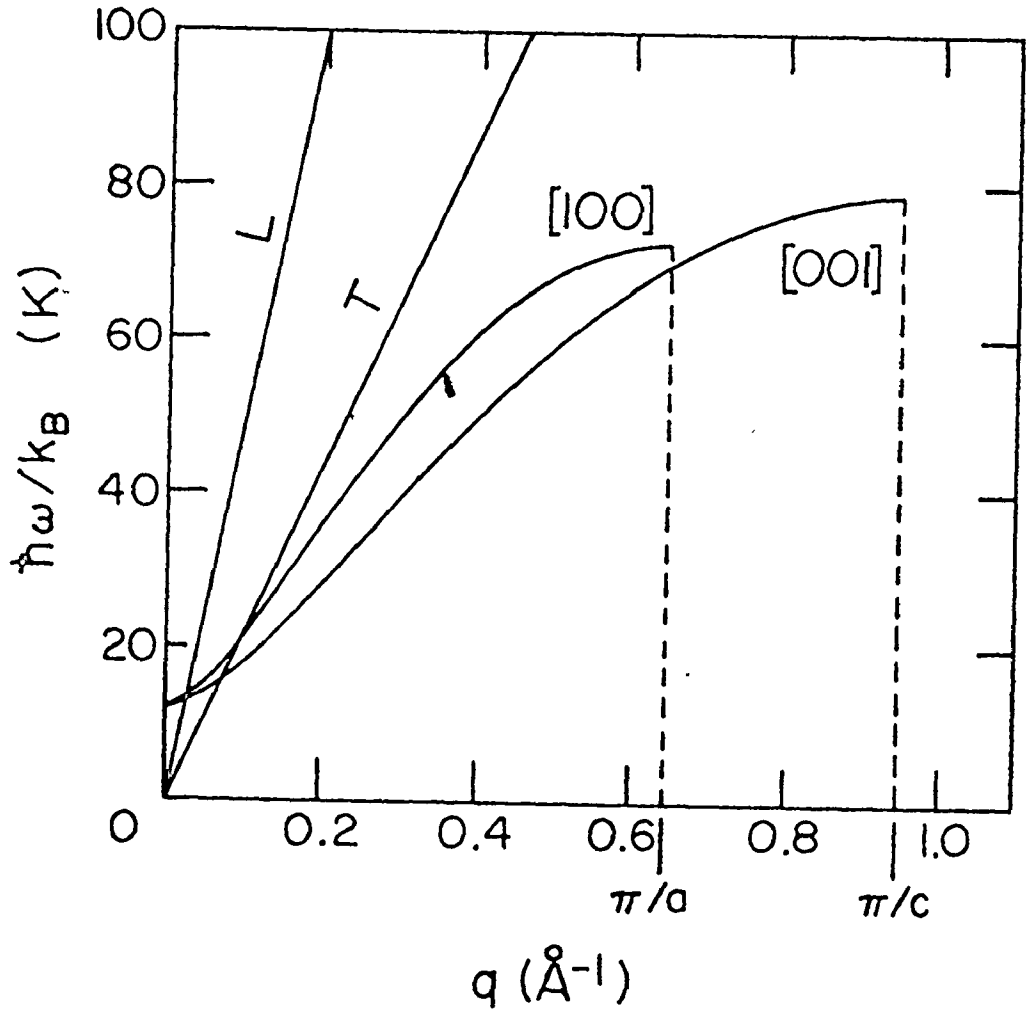
100
80
60
40
20
0
$\hbar\omega/k_B$ (K)
L
T
[100]
[001]
0.2
0.4
0.6
0.8
1.0
π/a
π/c
q (Å^{-1})

The calculated magnon conductivity as a function of temperature is shown in Fig. 5.12(a) in units of the phonon boundary limited conductivity, $K_p = 0.438\ D\ T^3$ watts $cm^{-1}\ K^{-1}$. It can be seen that with no external magnetic field, the magnon conductivity is very small below 2 K. This is because the magnon modes have only a small thermal population at low temperatures due to the large anisotropy gap. At higher temperatures it is possible that the magnons could carry an appreciable fraction of the total heat current.

However, there was no evidence for a magnon contribution in the experimental zero field conductivity results. In several previous experiments[22,104] the fact that the conductivity does not follow a T^3 dependence was attributed to a magnon component which was changing with temperature. This clearly is not the case. The conductivity versus temperature results have been accounted for assuming only a phonon contribution which is modified by a resonant interaction with an impurity.

A better method for finding evidence of magnon heat conduction is to examine the magnetic field dependence of the thermal conductivity. When a magnetic field $\vec{H}$ is applied along the [001] easy axis, the magnon dispersion curve splits into two branches. One branch is raised in energy, and the other lowered by an amount $g\mu_B H$,

$$\hbar\omega(\vec{q},j) = \hbar\omega(\vec{q}) \pm g\mu_B H. \qquad (5.38)$$

The lower branch acquires a larger thermal population which more than compensates for the depopulation of the upper branch, so the

FIG. 5.12(a) Temperature dependence of the boundary limited magnon conductivity. The conductivity is expressed in units of the phonon boundary limited conductivity. The calculation is shown for no magnetic field, and for a field of 60 kOe applied along the [001] direction.

FIG. 5.12(b) Magnetic field dependence of the total boundary limited conductivity. The calculation is for a temperature of 2.0 K.

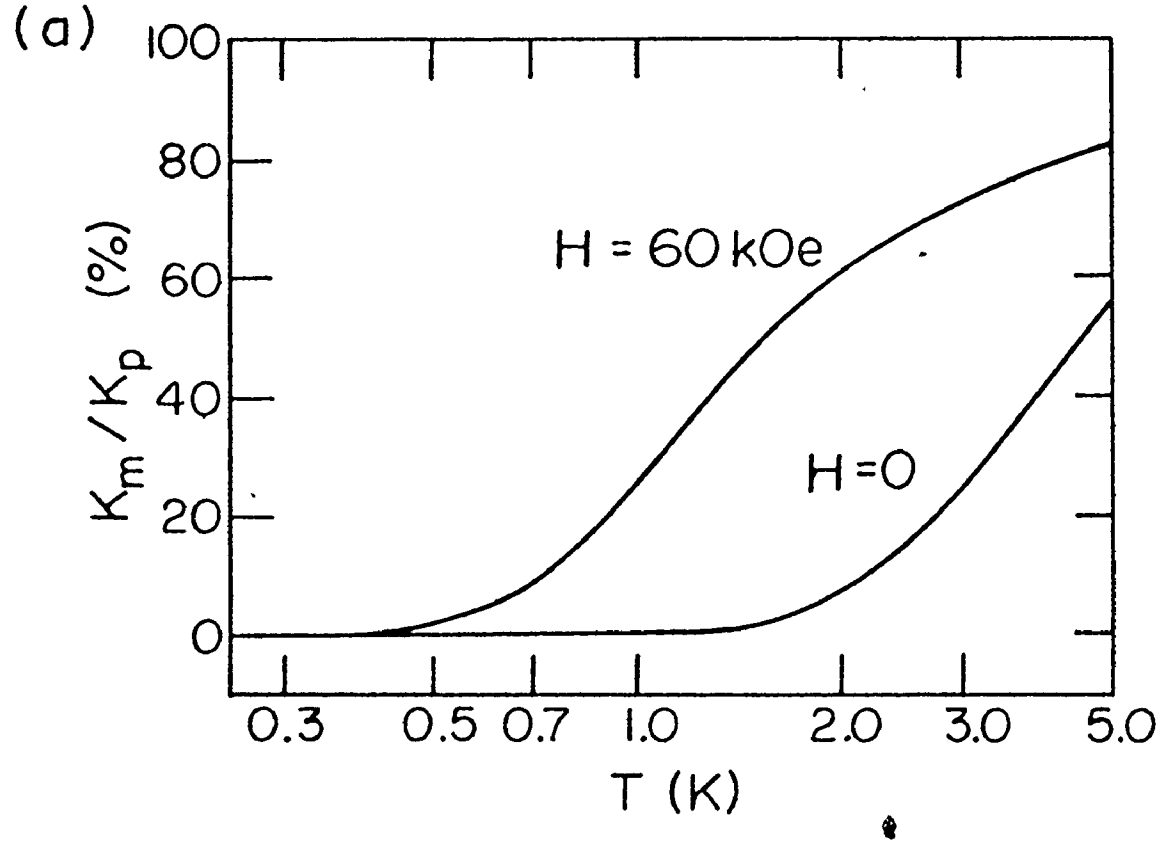
(a)
100
80
60
40
20
0
K_m / K_p (%)
H = 60 kOe
H = 0
0.3
0.5
0.7
1.0
2.0
3.0
5.0
T (K)

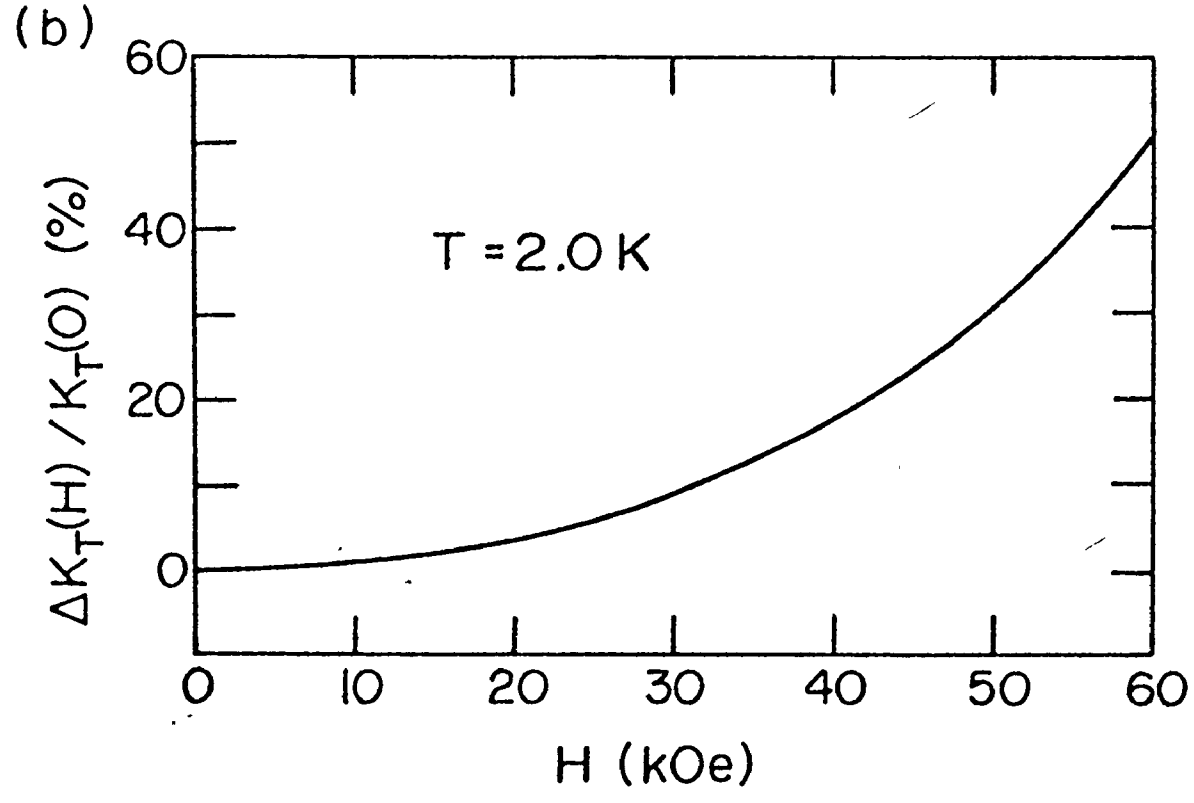
(b)
60
40
20
0
$\Delta K_T(H) / K_T(0)$ (%)
T = 2.0 K
0
10
20
30
40
50
60
H (kOe)

net conductivity increases. This was calculated numerically using equations (5.38), (5.34), and (5.37). The results are shown in Fig. 5.12(a) for H = 60 kOe. It is apparent that with a large applied field, there could be a significant magnon contribution at much lower temperatures.

The predicted magnetic field dependence of the conductivity is illustrated by Fig. 5.12(b). This shows the fractional change in the total conductivity as a function of magnetic field, where the total conductivity was calculated as the sum of the magnon and phonon boundary limits,

$$K_T(H) = K_m(H) + K_p. \qquad (5.39)$$

The largest effect is a 50% increase at 60 kOe for a temperature of 2.0 K. Again, however, the experimental results showed no evidence for a magnon contribution, since the conductivity did not change when $\vec{H}$ was applied along the [001] direction.

Of course, the phonon conductivity is not boundary limited, but is reduced by the resonant interaction with the impurity states. However, this should only increase the relative contribution of the magnons. Therefore, the magnon conductivity must be much smaller than its boundary limited value. The small concentration of OH^- impurities depresses the phonon conductivity because there is a very strong coupling between tunneling states and lattice vibrations. It seems unlikely that the magnons would also interact strongly with the OH^- defects. It is possible that there are other impurities in the crystal which scatter the magnons. If impurities with different spins or exchange interac-

tions substitute for the magnetic Mn^{++} ions, they could produce impurity modes in the magnon spectrum[62]. These could act like resonant magnon scatterers[61] in the same way that the tunneling states scatter the phonons.

While the possibility of impurity scattering cannot be ruled out, there is another possible explanation for the absence of magnon heat transport. This explanation hinges on the question of thermal equilibrium between the magnon and phonon systems. In a thermal conductivity experiment, phonons are generated by the heater and absorbed at the cold end of the sample. This heat can enter or leave the magnon system only via magnon-phonon interactions. Therefore, the heat flux in the magnon system depends on the magnon-phonon coupling, as well as on the magnon conductivity[105].

Thermometers are attached to the sample which measure the difference between the temperatures of the phonon system at either end,

$$\Delta T_p = T_p(L/2) - T_p(-L/2) \qquad (5.40)$$

where L is the sample length. Knowing the heat flux Q supplied by the heater, the effective thermal conductivity is calculated from

$$K_{eff} = - \frac{QL}{\Delta T_p} . \qquad (5.41)$$

Expressing the total conductivity as a sum of magnon and phonon conductivities, as in equation (5.39), implicitly assumes that the temperature of the magnon system is the same as that of the

phonon system. Because thermal transport is inherently a non-equilibrium phenomenon, this is not necessarily the case. Since the magnon temperature cannot be measured directly, the presence of magnon heat conduction can only be inferred from its effect on the phonon temperature. This in turn will depend on the amount of magnon-phonon coupling.

These ideas are developed quantitatively for a simple model in Appendix C. From equation (C.17), the phonon temperature difference can be expressed as

$$\Delta T_p = -\frac{Q}{K_p+K_m} L\left(1 + \frac{K_m}{K_p} \frac{\tanh BL/2}{BL/2}\right) . \qquad (5.42)$$

The parameter B is given by

$$B^2 = \frac{C_m}{\tau_{mp}} \left(\frac{1}{K_p} + \frac{1}{K_m}\right) \qquad (5.43)$$

where K_p and K_m are the intrinsic phonon and magnon conductivities, and C_m is the heat capacity per unit volume of the magnons. Heat enters or leaves the magnon system through magnon-phonon interactions which are described by the relaxation time τ_{mp}. Therefore, the effective conductivity is given by

$$K_{eff} = (K_p + K_m)\left(1 + \frac{K_m}{K_p} \frac{\tanh BL/2}{BL/2}\right)^{-1} . \qquad (5.44)$$

If the magnon-phonon relaxation time is very short, $B \to \infty$, and $K_{eff} \to K_p + K_m$. Therefore, only in this limit is the experimentally measured conductivity the sum of the magnon and phonon conductivities. On the other hand, if the relaxation time is very long, $B \to 0$, so from (5.44), the effective conductivity becomes

$$K_{eff} \rightarrow (K_p+K_m)\left(1 + \frac{K_m}{K_p}\right)^{-1} = K_p .$$

Therefore, in this limit, only the phonon conductivity is measured, even though the intrinsic magnon conductivity may be large.

To illustrate the magnitude of the relaxation time necessary to suppress the magnon conductivity, consider the following example. For an average sample temperature T = 2.0 K, and a magnetic field H = 60 kOe, the boundary limited conductivities are K_p = 3.00, and K_m = 1.83 watts cm^{-1} K^{-1}. This is the case that was shown in Fig. 5.12(b). Since the magnon dispersion curves are known, the specific heat can be calculated from

$$C_m = \frac{k_B}{(2\pi)^3} \sum_j \int \left(\frac{\hbar\omega}{k_B T}\right)^2 \frac{e^{\hbar\omega/k_B T}}{(e^{\hbar\omega/k_B T}-1)^2} \, d^3q \, . \qquad (5.45)$$

Such a calculation has been shown to give good agreement with experimental results[22,34]. Using equations (5.45), (5.38) and (5.34), the magnon specific heat at 2.0 K and 60 kOe was found to be 7.83×10^{-5} joules K^{-1} cm^{-3}.

These parameters were used to calculate the effective conductivity as a function of the magnon-phonon relaxation time. The results are shown in Fig. 5.13. It can be seen that if τ_{mp} is less than about 10^{-6} sec, the effective conductivity is essentially the sum of the magnon and phonon conductivities. However, if τ_{mp} is about 10^{-4} sec, the magnon contribution to K_{eff} is greatly reduced. This is the relaxation time that was used to calculate the temperature profiles shown in Fig. C.1. Furthermore,

FIG. 5.13 Dependence of the effective boundary limited conductivity on the magnon-phonon relaxation time. The calculation is for a temperature of 2.0 K, and a magnetic field of 60 kOe applied along the [001] direction. The limiting values for long and short relaxation times are also shown.

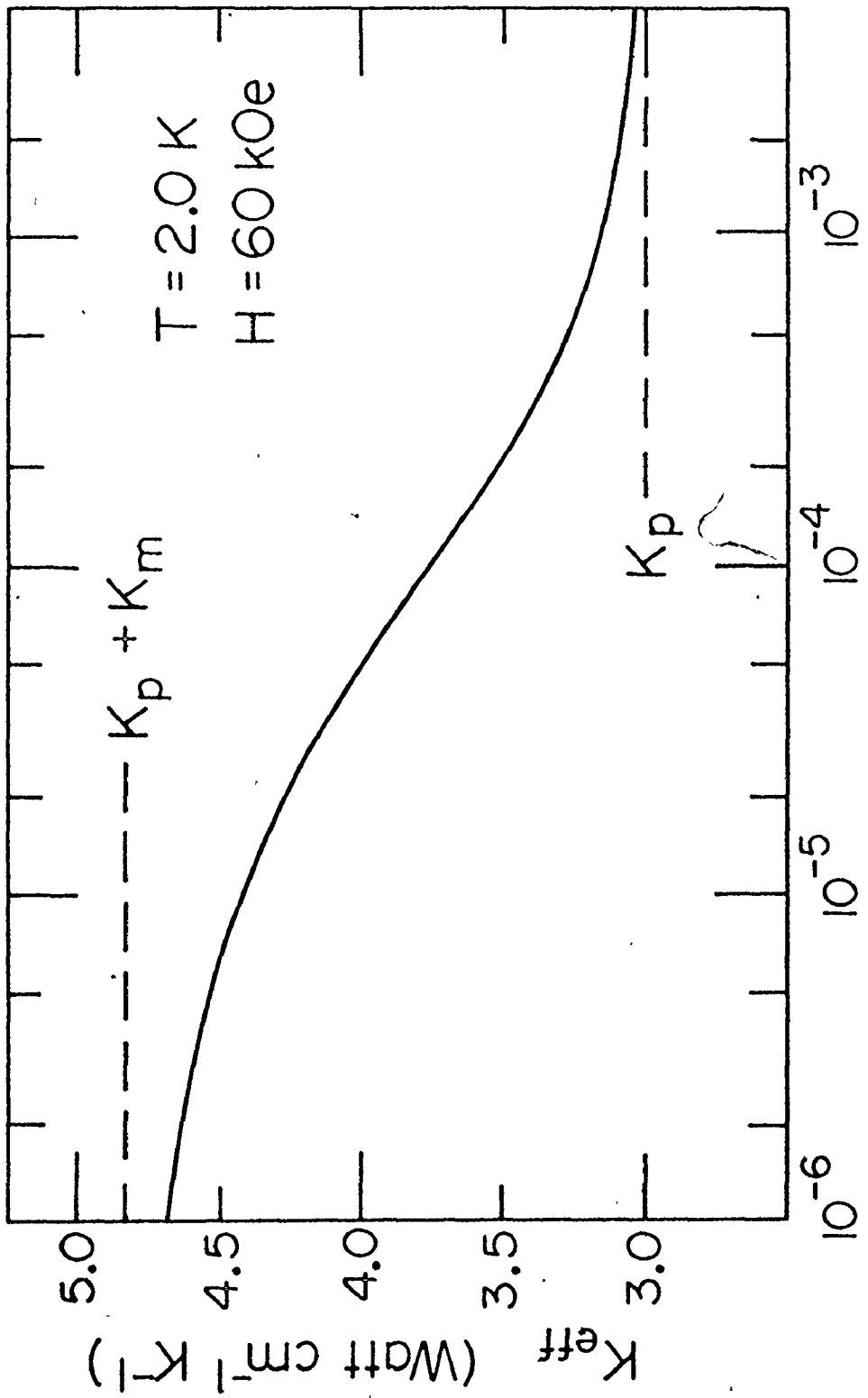
T = 2.0 K
H = 60 kOe
$K_p + K_m$
K_p
K_{eff} (Watt cm^{-1} K^{-1})
5.0
4.5
4.0
3.5
3.0
10^{-6}
10^{-5}
10^{-4}
10^{-3}
τ_{mp} (sec)

a relaxation time of 5×10^{-3} sec produces a K_{eff} that differs from K_p by less than 1%. Therefore, even though K_m is 60% of K_p, the magnon contribution could not be measured experimentally.

The magnon-phonon interaction is strongest in the region where the dispersion curves of the two excitations cross, since at this point energy and wave vector can be conserved in a one magnon-one phonon process. The interaction produces a gap in the dispersion curves at the crossover, the size of which is determined by the magnetoelastic coupling constant b[65]. This has been measured for MnF_2 by ultrasonic techniques, and found to be 3.0×10^6 ergs/cm^3 [60]. It is found that in the [001] direction, only the transverse phonons couple to the magnons. The crossover point is at $\hbar\omega/k_B$ = 15 K, as shown in Fig. 5.11. The gap in the spectrum at this point has been calculated to be only about 0.1 K[106], so only a few modes are involved in this process. Therefore, it is not surprising that there was no evidence for this resonant magnon-phonon interaction in the experimental results.

Higher order interactions, such as one phonon-two magnon processes are not restricted to modes of the same frequency and wave vector. Therefore, these are more important in establishing equilibrium between the magnon and phonon temperatures[63]. A theoretical treatment of these interactions has been developed for antiferromagnets by Upadhyaya and Sinha[69]. They found that the magnon-phonon relaxation time is proportional to T^{-5},

and they estimated that τ_{mp} is of the order of 10^{-7} to 10^{-8} sec for MnF_2 at 10 K. Extrapolating this estimate to 2 K gives a τ_{mp} of about 3×10^{-4} to 3×10^{-5} sec. However, since they neglected the effects of the anisotropy gap in the magnon spectrum, their results are probably not valid below $\hbar\omega(0)/k_B = 12.5$ K. The magnon-phonon relaxation time is probably longer than this estimate would indicate, because at temperatures below the gap, there are few thermal magnons available to participate in the interaction.

This has been verified by calculations of the magnon lifetimes from antiferromagnetic resonance (AFMR) measurements. Kotthaus and Jaccarino[107] measured the temperature dependent part of the AFMR linewidth of MnF_2 between 5 and 40 K for a magnetic field of 83 kOe. These results have recently been analyzed by White et al.[108]. They found that the thermally induced relaxation rate is proportional to T^4, and that $\tau_{Th}^{-1} = 5\times10^5$ sec^{-1} at 5 K. Therefore, extrapolating to 2 K, τ_{Th}^{-1} is found to be about 10^4 sec^{-1}. Since relaxation rates are additive, this is the sum of the relaxations due to magnon-phonon interactions, and magnon-magnon processes, i.e. $\tau_{Th}^{-1} = \tau_{mp}^{-1} + \tau_{mm}^{-1}$. However, it was also shown[108] that the relaxation rate can be quantitatively accounted for using only magnon-magnon normal processes. Therefore, any contribution by magnon-phonon relaxation must be smaller, so $\tau_{mp}^{-1} << \tau_{Th}^{-1}$. This indicates that for MnF_2 at 2 K in a field of 83 kOe, $\tau_{mp} >> 10^{-4}$ sec. Therefore, it is possible that the magnon-phonon equilibrium time is long enough

to suppress any magnon contribution to the thermal conductivity.

It must be emphasized that this explanation can be applied to any magnetic material. This may explain why experimental evidence for heat conduction by magnons has been found in only a few of the materials that have been investigated. As pointed out in the introduction, the most convincing case of magnon conductivity is for the ferrimagnet yttrium iron garnet (YIG)[2-5]. The magnon-phonon relaxation time for YIG has been measured directly using AFMR techniques[109]. It was found that τ_{mp} is about 10^{-6} sec at 2 K, which is much less than that for MnF_2. Therefore, it may be that the equilibrium time for YIG is short enough to allow the magnon conductivity to be measured.

G. Tunneling States in a Magnetic Field

When a magnetic field was applied at an angle of 25° to the [001] direction, large changes in the thermal conductivity were produced. It was suggested in Chapter IV that this could be accounted for by assuming that the resonant frequency for phonon scattering increases with magnetic field. The conductivity at 60 kOe was calculated using the same expressions (5.13) and (5.3), and the same parameters that were used to calculate the zero field conductivity, plus one additional adjustable parameter. It was assumed that the resonant frequency ω_o, which was $\hbar\omega_o/k_B = 4.0$ K with no applied field, increased by an amount $\delta\omega_o$ in a field of 60 kOe applied at an angle of 25°. The best fit to the relative change in conductivity, which is shown by the solid

line in Fig. 5.14 was calculated using $\hbar\delta\omega_o/k_B = 0.66$ K. While the fit is certainly not perfect, it must be emphasized that this employs only one independently adjustable parameter. The fact that the fitted curve follows the general trend of the data is a clear indication that the change in conductivity is caused by a shift in the resonant frequency.

Earlier in this chapter, it was postulated that the resonant frequency corresponds to the energy separation between two tunneling states of the OH^- molecule. At first, it may seem unlikely that this splitting should change with magnetic field, since the OH^- molecule is nonmagnetic. However, there is at least one mechanism that could cause this. The tunneling states are affected by static strains in the crystal, and these will be produced by a magnetic field because of the magnetoelastic interaction.

In Chapter II, an expression for the energy of a uniaxial antiferromagnet was given by equation (2.78), in terms of the strains and sublattice magnetizations. By minimizing this energy with respect to each strain, the static strains are found to be

$$e_{zx} = - \frac{b}{C_{44}} \frac{m_{1x} - m_{2x}}{m_s} \qquad (5.46)$$

and a similar expression for e_{yz}. In (5.46), b is the magnetoelastic coupling constant, m_{1x} and m_{2x} are the x components of magnetization for sublattices 1 and 2 respectively, and $m_s = |\vec{m}_1| = |\vec{m}_2|$ is the magnitude of the sublattice magnetization.

FIG. 5.14 Calculated relative change in the thermal conductivity at 60 kOe for a field at 25° to the [001] direction. The solid line is the calculated fit to the experimental results.

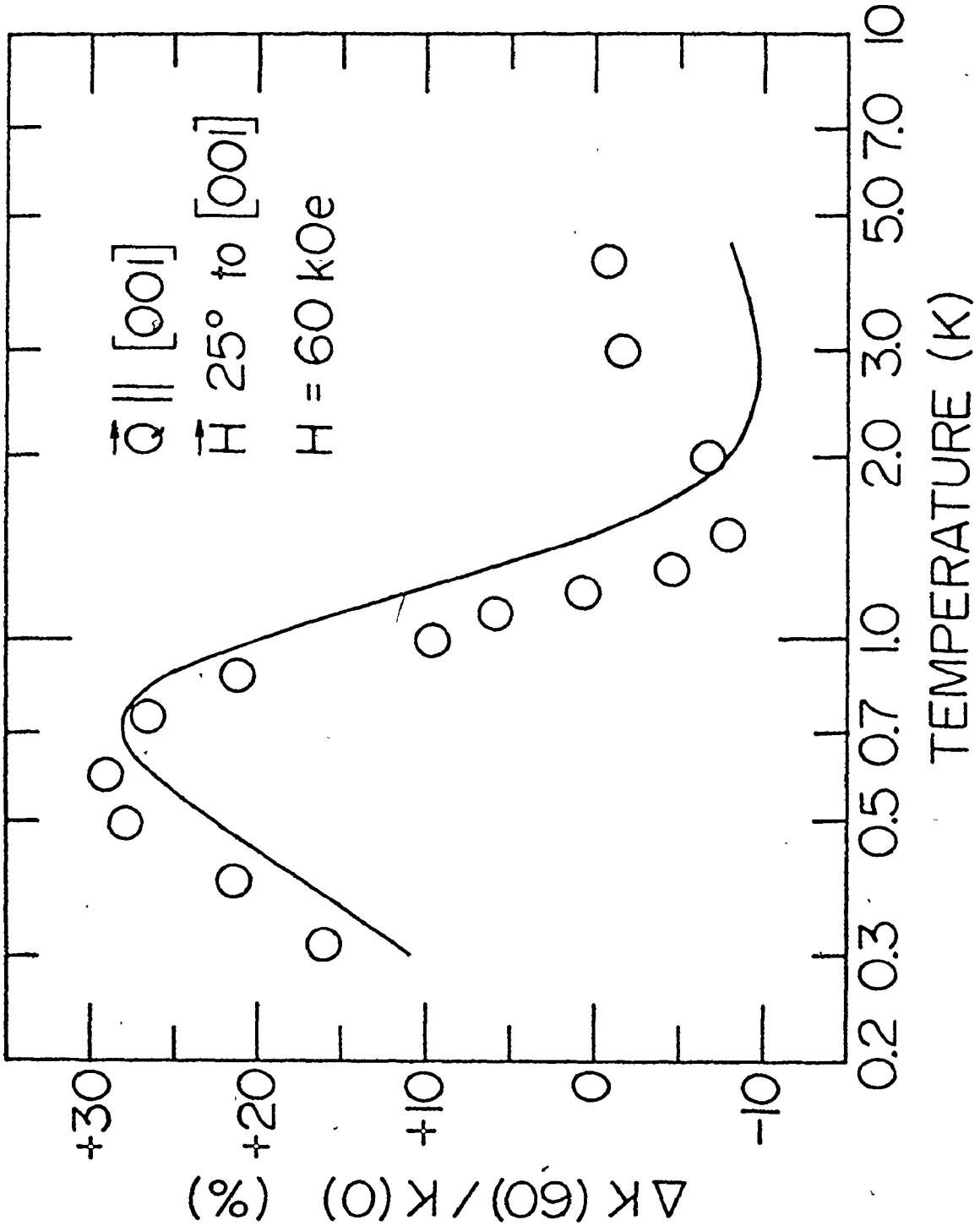
$\vec{Q} \parallel [001]$
$\vec{H}$ 25° to [001]
H = 60 kOe
+30
+20
+10
0
-10
$\Delta K\,(60)\,/\,K\,(0)$ (%)
0.2 0.3 0.5 0.7 1.0 2.0 3.0 5.0 7.0 10
TEMPERATURE (K)

At low temperatures, $\vec{m}_1$ is aligned along the +z direction, and $\vec{m}_2$ along the -z direction, so m_{1x} and m_{2x} are zero, and there is no static strain. When a magnetic field is applied parallel to the [001] easy axis, the magnetic moments remain aligned up to the critical field H_c, at which point they abruptly flop into a configuration perpendicular to the field. For MnF_2, $H_c = (2H_E H_A)^{1/2}$ is 93 kOe[60].

However, if the field is applied at an angle ψ to the easy axis, the orientations of the sublattice magnetizations change continuously as the field is increased[110]. This is analyzed in Appendix D. With refernece to Fig. D.1, the orientations are given by the angles θ and t. From equations (D.8) and (D.4), these can be expressed as

$$\tan 2\theta = \frac{\sin 2\psi}{(H_c/H)^2 - \cos 2\psi}$$

and (5.47)

$$\sin t = \frac{H \sin(\psi+\theta)}{2H_E}$$

where H_E = 530 kOe is the exchange field for MnF_2.

Suppose the field $\vec{H}$ is applied in the xz plane. From Fig. D.1, the x components of magnetization are

$$m_{1x} = -m_s \sin(\theta - t)$$

and (5.48)

$$m_{2x} = m_s \sin(\theta + t) \ .$$

These produce a static strain in the crystal, which from (5.46) can be expressed as

$$e_{zx} = \frac{2b}{C_{44}} \sin\theta\cos t. \qquad (5.49)$$

This expression, along with (5.47), shows how the strain depends on magnetic field, and on the angle at which it is applied.

Now it is necessary to calculate how the tunnel splitting changes with strain. With reference to Fig. 5.10, a strain component $e_{z'x'}$ will be produced at an impurity site with a magnitude

$$e_{z'x'} = \frac{e_{zx}}{\sqrt{2}} = \frac{\sqrt{2}\, b}{C_{44}} \sin\theta\cos t. \qquad (5.50)$$

As noted in section E of this chapter, since $e_{z'x'}$ transforms like the B_1 irreducible representation, this strain will produce off-diagonal matrix elements between the tunneling states. The new impurity Hamiltonian is $H' = H + H_s$, where the strain interaction is

$$H_s = h(B_1)e_{z'x'}(B_1) \qquad (5.51)$$

and

$$h(B_1) = \frac{1}{2} \sum_i \left(x_i' \frac{\partial V}{\partial z_i'} + z_i' \frac{\partial V}{\partial x_i'} \right).$$

The off-diagonal matrix elements are

$$\langle \psi_1 | H' | \psi_2 \rangle = \langle \psi_1 | H_s | \psi_2 \rangle = We_{z'x'} \qquad (5.52)$$

where $W = \langle \psi_1(A_1) | h(B_1) | \psi_2(B_1) \rangle$ is the energy shift per unit strain. By group theory, the diagonal matrix elements will be unchanged by the interaction, so from equation (5.27), these are

$$\langle \psi_1 | H' | \psi_1 \rangle = \langle \psi_1 | H | \psi_1 \rangle = -\Delta/2$$

and (5.53)

$$\langle \psi_2 | H' | \psi_2 \rangle = \langle \psi_2 | H | \psi_2 \rangle = \Delta/2$$

where the energy levels are measured with respect to E_o and Δ is the tunnel splitting with no static strain.

Therefore, the secular equation for the new energy levels E', in terms of the basis states $|\psi_1\rangle$ and $|\psi_2\rangle$ is

$$\begin{vmatrix} -\Delta/2 - E' & We_{z'x'} \\ We_{z'x'} & \Delta/2 - E' \end{vmatrix} = 0 \qquad (5.54)$$

which has the solutions

$$E' = \pm \frac{\Delta}{2} (1 + X^2)^{1/2} \qquad (5.55)$$

where $X = 2We_{z'x'}/\Delta$. These energy levels are shown in Fig. 5.15. It can be seen that the tunnel splitting,

$$\Delta' = \Delta(1 + X^2)^{1/2} \qquad (5.56)$$

does increase with strain. The splitting required to produce a resonant frequency $\hbar\omega_o/k_B = 4.66$ K is also shown in the diagram.

This analysis of the tunneling states in the presence of a static strain is similar to that performed by Alderman and Cotts[111] for the tunneling system KCl:Li. Their calculated splittings as a function of applied stress were found to be in good agreement with the experimental measurements. The energy shift parameter W that they calculated by fitting the experimental results was found to be the same[26] as that calculated from ultrasonic measurements[112]. From the C_{44} elastic constant measurements, W for OH^- in MnF_2 was estimated earlier in this chapter to be 8.0×10^3 K per unit strain.

FIG. 5.15 Dependence of the tunneling state energy levels on static strain. The splitting for a field of 60 kOe, applied at 25° to the [001] direction is also shown.

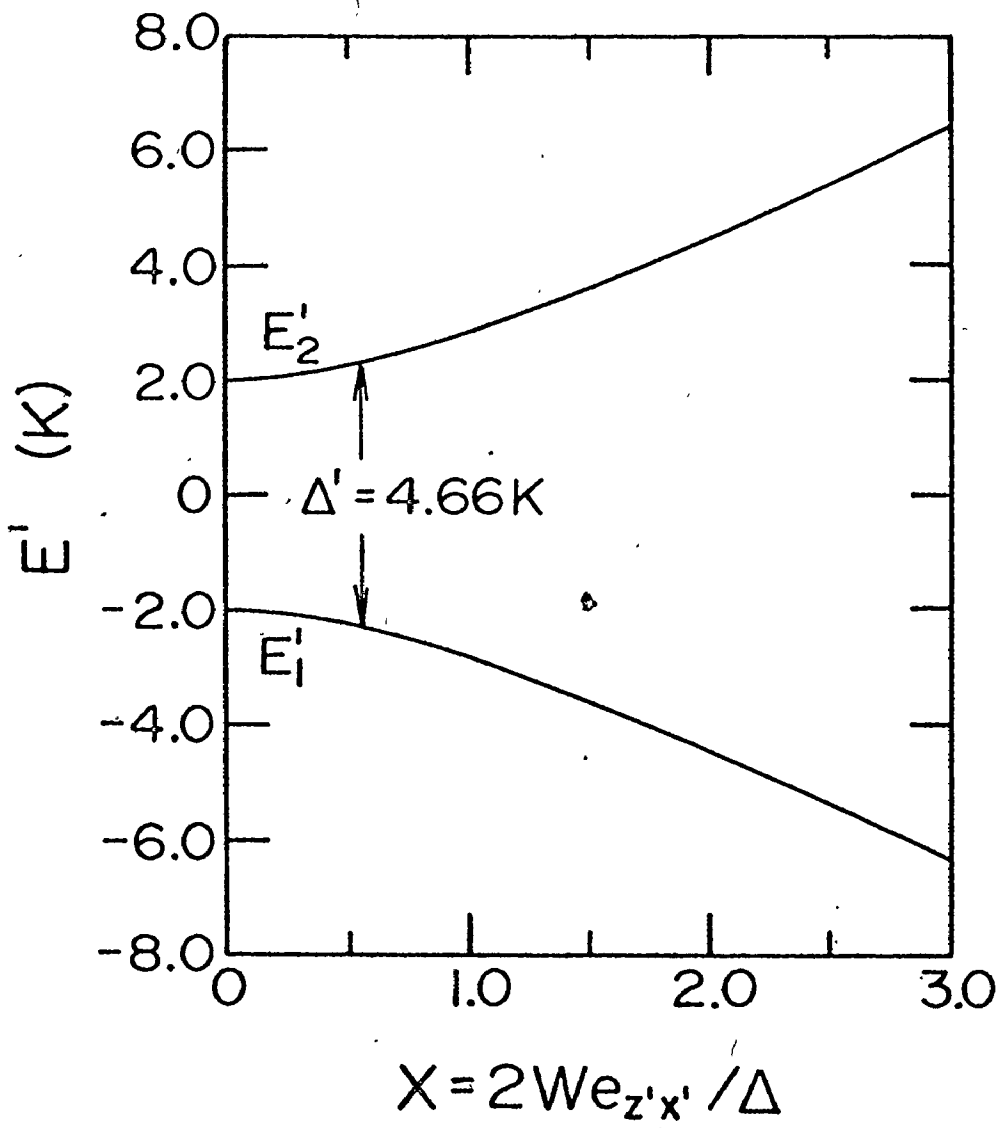
8.0
6.0
4.0
2.0
0
-2.0
-4.0
-6.0
-8.0
E (K)
E_2'
$\Delta' = 4.66K$
E_1'
0
1.0
2.0
3.0
$X = 2We_{z'x'}/\Delta$

Combining equations (5.56) and (5.50), the tunnel splitting in the presence of a field H applied at an angle ψ can be expressed as

$$\Delta'(H,\psi) = \Delta[1 + G^2\sin^2\theta(H,\psi)\cos^2 t(H,\psi)]^{1/2} \qquad (5.57)$$

where $G = 2\sqrt{2}\ Wb/\Delta C_{44}$. It can be seen that this expression has the correct angular dependence. If $\psi = 0$, then from (5.47) $\theta = 0$, so the tunnel splitting remains constant, and the conductivity does not change as the field is increased.

If $\psi = 25°$, then it can be calculated from (5.47) that $\theta = 12°$, and $t = 2°$ for a field of 60 kOe. Using these values in (5.57), it was found that G must have a value of 2.86 to produce a tunnel splitting of 4.66 K at 60 kOe. With this value for G, the resonant frequency for any field H can be calculated from equations (5.47) and (5.57). Using these, along with the previous thermal conductivity expressions and parameters, the conductivity was calculated as a function of magnetic field. The results are shown by the solid lines in Fig. 5.16. It can be seen that this model predicts the correct magnetic field dependence for both increases and decreases in conductivity. It must be emphasized that these calculations use no independently adjustable parameters.

Finally, it should be noted that it is possible to calculate a value for G from other measurements of the quantities involved. With $W = 8.0\times10^3$ K, $b = 3.0\times10^6$ ergs/cm^3 (60), $\Delta = 4.0$ K, and $C_{44} = 3.202\times10^{11}$ dynes/cm^2 (33), G was found to

FIG. 5.16 Calculated magnetic field dependence of the thermal conductivity for fields at 25° to the [001] direction. The solid lines show the calculated relative change in the conductivity.

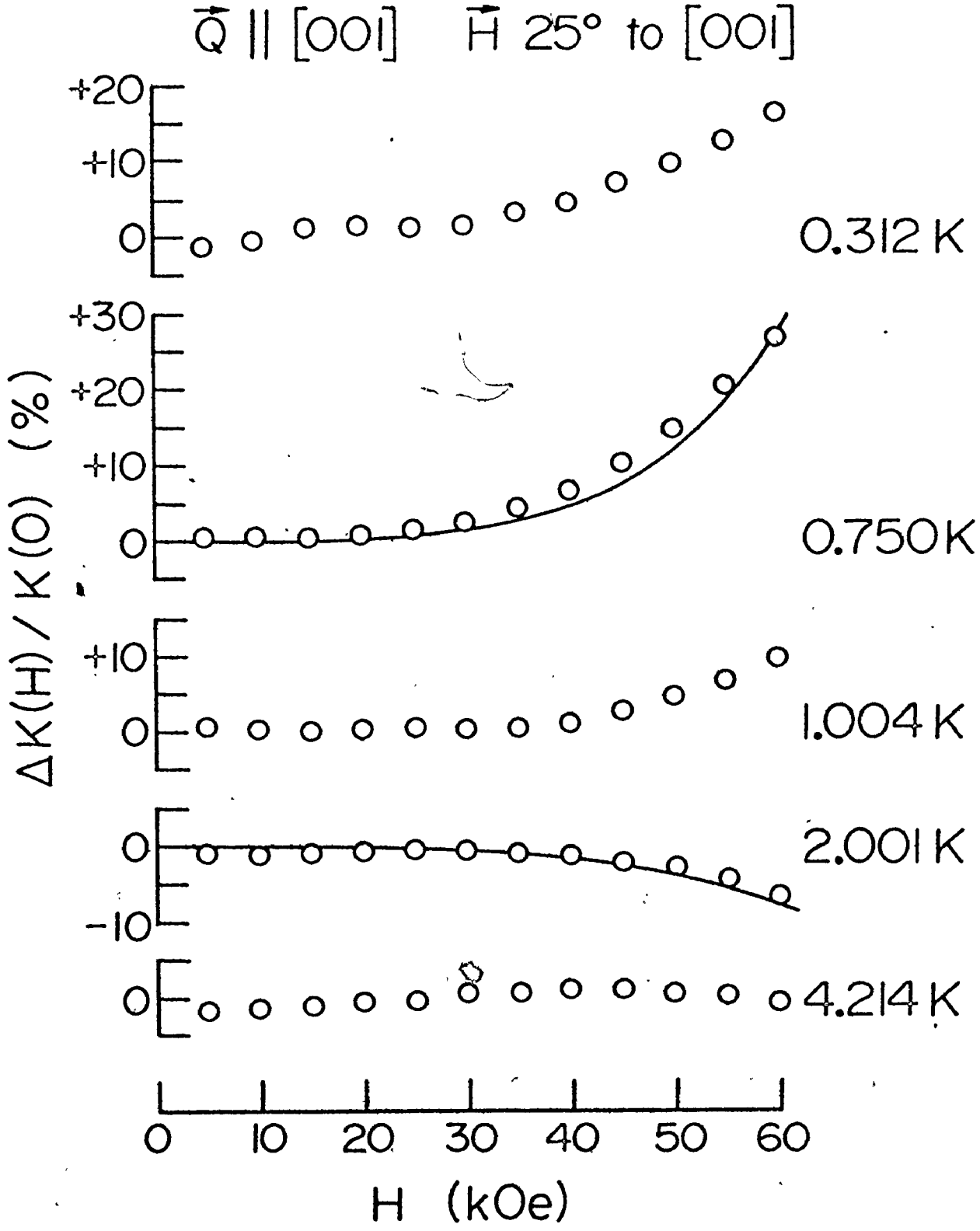
Q || [001] H 25° to [001]
+20
+10
0
0.312 K
+30
+20
+10
0
0.750 K
+10
0
1.004 K
0
-10
2.001 K
0
4.214 K
ΔK(H) / K(0) (%)
0
10
20
30
40
50
60
H (kOe)

be 0.053. This is a factor of about 50 smaller than the value needed to explain the experimental results. Nevertheless, this model should not be discarded, since it does predict the correct dependence on angle and on magnetic field. Since the calculation of the energy shift per unit strain was based on a rather crude estimate of the impurity concentration, the value of W may be in error. If W is in fact larger, this would produce a larger value for G.

Another possible explanation for this discrepancy is that the magnetoelastic coupling may be different around an OH^- impurity than it is in the bulk crystal. Magnetoelastic interactions[64] occur because strains in the crystal alter the distance between magnetic Mn^{++} ions, which in turn affects the exchange and magnetic dipole interactions between them. Strains also alter the crystal field around each Mn^{++} ion which affects the spin of the ion via residual spin-orbit coupling. All these effects will be different for Mn^{++} ions in the vicinity of an OH^- substitutional impurity. Since only the local strain around the impurity enters into the calculation, if the local coupling parameter b were larger than the bulk value, this would also result in a larger value for G.

CHAPTER VI

CONCLUSIONS AND RECOMMENDATIONS

Since its magnon dispersion curves are well known, it was possible to calculate exactly the boundary limited magnon conductivity of MnF_2. The calculation demonstrated that focusing effects can be important in heat transport by magnons, as they are in the phonon case[32]. It was predicted that the magnon component could be recognized by an increase in the total conductivity when a magnetic field was applied parallel to the [001] easy axis of magnetization. The maximum effect was calculated to be a 50% increase in a field of 60 kOe, at a temperature of 2.0 K.

The experimental results, however, showed no change in conductivity with magnetic field for any temperature in the range 0.3 to 4.2 K. This could indicate that the magnon conductivity was reduced from its boundary limit, possibly due to scattering by magnetic impurities. However, a more general explanation for the absence of magnon conductivity was postulated. It was demonstrated that the experimentally measured conductivity depends on the amount of coupling between the magnon and phonon systems. If this coupling is very small, only the phonon conductivity will be measured, even though the intrinsic magnon conductivity may be large. This fact has not been recognized in previous treatments

of the subject.

The available information on magnon lifetimes indicated that the magnon-phonon relaxation time for MnF_2 could be long enough to suppress any thermal transport in the magnon system. Furthermore, since this explanation could be applied to other magnetic materials, it might explain why magnon conductivity has been such an elusive phenomenon.

This hypothesis could be verified by direct measurement of the time required for the magnon and phonon temperatures to come to equilibrium. It has been observed in specific heat experiments that long relaxation times can be required for weakly interacting systems to reach equilibrium with the phonon temperature. Relaxation times shorter than a few seconds would not be noticed in a standard specific heat experiment. However, by using very short heater pulses, Seward et al.[113] were able to measure relaxation times of the order of 10^{-2} sec for the system NaCl:CN. Such an experiment for MnF_2, or another magnetic material, could conceivably measure the magnon-phonon relaxation time directly.

Despite the lack of a magnon component, thermal transport in MnF_2 exhibited several interesting features. With heat flow along the [001] direction, the thermal conductivity as a function of temperature showed a dip centred at 1.0 K. The shape of the dip was characteristic of a resonant interaction of the phonons with an impurity. This impurity has previously been shown[24] to be OH^- which occurs even in nominally pure MnF_2.

The shape of the heat pulse signal for a [001] oriented

sample indicated that the transverse pulse was highly attenuated. The dependence on path length of the heat pulse signals for [110] oriented samples indicated that the fast transverse pulse in this direction was also attenuated. In both cases, the attenuated pulses were associated with phonons of E_g symmetry.

These results were analyzed using a method that exploits the complimentary nature of thermal conductivity and heat pulse measurements. This method required a knowledge of the phonon phase and group velocities for MnF_2. These were calculated numerically using measured values of the elastic constants[33]. The calculations showed that the phonon velocities are very anisotropic in the (001) plane of MnF_2.

Since the heat pulse results suggested that only E_g phonons were resonantly scattered, this assumption was included in the theoretical expression that was fitted to the thermal conductivity results. A satisfactory fit was achieved using an expression due to Walton[42,43] for the phonon resonant relaxation rate. From the fit, the resonant frequency was found to be 5.2×10^{11} sec^{-1} which corresponds to a level separation for the impurity states of 4.0 K, or 2.8 cm^{-1}. It was found that it was necessary to include phonon focusing effects in calculating the boundary limit for the conductivity. Moreover, by eliminating the usual isotropic approximation, it was possible to calculate the scattering parameters for the E_g mode, rather than an average over all phonon modes.

A computer model was constructed which simulated the

ballistic heat pulse signals. The model correctly predicted the presence of an extra transverse pulse for the [110] oriented samples, and showed that this pulse was due to the large elastic anisotropy in the (001) plane. Since it included focusing effects, the model also predicted the correct relative intensities of the heat pulses, with the exception of the pulses associated with the E_g phonons. The attenuation of these pulses was included by using the scattering parameters calculated from the thermal conductivity fit, and assuming a perfect-coupling black-body frequency distribution for the phonons in the heat pulses. With the attenuation included, the calculated pulse signals were in good agreement with the experimental results.

This method of analysis is preferable to fitting directly to the heat pulse results. The phonon frequency distribution for a thermal conductivity experiment is well established, whereas the distribution for a heat pulse experiment depends on the assumptions made about the thermal coupling between the heater and sample.

The thermal conductivity and heat pulse results were shown to be consistent with previously unexplained results for the C_{44} elastic constant of MnF_2. It was demonstrated that the anomalous low temperature decrease in C_{44} noted by Melcher[33] could be accounted for by the reduction in the velocity of the E_g phonons caused by their resonant interaction with the OH^- impurities. This was calculated using Walton's expression[41-43] for the dispersion relations of the coupled phonon-impurity modes. The resulting

expression for C_{44} as a function of temperature was fitted to Melcher's data with fairly good agreement. By assuming that the elastic constant samples contained the same impurity concentration as the thermal conductivity sample, it was possible to estimate a concentration for the OH^- impurities of 8×10^{16} cm^{-3}. Using this value, it was calculated from the elastic constant fit that the elastic dipole moment of the OH^- impurity was 3.4×10^{-24} cm^3.

It was pointed out that the OH^- molecule in MnF_2 exhibits a level separation of the order of a few cm^{-1}, an elastic dipole moment of the order of 10^{-24} cm^3, and a large reduction in the thermal conductivity for a small impurity concentration. Since all these properties are very similar to those found for tunneling states of molecular impurities in alkali halide hosts[26], it was postulated that the OH^- molecule in MnF_2 also possesses tunneling states. To support this hypothesis, it was demonstrated that at least one model for the tunneling states could be constructed which was consistent with the experimental results. Using the method of Gomez et al.[46], the low lying states of the model system were shown to form a tunnel-split doublet. Furthermore, the symmetries of the states were such that only E_g phonons would cause transitions between them, and thus be resonantly scattered.

When a magnetic field was applied at an angle of 25° to the [001] easy axis, the thermal conductivity increased for temperatures below 1.2 K, and decreased for higher temperatures. This was shown to be caused by an increase in the resonant frequency of the OH^- impurity. This is not inconsistent with a tunneling

model since an off-axis magnetic field creates static strains in the crystal, via the magnetoelastic interaction, which increase the splitting between the tunneling states. It was shown that this explanation predicted the correct qualitative dependence of the thermal conductivity on magnetic field, and on the angle at which it was applied. However, there was quantitative disagreement between the calculated and measured magnitudes of the effect. This discrepancy might be explained by a larger local magnetoelastic coupling in the vicinity of an impurity site.

The tunneling nature of the OH^- impurity states in MnF_2 could be confirmed or disproven by further experimental investigation. Specific heat experiments have been important in the investigation of tunneling systems such as OH^- in KCl[114]. A two level system with a splitting of 4.0 K for the OH^- impurity in MnF_2 would contribute a Schottky anomaly to the specific heat, peaked at 1.7 K. Unfortunately, the specific heat of MnF_2 at this temperature is dominated by the large heat capacity of the manganese nuclear spin system[34]. Impurity concentrations much larger than 10^{17} cm^{-3} would be required to produce a measurable contribution to the specific heat.

Infrared absorption measurements have been used to study OH^- impurity modes in alkali halides[96]. However, Gustafson[23] reported that there was no evidence for OH^- modes in the infrared absorption of MnF_2. This may be because the naturally occurring OH^- concentration is too small to produce a measurable absorption.

With higher concentrations, these experiments could prove useful.

Another possible experiment, which has been used for other tunneling systems[84], is the measurement of the thermal conductivity in a large static electric field. Since the OH^- molecule has a large electric dipole moment[114], an electric field would alter the tunnel splitting, causing a change in the resonant frequency for phonon scattering. This in turn would produce a variation in the conductivity as a function of electric field. If the existence of OH^- tunneling states in MnF_2 is confirmed, this would be one of the very few examples of a tunneling system in a host crystal other than an alkali halide.

In summary, it can be said that, even though MnF_2 is a very extensively studied material, its thermal transport properties include several interesting features that are worthy of further investigation.

APPENDIX A

PHONON VELOCITIES

At low temperatures, the phase and group velocities of acoustic phonons can be calculated from elastic continuum theory[35]. the results of this theory can be summarized as follows. Hooke's law relating the stress and strain tensors can be expressed as

$$\sigma_{ij} = \sum_{k\ell} C_{ijk\ell}\,\varepsilon_{k\ell} \qquad \text{(A.1)}$$

where σ_{ij} is the stress, $\varepsilon_{k\ell}$ is the strain, $C_{ijk\ell}$ is an elastic constant, and $i,j,k,\ell = 1,2,3$. The strain components are related to the particle displacements $\vec{u}$ by

$$\varepsilon_{k\ell} = \frac{1}{2}\left(\frac{\partial u_k}{\partial x_\ell} + \frac{\partial u_\ell}{\partial x_k}\right) \qquad \text{(A.2)}$$

where $\vec{u} = \sum_i u_i \hat{i}_i$, and $\hat{i}_i$ is a unit vector along the Cartesian crystal axis x_i. The equations of motion for the stress components and particle displacements are

$$\sum_i \frac{\partial \sigma_{ij}}{\partial x_i} = \rho \frac{\partial^2 u_j}{\partial t^2} \qquad \text{(A.3)}$$

where ρ is the density of the medium. Substituting (A.1) and (A.2) into (A.3) yields

$$\frac{1}{2} \sum_{ik\ell} C_{ijk\ell} \frac{\partial}{\partial x_i}\left(\frac{\partial u_k}{\partial x_\ell} + \frac{\partial u_\ell}{\partial x_k}\right) = \rho \frac{\partial^2 u_j}{\partial t^2}\,. \qquad \text{(A.4)}$$

The solution to these equations is assumed to be a plane

wave with a wave vector $\vec{k}$ which has direction cosines ℓ_1, ℓ_2, and ℓ_3 with respect to the crystal axes. Therefore,

$$\vec{u} = \hat{e}\, e^{ik(\ell_1 x_1 + \ell_2 x_2 + \ell_3 x_3 - vt)} \tag{A.5}$$

where $\hat{e}$ is the unit polarization vector, and $v = \omega/k$ is the phase velocity. Substituting (A.5) into (A.4) gives

$$\frac{1}{2} \sum_{ik\ell} \ell_i \ell_\ell (C_{ijk\ell} + C_{ij\ell k}) e_k = \rho v^2 e_j . \tag{A.6}$$

Letting $\Gamma_{jk} = \frac{1}{2} \sum_{i\ell} \ell_i \ell_\ell (C_{ijk\ell} + C_{ij\ell k})$, this can be written as

$$\sum_k (\Gamma_{jk} - \delta_{jk}\rho v^2) e_k = 0. \tag{A.7}$$

These equations will have non-trivial solutions only if the secular equation,

$$|\Gamma_{jk} - \delta_{jk}\rho v^2| = 0 \tag{A.8}$$

is satisfied. This is a cubic equation in ρv^2 with three real roots. For each value of the phase velocity v found from (A.8), there is a corresponding polarization vector $\hat{e}$, which can be determined from (A.7). These will consist of one quasi-longitudinal and two quasi-transverse polarizations. Only if $\vec{k}$ is along a symmetry direction will the modes be pure longitudinal and pure transverse.

The group velocity is the velocity with which energy is transported by the wave. The rate of energy flow per unit area is given by a vector with components[36]

$$Q_i = - \sum_j \sigma_{ij} \frac{\partial u_j}{\partial t} . \tag{A.9}$$

Using (A.1), (A.2), and (A.5), this becomes

$$Q_i = -\frac{1}{2} k^2 v \sum_{jk\ell} C_{ijk\ell} e_j (\ell_\ell e_k + \ell_k e_\ell) e^{2ik(\ell_1 x_1 + \ell_2 x_2 + \ell_3 x_3 - vt)} . \quad (A.10)$$

The total energy density in the medium is

$$U = \sum_i \rho \left(\frac{\partial u_i}{\partial t}\right)^2 \quad (A.11)$$

which, using (A.5), becomes

$$U = -\rho k^2 v^2 \sum_i e_i^2 e^{2ik(\ell_1 x_1 + \ell_2 x_2 + \ell_3 x_3 - vt)} . \quad (A.12)$$

Dividing (A.10) by (A.12), and using the fact that $\sum_i e_i^2 = 1$, the components of the group velocity are found to be

$$v_{Gi} = \frac{Q_i}{U} = \frac{1}{\rho v} \sum_{jk\ell} C_{ijk\ell} \ell_\ell e_j e_k . \quad (A.13)$$

Except along symmetry directions, $\vec{v}_G$ is not colinear with $\vec{k}$. Therefore, in general, the group velocity and the phase velocity vectors will point in different directions in the crystal.

APPENDIX B

THIRD OH^- TUNNELING STATE

With reference to Fig. 5.10, the three localized basis states of the OH^- molecule can be labelled $|a\rangle$, $|b\rangle$, and $|c\rangle$. If $|c\rangle$ is neglected, the eigenstates and eigenvalues of the system are

$$|\psi_1\rangle = (|a\rangle + |b\rangle)/[2(1+S)]^{1/2}$$
$$|\psi_2\rangle = (|a\rangle - |b\rangle)/[2(1-S)]^{1/2} \qquad (B.1)$$

and

$$E_1 = \langle\psi_1|H|\psi_1\rangle = (E_o+\eta)/(1+S)$$
$$E_2 = \langle\psi_2|H|\psi_2\rangle = (E_o-\eta)/(1-S) \qquad (B.2)$$

with the definitions,

$$E_o = \langle a|H|a\rangle = \langle b|H|b\rangle,$$
$$\eta = \langle a|H|b\rangle, \qquad (B.3)$$

and

$$S = \langle a|b\rangle.$$

When the third localized state $|c\rangle$ is included, the following definitions are used,

$$\langle c|H|c\rangle = E_o' ,$$
$$\langle a|H|c\rangle = \langle b|H|c\rangle = \nu, \qquad (B.4)$$

and

$$\langle a|c\rangle = \langle b|c\rangle = S'.$$

By expanding $|\psi_1\rangle$ and $|\psi_2\rangle$ it is easy to show that

$$\langle\psi_1|H|c\rangle = 2\nu/[2(1+S)]^{1/2} ,$$
$$\langle\psi_2|H|c\rangle = 0 , \qquad (B.5)$$
$$\langle\psi_1|c\rangle = 2S'/[2(1+S)]^{1/2},$$

and

$$\langle\psi_2|c\rangle = 0.$$

These results can be used to solve the secular equation,

$$|(\underline{H} - E\underline{I})\underline{\psi}| = 0 \qquad (B.6)$$

for the energy levels E of the system. In this equation, $\underline{I}$ is the 3×3 unit matrix, and $\underline{\psi}$ is the 3 dimensional column vector of the basis states,

$$\underline{\psi} = \begin{pmatrix} |\psi_1\rangle \\ |\psi_2\rangle \\ |c\rangle \end{pmatrix}. \qquad (B.7)$$

Assuming that the overlaps S and S' are small, and can be neglected, the secular equation becomes

$$\begin{vmatrix} E_o+\eta-E & 0 & 2\nu \\ 0 & E_o-\eta-E & 0 \\ 2\nu & 0 & E_o'-E \end{vmatrix} = 0. \qquad (B.8)$$

One solution to the above cubic equation is

$$E = E_o-\eta = E_2 . \qquad (B.9)$$

Therefore, $|\psi_2\rangle$ is still an eigenstate of the system. The other solutions are given by

$$2E = E_o+\eta+E_o' \pm [(E_o+\eta-E_o')^2 + 16\nu^2]^{1/2} . \qquad (B.10)$$

Let $E_o' - E_o = \Delta E$. It was demonstrated in section E of Chapter V that $\Delta E >> |\eta|$. Also, since angle a-d-c in Fig. 5.10 is greater

than angle a-d-b, the overlap $|\nu| << |\eta|$. Therefore, $16\nu^2 << (\eta-\Delta E)^2$, so equation (B.10) is approximately

$$2E \simeq E_o+\eta+E_o' \pm (\eta-\Delta E)\left[1 + \frac{8\nu^2}{(\eta- \Delta E)^2}\right]$$

or

$$2E \simeq E_o+\eta+E_o' \pm \left(\eta-\Delta E - \frac{8\nu^2}{\Delta E}\right). \qquad \text{(B.11)}$$

Therefore, the other two energy levels are

$$E = E_o + \eta - \frac{4\nu^2}{\Delta E} = E_1 - \frac{4\nu^2}{\Delta E}$$

and

$$E = E_o' + \frac{4\nu^2}{\Delta E} \; . \qquad \text{(B.12)}$$

Since $|\nu| << \Delta E$, the energy levels are not changed very much by allowing tunneling between c and the other two wells. This produces only a small amount of mixing between the $|\psi_1\rangle$ and $|c\rangle$ states.

APPENDIX C

MAGNON AND PHONON TEMPERATURES

Consider a thermal conductivity sample of length L and cross-section area A, with heat flow along the x direction. A total heat flux Q is supplied at $x = -L/2$, and absorbed at $x = L/2$. In general, the temperature of the magnon system $T_m(x)$ at any point x will differ from that of the phonon system $T_p(x)$. If there were no heat flow down the sample through the magnon system, the magnon temperature at each point would come into equilibrium with the phonon temperature. It is assumed that $T_m(x)$ would approach $T_p(x)$ exponentially with a characteristic relaxation time τ_{mp},

$$\frac{dT_m(x)}{dt} = \frac{T_p(x)-T_m(x)}{\tau_{mp}} . \qquad (C.1)$$

Therefore, in a volume element Adx of the sample, the amount of heat per unit time flowing into the magnon system from the phonon system would be

$$dP_m(x) = C_m \frac{dT_m(x)}{dt} Adx = C_m \frac{T_p(x)-T_m(x)}{\tau_{mp}} Adx \qquad (C.2)$$

where C_m is the heat capacity per unit volume of the magnons.

However, if the magnon system has a finite conductivity K_m, the heat which flows into it will be conducted along the sample, and a steady state will be reached. The contribution of a small length dx to the heat flux in the magnon system is

$$dQ_m(x) = \frac{dP_m(x)}{A} = C_m \frac{T_p(x)-T_m(x)}{\tau_{mp}} dx. \qquad (C.3)$$

Therefore, the total magnon heat flux at any point x is given by

$$Q_m(x) = \frac{C_m}{\tau_{mp}} \int_{-L/2}^{x} (T_p(x') - T_m(x'))dx'. \qquad (C.4)$$

But, by definition of the magnon conductivity,

$$Q_m(x) = -K_m \frac{dT_m(x)}{dx}. \qquad (C.5)$$

Combining (C.5) and (C.4), and differentiating yields a second order differential equation for the magnon temperature,

$$\frac{d^2T_m(x)}{dx^2} + \frac{C_m}{K_m\tau_{mp}} (T_p(x)-T_m(x)) = 0. \qquad (C.6)$$

The total heat flux Q is divided between the magnon and phonon systems,

$$Q = Q_p(x) + Q_m(x) = -K_p \frac{dT_p(x)}{dx} - K_m \frac{dT_m(x)}{dx}. \qquad (C.7)$$

Therefore, $T_p(x)$ is related to $T_m(x)$ by

$$\frac{dT_p(x)}{dx} = -\frac{Q}{K_p} - \frac{K_m}{K_p} \frac{dT_m(x)}{dx} \qquad (C.8)$$

with the boundary condition that at the centre of the sample, the phonon and magnon temperatures are both equal to the average temperature T_o of the sample,

$$T_m(o) = T_p(o) = T_o. \qquad (C.9)$$

Solving (C.8), using (C.9), it is found that

$$T_p(x) = \frac{K_m+K_p}{K_p} T_o - \frac{Q}{K_p} x - \frac{K_m}{K_p} T_m(x). \qquad (C.10)$$

Substituting (C.10) into (C.6), the differential equation becomes

$$\frac{d^2T_m(x)}{dx^2} - \frac{C_m}{K_m\tau_{mp}}\left[\frac{K_m+K_p}{K_p}\,(T_m(x)-T_o) + \frac{Q}{K_p}\,x\right] = 0. \qquad (C.11)$$

Since heat enters or leaves the sample at each end only via the phonon system, the heat flux in the magnon system must be zero at both ends,

$$Q_m(L/2) = Q_m(-L/2) = 0. \qquad (C.12)$$

Therefore, from (C.5),

$$\left.\frac{dT_m}{dx}\right|_{L/2} = \left.\frac{dT_m}{dx}\right|_{-L/2} = 0\ . \qquad (C.13)$$

Also, from (C.9), it is known that

$$T_m(o) = T_o\ . \qquad (C.14)$$

Solving equation (C.11) with the boundary conditions (C.13) and (C.14), the magnon temperature is found to be

$$T_m(x) = T_o - \frac{Q}{K_p+K_m}\left(x - \frac{\sinh Bx}{B\cosh BL/2}\right) \qquad (C.15)$$

where the constant B is given by

$$B^2 = \frac{C_m}{\tau_{mp}}\left(\frac{1}{K_p} + \frac{1}{K_m}\right)\ . \qquad (C.16)$$

By substituting (C.15) into (C.10), the phonon temperature can be expressed as

$$T_p(x) = T_o - \frac{Q}{K_p+K_m}\left(x + \frac{K_m}{K_p}\,\frac{\sinh Bx}{B\cosh BL/2}\right). \qquad (C.17)$$

Typical solutions for $T_p(x)$ and $T_m(x)$ are illustrated in Fig. C.1.

FIG. C.1 Magnon and phonon temperatures in a thermal conductivity sample. The temperature profiles were calculated for the parameters, T_o = 2.0 K, L = 5.0 cm, K_p = 3.00 watts cm^{-1} K^{-1}, K_m = 1.83 watts cm^{-1} K^{-1}, and B = 0.830 cm^{-1}. The limiting cases for $B \to 0$, and $B \to \infty$ are also shown

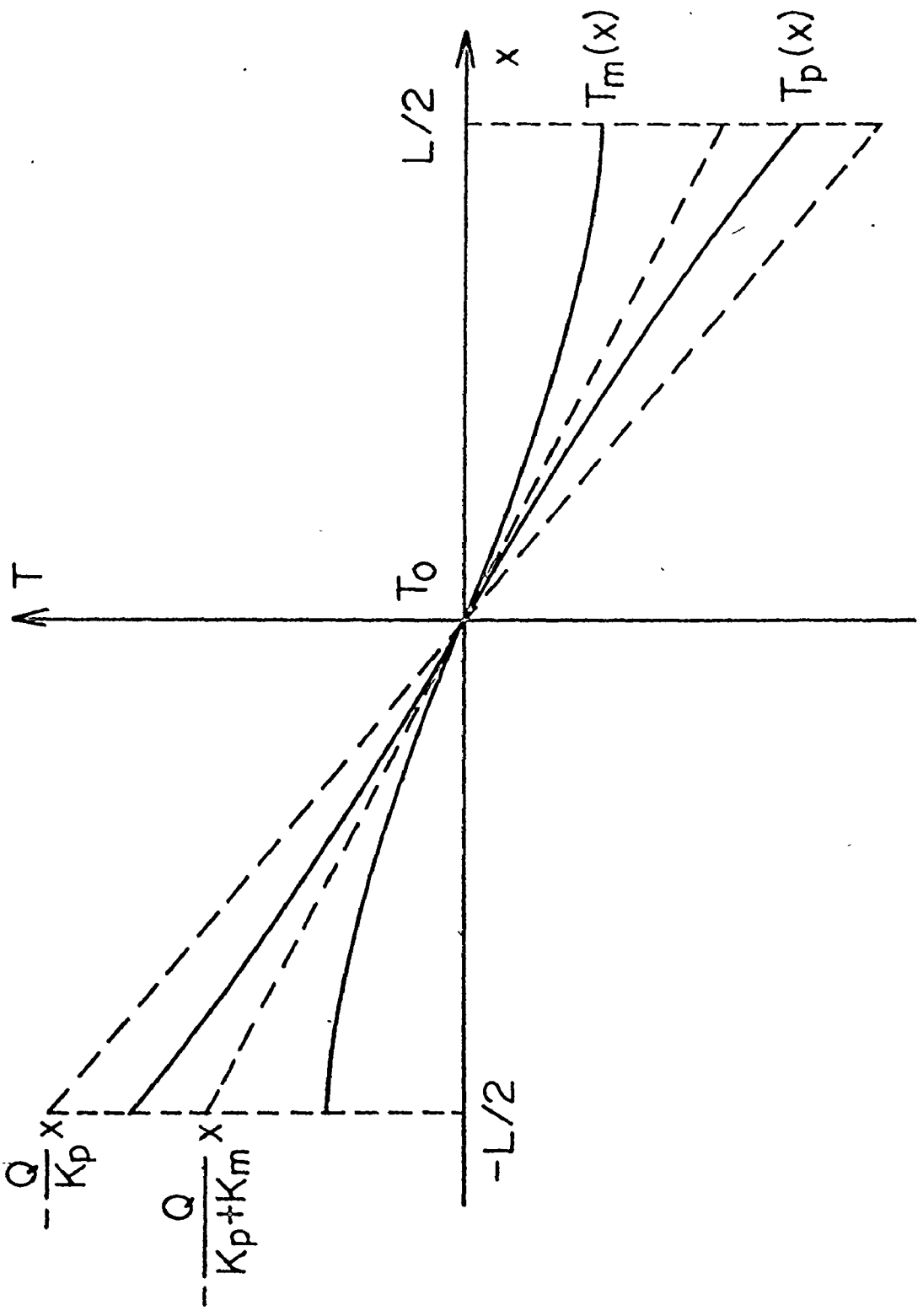
T
x
L/2
-L/2
T0
Tm(x)
Tp(x)
-Q/Kp x
-Q/(Kp+Km) x

The parameter B is related to the coupling between the magnon and phonon systems. If the two systems are perfectly coupled, $\tau_{mp} \to 0$, so $B \to \infty$. In this limit the magnon and phonon temperatures are the same,

$$T_p(x) = T_m(x) \to T_o - \frac{Q}{K_p+K_m} x. \qquad \text{(C.18)}$$

On the other hand, if there were no coupling between the systems, $\tau_{mp} \to \infty$, so $B \to 0$. In this case the solutions become

$$T_p(x) \to T_o - \frac{Q}{K_p} x$$

and $$T_m(x) \to T_o \qquad \text{(C.19)}$$

so there would be no gradient at all in the magnon temperature. These limiting cases are also shown in Fig. C.1.

APPENDIX D

SUBLATTICE MAGNETIZATION ORIENTATION

In this appendix, expressions are developed for the orientations of the sublattice magnetizations of a uniaxial antiferromagnet in the presence of an external field applied along an arbitrary direction. The coordinate system is shown in Fig. D.1. The magnetization of sublattice 1 is $\vec{m}_1$, which has a magnitude $m_s = |\vec{m}_1| = |\vec{m}_2|$. The equilibrium orientation makes an angle θ with the easy axis of magnetization z. In addition, $\vec{m}_1$ and $\vec{m}_2$ are tilted out of the equilibrium direction by an angle t towards the external field $\vec{H}$ which is applied at an angle ψ to z.

A semiclassical approach is used. The exchange, anisotropy, and Zeeman terms of the Hamiltonian (2.68) can be expressed in a molecular field model as

$$\begin{aligned} E_E &= -\lambda \vec{m}_1 \cdot \vec{m}_2 \\ E_A &= -\frac{K}{2m_s^2}(m_{1z}^2 + m_{2z}^2) \\ E_Z &= -(\vec{m}_1 + \vec{m}_2)\cdot\vec{H} \end{aligned} \qquad \text{(D.1)}$$

and

where λ is the exchange constant, and K is the anisotropy constant. Expressing each of these in terms of the angles of Fig. D.1 and simplifying, gives

$$\begin{aligned} E_E &= -m_s H_E \cos 2t \\ E_A &= -m_s H_A(\cos^2\theta\cos^2 t + \sin^2\theta\sin^2 t) \\ E_Z &= -2m_s H \sin(\psi+\theta)\sin t \end{aligned} \qquad \text{(D.2)}$$

and

FIG. D.1 Orientations of the sublattice magnetizations in a uniaxial antiferromagnet. The labels are defined in the text.

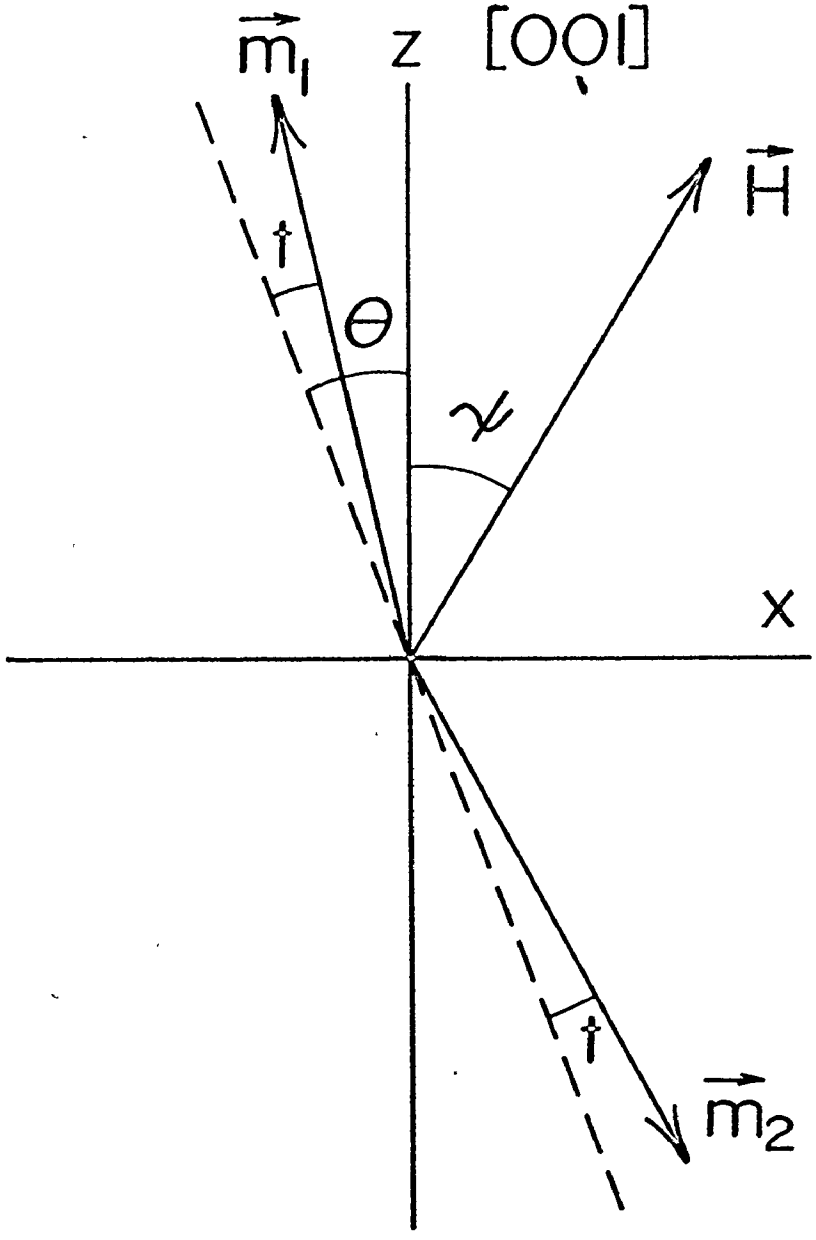
$\vec{m}_1$
z
[001]
$\vec{H}$
θ
φ
x
$\vec{m}_2$

where $H_E = -\lambda m_s$ is the effective exchange field, and $H_A = K/m_s$ is the anisotropy field.

Minimizing the total energy with respect to t gives

$$\sin t = \frac{H \sin(\psi+\theta)}{2H_E+H_A\cos 2\theta} . \qquad (D.3)$$

It is assumed that $H_A << H_E$, so the second term in the denominator can be neglected. Therefore,

$$\sin t \approx \frac{H \sin(\psi+\theta)}{2H_E} . \qquad (D.4)$$

Substituting the equilibrium value of t from (D.4), the total energy becomes

$$E = -\frac{m_s}{2}\frac{H^2}{H_E}\sin^2(\psi+\theta) - m_s H_E - m_s H_A \cos^2\theta + \frac{m_s}{4}\frac{H^2 H_A}{H_E^2}\sin^2(\psi+\theta)\cos 2\theta . \qquad (D.5)$$

Minimizing (D.5) with respect to θ one finds, after some lengthy algebra, that

$$\sin\theta\cos\theta = \frac{H^2}{2H_A H_E}\sin(\psi+\theta)\left[\cos(\psi+\theta) + \frac{H_A}{2H_E}\cos(\psi+3\theta)\right] . \qquad (D.6)$$

Again assuming $H_A << H_E$, and noting that $H_c = (2H_A H_E)^{1/2}$ is the spin-flop field, this becomes

$$\sin\theta\cos\theta \approx \left(\frac{H}{H_c}\right)^2 \sin(\psi+\theta)\cos(\psi+\theta) \qquad (D.7)$$

which can be solved for θ to give

$$\tan 2\theta = \frac{\sin 2\psi}{(H_c/H)^2 - \cos 2\psi} . \qquad (D.8)$$

Therefore, for a given external field, the magnetization orientations are given by the solutions to equations (D.8) and (D.4).

These are equivalent to the expressions of Nagamiya et al.[110], which were derived by setting the total torque on the magnetizations equal to zero.

For $\psi = 0$, (D.8) has two solutions, $\theta = 0$, or $\pi/2$. The correct solution is $\theta = 0$ for $H < H_c$, and $\theta = \pi/2$ for $H > H_c$. Therefore, if $\vec{H}$ is applied along the easy axis, then at the spin-flop field the sublattice magnetizations abruptly flop into an orientation perpendicular to $\vec{H}$. For very large fields, this is always the lowest energy configuration, because the perpendicular susceptibility is much larger than the parallel susceptibility. However, if $\vec{H}$ is applied at a finite angle to the easy axis, there is no abrupt transition. The magnetizations rotate continuously from $\theta = 0$ to $\psi+\theta = \pi/2$ as the field is increased.

REFERENCES

1. H. Sato, Prog. Theor. Phys. 13, 119 (1955).
2. S. A. Friedberg and E.D. Harris, "Proceedings of the 8th. International Conference on Low Temperature Physics" (Butterworths, London, 1962), p. 302.
3. B. Luthi, J. Phys. Chem. Solids 23, 35 (1962).
4. R. L. Douglass, Phys. Rev. 129, 1132 (1963).
5. J. E. Rives, G. S. Dixon and D. Walton, J. Appl. Phys. 40, 1555 (1969).
6. C. M. Bhandari and G.S. Verma, Phys. Rev. 152, 731 (1966).
7. D. Walton, J. E. Rives, and Q. Khalid, Phys. Rev. B 8, 1210 (1973).
8. D. C. McCollum, R. L. Wild, and J. Callaway, Phys. Rev. 136, A426 (1964).
9. F. W. Gorter, L.J. Noordermeer, A. R. Kop, and A. R. Miedema, Phys. Lett. 29A, 331 (1969).
10. R. H. Donaldson and D.T. Edmonds, Phys. Lett. 2, 130 (1962).
11. Chen-Chou Ni and H. Weinstock, Phys. Lett. 34A, 3 (1971).
12. M. J. Metcalfe and H.M. Rosenberg, Phys. Lett. 33A, 211 (1970).
13. J. E. Rives, Phys. Lett. 36A, 327 (1971).
14. G. S. Dixon and D. Walton, Phys. Rev. 185, 735 (1969).
15. D. Douthett and S. A. Friedberg, Phys. Rev. 121, 1662 (1961).
16. J. E. Rives and D. Walton, Phys. Lett. 27A, 609 (1968).

17. G. Laurence and D. Petitgrand, Phys. Rev. B 8, 2130 (1973).

18. J. Gustafson and C. T. Walker, Phys. Rev. B 8, 3309 (1973).

19. J. B. Hartmann, Ph.D. thesis (Cornell University, 1974) (unpublished).

20. A. Okazaki, K. C. Turberfield, and R.W.H. Stevenson, Phys. Lett. 8, 9 (1964).

21. O. Nikotin, P. A. Lingard, and O. W. Dietrich, J. Phys. C 2, 1168 (1969).

22. W. Stutius and J. R. Dilinger, "17th. Annual Conference on Magnetism and Magnetic Materials" (A.I.P., Chicago, 1971), Part 1, p. 650.

23. J. Gustafson, Ph.D. thesis (Northwestern University, 1972) (unpublished).

24. K. P. Dere, M.Sc. thesis (Cornell University, 1971) (unpublished).

25. L. Pauling, Phys. Rev. 36, 430 (1930).

26. V. Narayanamurti and R. O. Pohl, Rev. Mod. Phys. 42, 201 (1970).

27. J. M. Ziman, "Electrons and Phonons" (Oxford U.P., London, 1960).

28. C. Kittel, "Quantum Theory of Solids" (John Wiley, New York, 1963).

29. P. Carruthers, Rev. Mod. Phys. 33, 92 (1961).

30. P.G. Klemens, in "Solid State Physics", edited by F. Seitz and D. Turnbull (Academic Press, New York, 1958), Vol. 7, p. 1.

31. J. Callaway, Phys. Rev. 113, 1046 (1959).

32. A. K. McCurdy, H. J. Maris, and C. Elbaum, Phys. Rev. B 2, 4077 (1970).

33. R. L. Melcher, Phys. Rev. B 2, 733 (1970).

34. A. J. Henderson, Jr., H. Meyer, and H. J. Guggenheim, J. Phys. Chem. Solids 32, 1047 (1971).

35. G. W. Farnell, Can. J. Phys. 39, 65 (1961).

36. F. I. Fedorov, "Theory of Elastic Waves in Crystals" (Plenum, New York, 1968) p. 121.

37. H.G.B. Casimir, Physica 5, 495 (1938).

38. J. Callaway and H.C. von Baeyer, Phys. Rev. 120, 1149 (1960).

39. R. O. Pohl, Phys. Rev. Lett. 8, 481 (1962).

40. C. T. Walker and R.O. Pohl, Phys. Rev. 131, 1433 (1963).

41. D. Walton, H. A. Mook and R. M. Nicklow, Phys. Rev. Lett. 33, 412 (1974).

42. D. Walton, Phys. Rev. B 7, 3925 (1973).

43. D. Walton in "Point Defects in Solids", edited by J. H. Crawford, Jr. and L. M. Slifkin (Plenum, New York, 1973).

44. A. F. Devonshire, Proc. Roy. Soc. (London) A153, 601 (1936).

45. P. Sauer, Z. Physik 194, 360 (1966).

46. M. Gomez, S. P. Bowen, and J. A. Krumhansl, Phys. Rev. 153, 1009 (1967).

47. P. Sauer, O. Schirmer, and J. Schneider, Phys. Status Solidi 16, 79 (1966).

48. H. B. Shore, Phys. Rev. 151, 570 (1966).

49. R. J. von Gutfeld, in "Physical Acoustics", edited by W.P. Mason (Academic, New York, 1968), Vol. 5, p. 233.

50. J. M. Andrews, Jr. and M.W.P.Strandberg, Proc. IEEE 54, 523 (1966).

51. B. Taylor, H. J. Maris, and C. Elbaum, Phys. Rev. B 3, 1462 (1971).

52. W. A. Little, Can. J. Phys. 37, 334 (1959).

53. O. Weiss, Z. Angew. Physik 26, 325 (1969).

54. R. J. von Gutfeld, A. H. Nethercot, Jr., and J. A. Armstrong, Phys. Rev. 142, 436 (1966).

55. R. C. Dynes and V. Narayanamurti, Phys. Rev. B 6, 143 (1966).

56. V. Narayanamurti, Phys. Lett. 30A, 521 (1969).

57. C. C. Ackerman and R. A. Guyer, Ann. Phys. (New York) 50, 128 (1968).

58. J. B. Brown, D. Y. Chung, and P. W. Matthews, Phys. Lett. 21, 241 (1966).

59. H. E. Jackson, C. T. Walker,and T. F. McNelly, Phys. Rev. Lett. 25, 26 (1970).

60. R. L. Melcher, Phys. Rev. Lett. 25, 1201 (1970).

61. J. Callaway, Phys. Rev. 132, 2003 (1963).

62. S. W. Lovesey, J. Phys. C 1, 102 (1968).

63. F. Keffer, in "Handbuch der Physik", edited by S. Flugge (Springer-Verlag, Berlin, 1966), Vol. 18, Part 2, p. 1.

64. J. Kanamori, in "Magnetism", edited by G. T. Rado and H. Suhl (Academic, New York, 1963), Vol. 1, p. 127.

65. C. Kittel, Phys. Rev. 110, 836 (1958).

66. C. Kittel and E. Abrahams, Rev. Mod. Phys. 25, 233 (1953).

67. K. P. Sinha and U. N. Upadhyaya, Phys. Rev. 127, 432 (1962).

68. A. W. Joshi and K. P. Sinha, "Proceedings of the International Conference on Magnetism, Nottingham, 1964" (Institute of Physics, London, 1964), p. 411.

69. U. N. Upadhyaya and K. P. Sinha, Phys. Rev. 130, 939 (1963).

70. R. Gonano and E. D. Adams, Rev. Sci. Instrum. 41, 716 (1970).

71. D. Walton, Rev. Sci. Instrum. 37, 734 (1966).

72. R. H. Sherman, S. G. Sydoriak, and T. R. Roberts, J. Res. Natl. Bur. Stand. 68A, 579 (1964).

73. T. R. Roberts and S. G. Sydoriak, Phys. Rev. 102, 304 (1956).

74. A. Freddi and I. Modena, Cryogenics 8, 18 (1968).

75. R. P. Hudson, Cryogenics 9, 76 (1969).

76. W. R. Abel, A. C. Anderson, and J. C. Wheatley, Rev. Sci. Instrum. 35, 444 (1964).

77. W. C. Black, Jr., W. R. Roach, and J. C. Wheatley, Rev. Sci. Instrum. 35, 587 (1964).

78. M. C. Hetzler and D. Walton, Rev. Sci. Instrum. 39, 1656 (1968).

79. F. Brickwedde et al., J. Res. Natl. Bur. Stand. 64A, 1 (1960).

80. R. W. Cohen and B. Abeles Phys. Rev. 168, 444 (1968).

81. D. H. Liebenberg and L.D. F. Allen, J. Appl. Phys. 41, 4050 (1970).

82. A. S. Nowick and W. R. Heller, Advan. Phys. 14,101 (1965).

83. P. Heller and G. B. Benedek, Phys. Rev. Lett. 8, 428 (1962).

84. P. P. Peressini, J. P. Harrison, and R. O. Pohl, Phys. Rev. 180, 926 (1969).

85. M. J. P. Musgrave, Proc. Roy. Soc. (London) A226, 339 (1954).

86. G. F. Miller and M. J. P. Musgrave, Proc. Roy. Soc. (London) A236, 352 (1956).

87. M. Griffel and J. W. Stout, J. Am. Chem. Soc. 72, 4351 (1950).

88. D. F. Gibbons, Phys. Rev. 115, 1194 (1959).

89. R. L. Rosenbaum, C. K. Chau, and M. V. Klein, Phys. Rev. 186, 852 (1969).

90. C. W. McCombie and J. Slater, Proc. Phys. Soc. (London) 84, 499 (1964).

91. R. O. Pohl, in "Localized Excitations in Solids", edited by R. F. Wallis (Plenum, New York, 1968), p. 443.

92. R. A. Sherlock, A.F.G. Wyatt, N. G. Mills, and N. A. Lockerbie, Phys. Rev. Lett. 29, 1299 (1972).

93. R. L. Melcher, private communication.

94. H. Hartel and F. Luty, Phys. Status Solidi 12, 347 (1965).

95. J. W. Stout and S. A. Reed, J. Am. Chem. Soc. 76, 5279 (1954).

96. B. Wedding and M. V. Klein, Phys. Rev. 117, 1274 (1969).

97. M. Tinkham, "Group Theory and Quantum Mechanics" (McGraw-Hill, New York, 1964).

98. D. Walton, Phys. Rev. Lett. 19, 305 (1967).

99. M. C. Hetzler, Jr. and D. Walton, Phys. Rev. B 8, 4801 (1973).

100. R. A. Herendeen and R.H. Silsbee, Phys. Rev. 188, 645 (1969).

101. B. G. Dick and D. Strauch, Phys. Rev. B 2, 2200 (1970).

102. J. M. Ziman, Proc. Phys. Soc. (London) 65, 540 (1952).

103. R. Kubo, Phys. Rev. 87, 568 (1952).

104. D. H. Katayama and K. A. McCarthy, Bull. Am. Phys. Soc. 15, 1592 (1970).

105. D. Walton, "Proceedings of the International Conference on Phonon Scattering in Solids" (CEN, Saclay, France, 1972).

106. D. A. Goodings and B. W. Southern, private communication.

107. J. P. Kotthaus and V. Jaccarino, Phys. Lett. 42A, 361 (1973).

108. R. M. White, R. Freedman, and R. B. Woolsey, Phys. Rev. B 10, 1039 (1974).

109. E. G. Spencer and R. C. LeCraw, Phys. Rev. Lett. 4, 130 (1960).

110. T. Nagamiya, K. Yosida,and R. Kubo, Advan. Phys. 4, 1 (1955).

111. D. W. Alderman and R. M. Cotts, Phys. Rev.B 1, 2870 (1970).

112. N. E. Byer and H. S. Sack, J. Phys. Chem. Solids 29, 677 (1968).

113. W. D. Seward, V. Reddy and J. W. Shaner, Solid State Comm. 11, 1569 (1972).

114. P. P. Peressini, J. P. Harrison, and R. O. Pohl, Phys. Rev. 182, 939 (1969).